[AMERICAN JOURNAL OF SCIENCE, VOL. 298, MAY, 1998, P. 349–438]

American Journal of Science

MAY 1998

A MODEL OF SURFACE SITE TYPES ON OXIDE AND SILICATE MINERALS BASED ON CRYSTAL CHEMISTRY: IMPLICATIONS FOR SITE TYPES AND DENSITIES, MULTI-SITE ADSORPTION, SURFACE INFRARED SPECTROSCOPY, AND DISSOLUTION KINETICS

CARLA M. KORETSKY,* DIMITRI A. SVERJENSKY, and NITA SAHAI

Morton K. Blaustein Department of Earth and Planetary Sciences, Johns Hopkins University, 3400 N. Charles Street, Baltimore, Maryland 21218

ABSTRACT. In this study, a method for estimating site types and ionizable site densities at mineral surfaces by consideration of ideal crystal surfaces has been developed. Periclase, rutile, goethite, hematite, corundum, kaolinite, andalusite, sillimanite, sanidine, albite, anorthite, and quartz surfaces were considered, both because they represent a wide range of crystal structures and because many adsorption and dissolution studies have focused on these minerals. For each mineral, the predominant cleavage or growth faces were studied. To avoid choosing arbitrary slices of the crystal parallel to each cleavage or growth face, the total Brown bond strengths (and the resulting partial charges on coordinatively unsaturated atoms) were calculated for the bonds that must be broken to generate each possible ideal slice on a given plane. The charge-neutral or nearly charge-neutral slices produced with a minimum total strength of bonds severed were examined with the aid of the commercial computer program CrystalMaker©.

Once the ideal mineral surface for a given plane was chosen, the number of sites per unit surface area was calculated using five different methods. For the minerals considered, calculated site densities for a given surface ranged from 0 to 40.8 sites/nm^2, a considerably larger range than the density of 2.3 to 10 sites/nm^2 that is often cited. The results from each of the methods were compared to available experimental estimates of surface hydroxyl site densities from temperature desorption experiments, infrared data, and tritium exchange methods and to ionizable or reactive site densities from acid-base titrations and chemical reaction methods. Estimates based on the number of broken bonds gave the best agreement with site densities using the tritium exchange method. However, estimates based on the number of coordinatively unsaturated atoms or on the partial charge of coordinatively unsaturated atoms were also consistent with much of the available tritium exchange data. Predicted site types were compared with the available spectroscopic data. Implications of predicted site types with respect to the interpretation of infrared data and for improving adsorption and dissolution rate models are discussed.

INTRODUCTION

The cycling of elements at Earth's surface is influenced both by the adsorption of cations and anions onto mineral surfaces and by mineral dissolution rates. For example, the mobility of anthropogenic organic contaminants such as pesticides or of toxic metals like cadmium or lead might be greatly retarded or accelerated by adsorption or desorption at mineral surfaces. In natural settings, adsorption or desorption processes may contribute to ore formation and influence the availability of nutrients in soils.

* Current address: School of Earth & Atmospheric Sciences, Georgia Institute of Technology, Atlanta, Georgia, 30332-0340.

Adsorption probably also plays a significant role in the scavenging of metals in the oceans. Therefore, there has been widespread interest among geochemists in the development of models to assess quantitatively the effects of adsorption processes in natural environments. Single-site adsorption models such as the triple layer model (Yates, ms; Davis, James, and Leckie, 1978; Hayes and others, 1991), the diffuse double layer model (Stumm, Huang, and Jenkins, 1970; Huang and Stumm, 1973), and the constant capacitance model (Schindler and Kamber, 1968; Hohl and Stumm, 1976; Sposito, 1984; Schindler and Stumm, 1987) all require an estimate of the total number of reactive sites per unit area (the site density) present on a given mineral. Multi-site models, such as MUSIC (Hiemstra, Riemsdijk, and Bolt, 1989; Hiemstra, Wit, and Riemsdijk, 1989) require not only an estimate of the total site density but also require descriptions of all the site types that may react with adsorbates.

The development of quantitative dissolution rate models is also of interest, because silicate dissolution plays such a vital role in the global cycling of CO_2. The weathering of silicate minerals involves uptake of CO_2 to produce aqueous bicarbonate ion, which is eventually transported to the sea where it may participate in the precipitation of carbonate minerals (Berner, 1994). The rates and the temperature dependence of the rates of such weathering reactions will influence the effect that increased concentrations of $CO_{2(g)}$ may have on global climate. Recent models of silicate dissolution rates include terms to account for the speciation of hydrogen at mineral surfaces. For example, Dove (1994) found that the dissolution rate of quartz may be modeled as

$$R = k_{>SiOH}(\theta_{>SiOH})^{n>SiOH} + k_{>SiO-tot}(\theta_{>SiO-tot})^{n>SiO-tot} \quad (1)$$

where R is the dissolution rate, k_i is the rate constant for the reaction of surface species i, n_i is the reaction order of surface species i, $\theta_{>SiOH}$ is the fraction of total surface sites present as >SiOH, and $\theta_{>SiO-tot}$ is the sum of the fractions of total surface sites present as either deprotonated $>SiO^-$ or as a complex with sodium ion, $>SiO\text{-}Na^+$. Thus, dissolution rates may fundamentally depend on surface site densities.

It is possible to measure surface hydroxyl site densities using a variety of experimental techniques (James and Parks, 1982; Davis and Kent, 1990). Such techniques include weight loss methods, H_2O sorption/desorption experiments, NMR spectroscopy, tritium exchange, and chemical reaction at the surface (for example, monitoring sorption of probe molecules such as ammonia or pyridine). Infrared spectroscopy is an excellent method for determining how many types of surface hydroxyl groups exist on a given mineral (for example, Little, 1966; Hair, 1967; Iler, 1979). In addition, the integrated intensity of infrared absorption bands can sometimes be useful for making quantitative or semi-quantitative measurements of surface hydroxyl group densities. Ionizable or reactive site densities can be measured using techniques such as acid-base titrations or chemical reaction methods (James and Parks, 1982; Dzombak and Morel, 1990). Unfortunately, all these techniques can be difficult to apply in practice and often give widely varying estimates of site densities for a given mineral.

Some effort has also been made to use crystal structure and habit to calculate surface hydroxyl site densities (Anderson, Horlock, and Oliver, 1965; Jones and Hockey, 1971b; Yates, ms; Morimoto, Nagao, and Tokuda, 1969; Barron and Torrent, 1996), but relatively few minerals have been considered in such studies. More importantly, none of these studies makes any attempt to justify the assumed choices of surface configuration or the mechanism of H_2O dissociation over that surface even though such assumptions have an enormous effect on the calculated site densities. Other studies (for example, Tsyganenko and Filimonov, 1973) have explored the types of surface sites that might exist on various minerals without attempting to calculate site densities.

Because surface site densities are difficult to measure experimentally and because there are few reliable techniques for calculating site densities, surface site densities are unknown for most geologically significant minerals. Therefore, a number of workers

have suggested setting surface site densities to a single constant for all minerals (Hayes and others, 1991; Davis and Kent, 1990). For example, Hayes and others (1991) recommend a values of 10 sites/nm^2, whereas Davis and Kent (1990) recommend 2.31 sites/nm^2. Davis and Kent (1990) argue that the choice of a single value of site density will lead to the development of consistent thermodynamic databases for applications to problems of adsorption onto soils or sediments where site densities are poorly known. Similarly, because potentiometric titrations could be fit equally well using 1, 10, or 100 sites/nm^2, Hayes and others (1991) recommend using 10 sites/nm^2 for all oxides.

However, setting all surface site densities to a single number ignores the contribution of the actual site density to the fitted equilibrium constants, limiting the comparability of log K values obtained for different minerals. This makes quantitative semi-empirical or theoretical predictions of adsorption in varied systems using fitted equilibrium constants (for example, Sverjensky, 1993; Sverjensky and Sahai, 1996; Sahai and Sverjensky, 1997) much more difficult. In addition, this type of approach does not provide any information concerning the variety of surface site types that might occur on different minerals.

The main purpose of this paper is to determine the numbers and types of sites exposed at various idealized mineral surfaces, such as might occur when minerals are freshly cleaved under vacuum, or in air, or at mineral surfaces with perfect growth faces. The general term "surface site" is used in this paper to describe any potentially reactive atom or set of atoms at a mineral surface. Atoms or molecules at the mineral-air or mineral-water interface may "chemically" or "physically" bind to such sites. "Chemically" bound atoms or molecules are strongly held at the surface by covalent or ionic chemical bonds, whereas "physically" bound atoms or molecules are less strongly held at the surface by H-bonding or by electrostatic interactions.

The idealized cleavage and growth planes used in this study were chosen after evaluating both the strength of bonds broken in generating different surfaces on a single face of a given mineral and after evaluating the net charge left at the surface for each different slice. Using the predicted surface configurations, the numbers and types of coordinatively saturated and unsaturated near surface atoms and the depths of all atoms in the unit cell relative to the surface have been calculated. This information is used to estimate surface site densities and to describe possible surface site types on various planes of twelve oxide and silicate minerals.

METHOD FOR EVALUATION OF SITE DENSITIES AND TYPES: LOCATION OF CLEAVAGE AND GROWTH PLANES IN THE CRYSTAL STRUCTURE

Before it is possible to estimate the number and types of surface sites that exist on a given crystal, the planes that are most likely to bound the crystal must be determined (Peri, 1965; Jones and Hockey, 1971b; James and Parks, 1982). Many minerals used in dissolution or adsorption studies are crushed during sample preparation. It is likely that such minerals will be bounded at least in part by their best cleavage planes, if they have any. However, rounding of the grains may expose many other planes, as well. Alternatively, if the minerals are not crushed prior to experiment, they are likely to be bounded primarily by growth faces. Clearly, very different planes, and therefore very different sites, might be exposed at the surface of a given mineral depending on the crystal form chosen and the method of sample preparation. In this study surface sites are described for some of the most common growth and cleavage planes of the twelve minerals considered. "Total" site densities were calculated for each of these minerals based on averages of both growth and cleavage planes. *However, whenever possible it is recommended that these averages be modified to reflect the relative abundances of cleavage or growth planes actually present on a given sample.* It is also important to note that many planes not explicitly considered in this study may also be exposed on real samples.

The orientation of cleavage and growth planes are very well known for a wide variety of minerals (Klein and Hurlbut, 1993; Deer, Howie, and Zussman, 1993; Zoltai

and Stout, 1984). However, the precise placement of these planes with respect to the actual crystal structures is not well known. For each cleavage or growth plane of a given mineral, parallel slices through the structure will yield very different surface structures. For example, if the surface of the (001) basal plane of kaolinite is constructed without

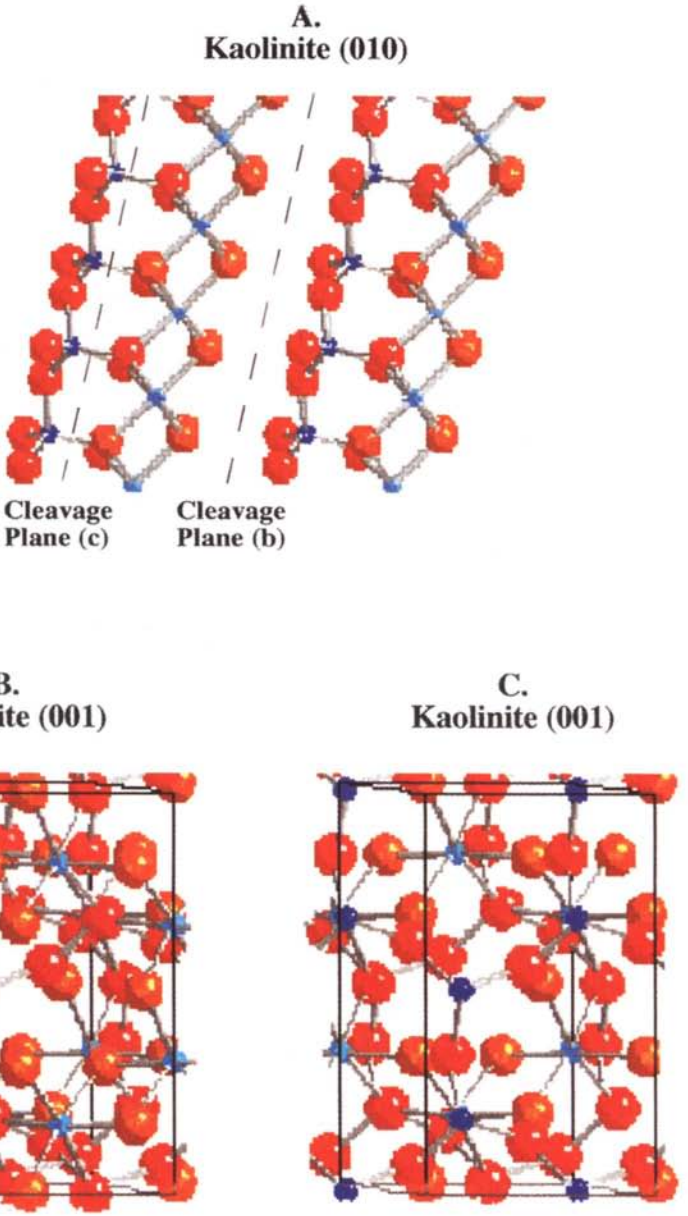

Fig. 1(**A**) Schematic depiction of the kaolinite structure projected onto (010) from CrystalMaker©. Slicing in and out of the plane of the page along the dashed line marked (b) will yield the coordinatively unsaturated, charged kaolinite (001) surface shown in (**B**). Slicing along the dashed line marked (c) will yield the charge-neutral, coordinatively saturated kaolinite (001) surface shown in (C). Red spheres represent oxygen atoms, gold spheres represent hydroxide anions, light blue spheres represent aluminum atoms and purple spheres represent silicon atoms.

regard to the strength of severed bonds, various kaolinite (001) surface configurations may result. One possible (001) surface on kaolinite is created by placing the cleavage plane along the interlayer region between the tetrahedral and octahedral sheets (fig. 1A, cleavage plane (B) and fig. 1B) of the structure. However, another surface, also on the (001) plane, could be generated by cutting through the tetrahedral sheet (fig. 1A, cleavage plane (C), and fig. 1C). In fact, many possible surfaces, all on kaolinite (001), could be formed, depending on where the structure is sliced. In the case of the kaolinite basal plane, the hydrogen bonding between the tetrahedral and octahedral sheets is much weaker than the bonding within the layers, so that the "true" cleavage plane is very likely to occur between the T-O layers. For many other mineral structures, the placement of cleavage or growth planes is not as evident.

For each mineral considered in this study, the program CrystalMaker© (Palmer, 1996) was used to generate a surface on the plane of interest. Next, the top layer of atoms in the unit cell was stripped away to yield a new surface on the same plane. This procedure was repeated until all possible slices were made through the crystal structure. For each slice, the coordination of each atom in a unit cell that included the surface atoms was recorded, including the lengths and types of all broken or "dangling" bonds formed by the atoms at or near the top of the unit cell. The depths of all atoms in the unit cell relative to the highest layer of atoms were also calculated.

It has been shown that clean surfaces (that is, surfaces created in vacuum) often show relaxation of the first few atomic layers. Typically, these layers pull inward, toward the bulk of the structure, reducing the spacing between the first few layers by as much as 15 percent of the ideal spacing (Heinrich, 1983; Hochella, 1990, 1995). Lateral reconstruction may also occur on real surfaces, changing the coordination of surface atoms from what is observed in the bulk crystal structure. An example of surface relaxation was recently studied by Becker, Hochella, and Apra (1996). They calculated electronic structure and wave functions for a periodic, infinite slab of hematite and found that on hematite (001) the coordinatively unsaturated, uppermost Fe atoms in the structure should relax downward by 0.48 Å on a freshly cleaved surface but should relax downward by only 0.30 Å if H_2O is adsorbed at the surface. In the present study, only ideal surfaces were considered. Bond lengths and angles and depths of atoms with respect to the surface were all calculated with the assumption that no lateral reconstruction and no relaxation occurs.

In addition to modification of surface structures by surface relaxation and reconstruction, it has been shown that cleavage and growth surfaces of minerals are rarely, if ever, perfectly flat (Hochella, 1990, 1995). Instead, mineral surfaces have very complex microtopography. Flat areas on the surface (terraces) are separated by multiple steps that can range from a single atom to many atoms in height. Corners in these steps, called kinks, holes in the terraces with a single or a few missing atoms, or areas with a single atom or molecule bound to a terrace also occur. Steps and kinks, in particular, may represent sites of high reactivity because atoms at these locations in the structure are less coordinatively saturated than atoms at flat terraces. In this study, only atomically flat surfaces analogous to terraces of a real mineral were considered. The role of steps and kinks in modifying site densities and kinks may be modeled in a future study (Koretsky, ms).

An empirical relationship between bond length and bond strength has been developed by Brown and Shannon (1973). This model has since been improved Altermatt and Brown (1985). Using the empirical relationship

$$s = \exp [(r_O - r)/B] \quad (2)$$

given by Altermatt and Brown (1985), where s is bond strength, r_O is an empirical parameter for a given cation-anion pair, r is the bond length, and B is a fitted parameter equal to 0.37, bond strengths were calculated for all bonds in each mineral considered in

this study. As described above, all possible ideal surfaces were generated along each cleavage or growth plane for each mineral. Using the calculated Brown bond strengths, the absolute value of the strength of the bonds per unit cell severed to create each of these surfaces could then be calculated. The surface along each cleavage or growth direction that resulted in the minimum absolute value of broken bond strength was then used to assess site densities, subject to one additional constraint.

In the method described, no account is taken for the residual positive or negative charge left on coordinatively unsaturated surface atoms. If an excess of either cations or anions is stripped from the surface, a residual surface charge will result. Since charged surfaces are generally considered to be less stable than uncharged surfaces in air or in vacuum (for example, Tsukada, Adachi, and Satoko, 1983), charge-neutral or nearly charge-neutral surfaces were chosen in this study even when these surfaces did not minimize the absolute value of broken bond strength. However, it should be noted that with very few exceptions, the surfaces with minimum strength of broken bonds were also charge-neutral. In other words, in most cases, both criteria were equally satisfied by the surfaces described in this study.

To calculate the residual charge at the surface, surface cations were assigned a positive charge equal to the strength of each of their broken bonds, and surface anions were assigned a negative charge equal to the strength of each of their broken bonds. These positive and negative residual charges were summed to give the total (as opposed to absolute value of) Brown bond strength broken. For example, the quartz (100) surface considered in this study has one 3-fold coordinated Si atom and one 1-fold coordinated oxygen atom in each surface unit cell. Both atoms are missing one Si-O bond of length 1.61 Å, which corresponds to a Brown bond strength of 1.05 valence units (v.u.). This gives an *absolute* value of broken bond strength of 2.10 v.u. per unit cell. However, in calculating the total Brown bond strength, the broken bond on the Si atom is assigned a positive strength of 1.05 v.u., while the broken bond on the O atom is assigned a negative strength of 1.05 v.u. Summing these gives the total Brown bond strength for this surface of 0 v.u. per unit cell. A total Brown bond strength of zero indicates a charge-neutral surface. In cases where more than one charge-neutral surface could be generated, the surface of minimum absolute value of broken bond strength was chosen for study. If no charge-neutral surface could be generated, the surface with the total Brown bond strength closest to zero was chosen.

Once a specific surface plane is chosen, the number and types of surface sites may be assessed. Such sites may be defined and counted in a number of ways. For example, Anderson, Horlock, and Oliver (1965), Jones and Hockey (1971b) and Yates (ms) all assumed that H_2O would dissociate over a fresh surface such that each hydroxyl would bond to a near-surface cation, and each hydrogen would bond to a near-surface oxygen. In other words, surface cation and oxygen atoms were assumed to bond to hydroxyl or hydrogen, regardless of their coordinative state prior to the hydroxyl or hydrogen adsorption. In contrast, Hollabaugh and Chessick (1961) used the average atomic spacing of Ti and O atoms in the bulk structure of rutile, together with an assumed surface area, to calculate the number of Ti atoms that should be present at the rutile surface. They then assumed that each Ti atom would hydroxylate and therefore used the number of Ti atoms at the surface as an estimate of surface hydroxyl density.

In this study, the number of surface sites on each surface were counted using five distinct methods. In the first method, each broken bond on a near-surface atom was counted as one site. For example, a 3-fold coordinated Si atom at the quartz surface was counted as one site, whereas a 2-fold coordinated Si on quartz was counted as two sites. In the second method, each coordinatively unsaturated atom, that is, an atom with a smaller coordination number than it would have in the bulk structure, was counted as one site. Thus, either a 2-fold or a 3-fold coordinated Si atom was counted as a *single* site.

If it is assumed that it is not the coordination of an atom, but rather its proximity to the surface that determines whether an atom or molecule can bind to it, then a method of site counting analogous to that of Jones and Hockey (1971b) is required. In the third method considered in this study, a near-surface atom was defined as an atom within 1.4 Å of the highest plane of atoms in a given surface. This corresponds to all atoms within one oxygen radius of the topmost atoms on the plane. Using this definition, all atoms within 1.4 Å depth of the surface were counted as sites, with each atom equal to one site. In the fourth counting scheme, only oxygen atoms within 1.4 Å depth were considered as possible sites, again, with each oxygen atom equivalent to one site.

In the fifth and final method of estimating site densities, a quite different approach was taken. In this method, the charge on each coordinatively unsaturated atom was calculated using the Brown bond strengths of the broken bonds. As before, each coordinatively unsaturated cation was assigned a positive charge equal to the strength of its broken bond, while each coordinatively unsaturated anion was assigned a negative charge equal to the strength of its broken bonds. Coordinatively unsaturated cations with a charge between +0.5 and +1.0 v.u. were assumed to form singly hydroxylated surface groups and were therefore counted as a single site. Similarly, coordinatively unsaturated anions with a charge between −0.5 and −1.0 v.u. were assumed to form singly protonated surface groups and were counted as a single site. Coordinatively unsaturated cations with a charge between +1.5 and +2.0 or coordinatively unsaturated anions with a charge between −1.5 and −2.0 were assumed to doubly hydroxylate or doubly protonate, respectively, and were counted as two sites. In other words, coordinatively unsaturated atoms were assumed to bond with H^+ or OH^- only if reaction with these species resulted in a net reduction of the partial charge on that atom. It is implicitly assumed in this approach that the surface hydroxyl site density is equivalent to the total or maximum reactive site density.

Table 1 contains a summary of the calculated sites/nm^2 for each plane on each mineral considered in this study using the five estimation methods. To compare estimated site densities derived for individual faces with experimentally-determined site densities from whole crystals, some account must be made of the relative abundances of the various faces that occur on the whole crystals. Averages of both common cleavage and common low-index growth planes for twelve minerals were calculated as described below. Averages of cleavage planes for each mineral are given in table 2, and averages of growth planes are given in table 3. A complete list of the depths and coordination states available on the world wide web at: http://www.jhu.edu/~eps/faculty/sverjensky/koretsky.html. Also available at this world wide web site are additional color diagrams of the surfaces and surface sites described in this study.

All mineral structures in this study were taken from the crystal structure library provided with the program CrystalMaker©. The structures were used without modification, except in the case of low albite. The albite structure was input using data from the Amelia albite neutron diffraction study of Harlow and Brown (1980). Unit-cell dimensions and sources (as cited in CrystalMaker©) are given in table 4.

RESULTS

α-Quartz (SiO_2)

α-Quartz is a tectosilicate mineral, in which all the Si atoms in the bulk of the mineral are tetrahedrally coordinated by four O atoms. All the Si-O bond lengths in α-quartz are not equal: each Si is bonded to two O atoms at a distance of 1.605 Å and to two O atoms at a distance of 1.613 Å. Because these two Si-O bonds are of different lengths, they are also of unequal strength, so cleavage planes that break the same number of Si-O bonds may in fact not be equal in terms of the total strength of bonds broken.

α-Quartz does not have any excellent cleavages, but it does have a number of preferred cleavage planes (Bloss and Gibbs, 1963). The best cleavage planes are {101},

TABLE 1

Summary of the calculated numbers of sites/nm² for each mineral surface considered in this study

Mineral (Formula)	Plane	Method 1	Method 2	Method 3	Method 4	Method 5
α-Quartz (SiO_2)	{100}	7.5	7.5	18.8	11.3	7.5
	{001}	9.6	9.6	14.3	9.6	9.6
	{110}	8.7	6.5	10.9	8.7	8.7
	{011}	5.9	5.9	14.8	8.9	5.9
	{111}	7.9	7.9	13.9	9.9	7.9
Periclase (MgO)	{100}	23.6	23.6	23.6	11.8	0
	{110}	33.3	16.7	16.7	8.3	16.7
	{111}	40.8	13.6	27.2	13.6	13.6
Rutile (TiO_2)	{100}	14.7	14.7	14.7	7.4	14.7
	{001}	19.0	14.2	14.2	9.5	14.2
	{110}	10.4	10.4	26.0	15.6	10.4
	{101}	15.9	15.9	15.9	8.0	15.9
	{111}	21.0	17.5	17.5	10.5	17.5
Goethite (α-FeOOH)	{100}	14.4	14.4	21.6	7.2	0
	{010}	17.4	13.1	17.4	8.7	8.7
	{001}	20.0	10.0	20.0	13.4	10.0
Corundum (α-Al_2O_3)	{100}	25.9	16.2	19.4	12.9	16.2
	{001}	30.5	20.4	20.4	15.3	5.1
	{1-12}	16.4	16.4	24.6	16.4	16.4
Hematite (Fe_2O_3)	{100}	23.1	14.4	14.4	8.6	14.4
	{001}	27.3	18.2	18.2	13.6	4.5
	{1-12}	14.5	14.5	21.7	14.5	14.5
Andalusite (Al_2SiO_5)	{100}	13.7	11.4	15.9	11.4	11.4
	{010}	13.8	11.5	16.2	11.5	13.8
	{001}	13.0	11.4	21.1	13.0	11.4
	{011}	10.6	10.6	21.3	13.3	10.6
Kaolinite ($Al_2Si_2O_5(OH)_4$)	{010}	16.4	10.9	12.3	8.2	9.6
	{001}	0	0	21.8	13.1	0
	{110}	7.9	6.6	14.6	11.9	5.3
Sillimanite (Al_2SiO_5)	{100}	9.0	9.0	22.6	13.6	9.0
	{010}	18.5	9.3	13.9	9.3	16.2
	{001}	13.9	12.2	15.7	10.4	10.4
	{110}	12.9	11.3	11.3	8.1	12.9
Sanidine ($KAlSi_3O_8$)	{010}	7.3	7.3	19.9	12.7	7.3
	{001}	7.1	7.1	19.6	12.5	7.1
Anorthite ($CaAl_2Si_2O_6$)	{010}	11.5	8.6	10.6	5.8	4.8
	{001}	11.4	7.6	10.5	5.7	5.7
Albite ($NaAlSi_3O_8$)	{010}	11.5	9.6	9.6	5.8	3.8
	{001}	11.5	7.7	11.5	5.8	3.8

Method 1:Each broken bond counted as one site

Method 2: Each coordinateively unsaturated atom counted as one site.

Method 3: Each atom, regardless of coordinative saturation state, within 1.4 A of mineral surface, counted as one site.

Method 4: Each oxygen atom, regardless of saturation state, within 1.4 A of mineral surface, counted as one site.

Method 5: Each cation with a charge of +0.5 to +1.0 counted as one site, each cation with a charge of +1.5 to +2.0 counted as two sites. Each anion with a charge of −0.5 to −1.0 counted as one site, each anion with a charge −1.5 to −2.0 counted as two site.

TABLE 2

Summary of the average sites/nm² for cleavage faces of the minerals considered in this study

Mineral (Formula)	Average Type	Face(s) Used	Method 1	Method 2	Method 3	Method 4	Method 5
α-Quartz (SiO_2)	Low index faces	{100}, {001}, {011}, {110}, {111}	7.9	7.5	13.8	9.3	7.9
Periclase (MgO)	Cleavage	{100}	23.6	23.6	23.6	11.8	0
Rutile (TiO_2)	Cleavage	{110}, {100}	12.6	12.6	20.4	11.5	12.6
	Weighted	.6*{110}, .2*{101}, .2*{100}	12.4	12.4	21.7	12.4	12.4
Goethite (α-FeOOH)	Cleavage	{010}	17.4	13.1	17.4	8.7	8.7
Corundum (α-Al_2O_3)	Parting	{001}	30.5	20.4	20.4	15.3	5.1
Hematite (Fe_2O_3)	Parting	{001}	27.3	18.2	18.2	13.6	4.5
Andalusite (Al_2SiO_5)	Cleavage	{100}	13.7	11.4	15.9	11.4	11.4
Sillimanite (Al_2SiO_5)	Cleavage	{010}	18.5	9.3	13.9	9.3	16.2
Kaolinite ($Al_2Si_2O_5(OH)_4$)	Cleavage	{001}	0	0	21.8	13.1	0
Sanidine ($KAlSi_3O_8$)	Cleavage	{010}, {001}	7.2	7.2	19.8	12.6	7.2
Anorthite ($CaAl_2Si_2O_6$)	Cleavage	{010}, {001}	11.5	8.1	10.6	5.8	5.3
Albite ($NaAlSi_3O_8$)	Cleavage	{010}, {001}	11.5	8.7	10.6	5.8	3.8

Method 1: Each broken bond counted as one site

Method 2: Each coordinateively unsaturated atom counted as one site.

Method 3: Each atom, regardless of coordinative saturation state, within 1.4 A of mineral surface, counted as one site.

Method 4: Each oxygen atom, regardless of saturation state, within 1.4 A of mineral surface, counted as one site.

Method 5: Each cation with a charge of +0.5 to +1.0 counted as one site, each cation with a charge of +1.5 to +2.0 counted as two sites. Each anion with a charge of −0.5 to −1.0 counted as one site, each anion with a charge −1.5 to −2.0 counted as two site.

{011}, and {112}, followed by less pronounced cleavages on {001}, {111}, {511}, {100}, and then perhaps by cleavages on {302} and {110}. Common growth faces on α-quartz crystals include {100}, {011}, {101}, and {111} (Zoltai and Stout, 1984). Because α-quartz used in many adsorption and dissolution studies has been crushed and presumably rounded, numerous faces will be exposed at the surface. For simplicity, the following low-index faces were considered in this study: {100}, {001}, {110}, {011}, and {111}.

Figure 2 illustrates the coordinatively unsaturated atoms that will occur on the ideal quartz {100}, {001}, {011}, {111}, and {110} surfaces chosen in this study. Note that the coordinatively unsaturated Si and O atoms on quartz {001} are bonded to one another. Similarly, on quartz {111} one pair of the coordinatively unsaturated Si and O atoms are bonded to each another, while the other coordinatively unsaturated Si and O atoms are independent of each another.

The predicted site densities for the five quartz surfaces range from 5.9 to 18.8 sites/nm² (table 1). The "average" quartz values given in tables 2 and 3 were calculated by averaging the predicted site densities for the {100}, {001}, {011}, {110}, and {111} surfaces using each of the five estimation methods. Since none of these cleavage or growth planes is very much preferred over the others, the site densities for each face were given equal weight in the averages.

Spectroscopic evidence.–If it is assumed that in contact with air, coordinatively unsaturated Si and O atoms at the quartz surface will protonate or hydroxylate to reduce their partial charges and regain their bulk coordination number, then the presence of both isolated (>SiOH) and geminal (>Si(OH)$_2$) groups on quartz crushed in air should be expected from the results of this study. In agreement with this prediction, surface hydroxyl groups have been observed on α-quartz powders crushed and measured in air using reflectance infrared spectroscopy (Gallei and Parks, 1972; Koretsky and others,

1997). Koretsky and others (1997) observed a single band at 3745 cm^{-1} on crushed natural and synthetic samples of quartz, which they attributed to isolated >SiOH groups at the mineral surface. Evidence of H-bonded OH groups was also found after heating to temperatures as high as 600°C, although no definitive identification of these groups as geminal $>Si(OH)_2$, vicinal >Si(OH), or residual H_2O H-bonded surface groups was possible.

TABLE 3

Summary of the average sites/nm² for growth faces of the minerals considered in this study

Mineral (Formula)	Average Type	Face(s) Used	Method 1	Method 2	Method 3	Method 4	Method 5
α-Quartz (SiO_2)	Low index faces	{100}, {001} {011}, {110} {111}	7.9	7.5	14.5	9.7	7.9
Periclase (MgO)	Growth	{100}, {111}	32.2	18.6	25.4	12.7	6.8
Rutile (TiO_2)	Growth	{100}, {110}, {101}, {111}	15.5	14.6	18.5	10.4	14.6
Goethite (α-FeOOH)	Growth	{010}	17.4	13.1	17.4	8.7	8.7
Corundum (α-Al_2O_3)	Growth	{001}	30.5	20.4	20.4	15.3	5.1
Hematite (Fe_2O_3)	Growth	{001}	27.3	18.2	18.2	13.6	4.5
Andalusite (Al_2SiO_5)	Growth	{001}, {011}	11.8	11.0	21.2	13.2	11.0
Kaolinite ($Al_2Si_2O_5(OH)_4$)	Growth	{010}, {001}, {110}	8.1	5.8	16.2	11.1	5.0
Sillimanite (Al_2SiO_5)	Growth	{001}, {110}, {010}	15.1	10.9	13.6	9.3	13.2
Sanidine ($KAlSi_3O_8$)	Growth	{001}, {010}	7.2	7.2	19.8	12.6	7.2
Anorthite ($CaAl_2Si_2O_6$)	Growth	{010}, {001}	11.5	8.1	10.6	5.8	5.3
Albite ($NaAlSi_3O_8$)	Growth	{010}, {001}	11.5	8.7	10.6	5.8	3.8

Method 1: Each broken bond counted as one site
Method 2: Each coordinatively unsaturated atom counted as one site
Method 3: Each atom, regardless of coordinative saturation state, within 1.4 A of mineral surface, counted as a one site.
Method 4: Each oxygen atom, regardless of saturation state, within 1.4 A of mineral surface, counted as one site.
Method 5: Each cation with a charge of +0.5 to +1.0 counted as one site, each cation with a charge of +1.5 to+2.0 counted as two sites. Each anion with a charge of -0.5 to -1.0 counted as one site, each anion with a charge -1.5 to -2.0 counted as two sites.

TABLE 4

Unit cell dimensions and sources for the minerals considered in this study as given by CrystalMaker©

Mineral	a (Å)	b (Å)	c (Å)	α (°)	β (°)	γ (°)	Source
α-Quartz (298)	4.49137	4.49137	5.4047	90	90	120	Kihara (1990)
Periclase	4.1200	4.1200	4.1200	90	90	90	constructed from radii
Rutile	4.5937	4.5937	2.9581	90	90	90	Wyckoff (1960)
Goethite	9.9500	3.0100	4.6200	90	90	90	Szytula and others (1968)
Hematite	5.0380	5.0380	5.0380	90	90	120	-
Corundum	4.7617	4.7617	12.9947	90	90	120	Finger and Hazen (1978)
Kaolinite	5.1400	8.9300	7.3700	91.8	104.5	90	Wyckoff (1960)
Andalusite	7.8985	7.8985	5.5590	90	90	90	Wyckoff (1960)
Sillimanite	7.4856	7.6738	5.7698	90	90	90	Wyckoff (1960)
Sanidine	8.5600	13.0300	7.1700	90	116	90	computer simulation
Anorthite	8.1730	12.8690	14.1650	93.11	115.91	91.26	Wainwright and Starkey (1971)
Albite	8.1420	12.7850	7.1590	94.19	116.61	87.68	Harlow and Brown (1980)

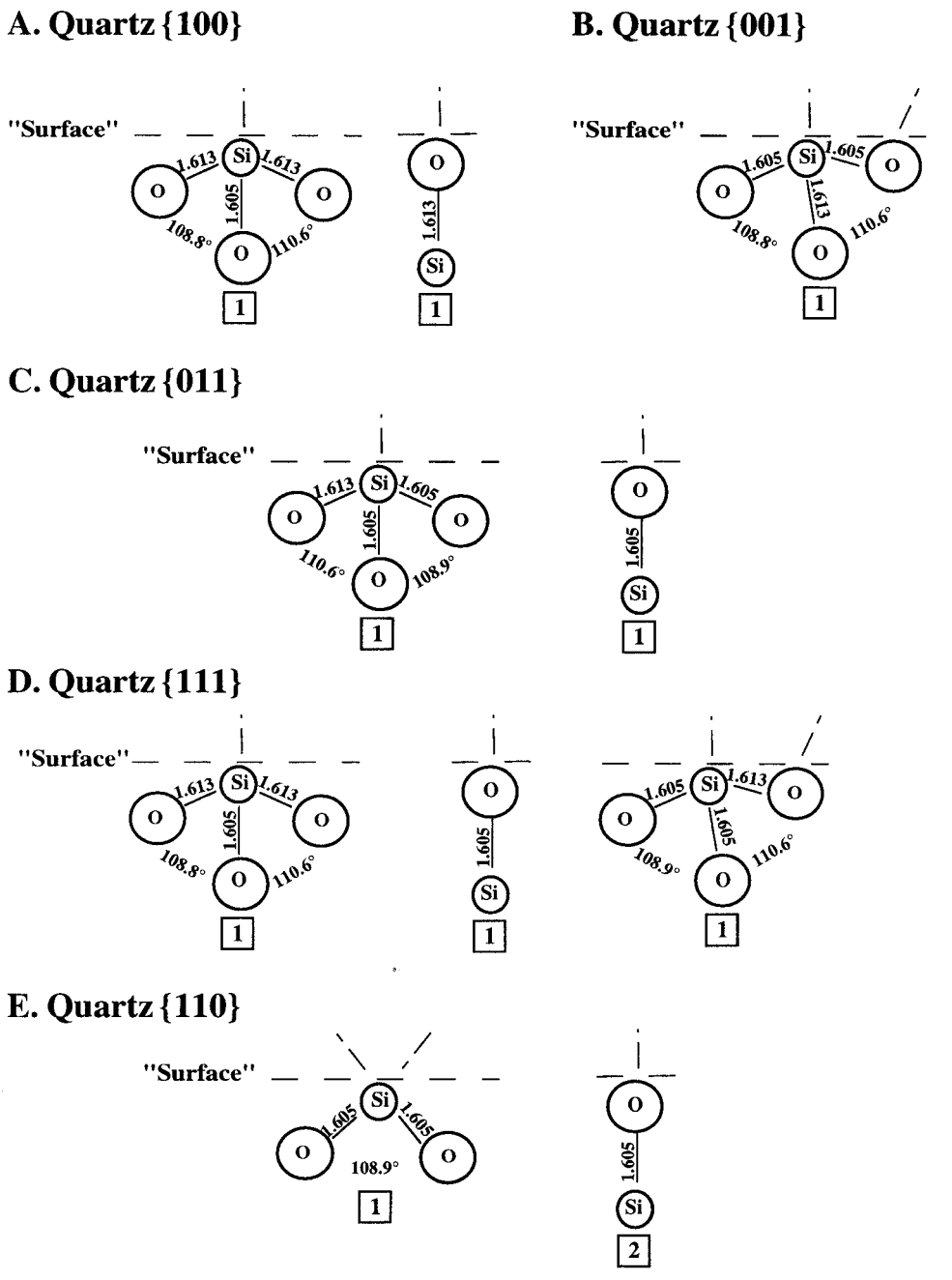

Fig. 2. Schematic depiction of the coordinatively unsaturated atoms that occur on quartz. In this and in all subsequent figures, horizontal dashed lines represent the termination of the bulk mineral structure, while vertical or inclined dashed lines represent broken bonds at that surface. The number of each structure type which occur in one unit cell is indicated by the boxed number beneath each structure. Bond lengths are in Å. Bond lengths and angles are values taken from the bulk crystal structure (that is, it was assumed that no reconstruction or relaxation occurs at the surface) given in CrystalMaker©. Structure of unsaturated atoms which occur on (A) quartz {100}, (B) quartz {001}, (C) quartz {011}, (D) quartz {111}, and (E) quartz {110} surfaces.

TABLE 5

Calculated and experimental site densities (sites/nm^2) from the literature for minerals considered in this study

Mineral	Face(s)	Calculated	Experimental	Source
α-Quartz	-	-	11.4 ± 0.2	a1
	{001}	9.6	-	b
	{101}	6.0	-	b
	-	-	6.3 ± 0.1	a2
	-	-	3.5	c
Periclase	-	-	16	d1
	-	-	36	d2
	{100}	11	-	d3
	{110}	8	-	d3
	{111}	6.5	-	d3
	-	-	16-18	e1
	-	-	8	e2
Rutile	-	-	12.5 ± 1.0	a1
	-	-	8.4	f
	-	-	12.4	g
	-	8	-	h1
	-	-	2.7-7.1	i
	{110}	10.2	-	j
	{101}	15.9	-	j
	{100}	14.7	-	j
	-	-	13	k1
	-	-	7.56	h2
	-	-	6.45	h3
	-	-	6.77	h4
	-	-	5 ± 0.7	l
	-	-	6.8	c
Goethite	-	-	20.1 ± 0.7	a3
	-	-	18.0 ± 0.7	a3
	-	-	18.8 ± 0.5	a3
	-	-	16.4 ± 0.7	a4
	-	-	18	t2
	{010}	13.3	-	m
	{010}	14.4	-	m
	{010}	15.1	-	m
	{010}	16.4	-	m
	-	-	10 ± 0.8	l
	-	16.8	-	k2
	-	-	1.68	s
	{110},{021}	15-16	-	n
Corundum	-	-	13 ± 1.2	l
	-	-	2.7	c
	-	-	1.7	r

TABLE 5
(continued)

Mineral	Face(s)	Calculated	Experimental	Source
Hematite	-	-	22.0 ± 0.4	a1
	-	-	8.52	h2
	-	-	10.23	h5
	-	-	8.13	h3
	-	-	7.76	h6
	-	-	7.94	h4
	-	-	6.79	h7
	-	-	5.6	o
	-	-	4.3 to 9.1	i
	-	-	24.3	c
	-	-	15	t1
	-	-	19	t2
	{100}	8.7	-	m
	{110}	15.0	-	m
	{012}	14.6	-	m
	{104}	15.9	-	m
	{018}	9.5	-	m
	{113}	12.4	-	m
	{001}	13.7	-	m
	-	9	-	h1
Albite	-	-	37	p
	-	-	8.4	q

Sources: (a1) Yates and others (1977): tritium exchange method. (a2) Yates and others (1977): tritium exchange method, pretreated by heating at 420°C, 24 hrs. (a3) Yates and others (1977): tritium exchange method, extrapolating long term data. (a4) Yates and others (1977): tritium exchange method, extrapolating data for extraction times of less than 15 min. (b) Boehm (1966) quoting Schneider (ms). (c) James and Parks (1982) citing Huang (ms), using acid-base titrations. (d1) Anderson, Horlock, and Oliver (1965): H_2O adsorption/desorption measurements in vacuum at 300°C. (d2) Anderson, Horlock, and Oliver (1965): H_2O adsorption/desorption measurements at room temperature. (d3) Anderson, Horlock, and Oliver (1965). (e1) Derouane and others (1972): NMR spectroscopy, sample heated to 300°C. (e2) Derouane and others (1972): NMR spectroscopy, sample heated to 1000°C. (f) Hollabaugh and Chessick (1961): H_2O desorption. (g) Jones and Hockey (1972): H_2O desorption. (h1) Morimoto, Nagao, and Tokuda (1969): calculated using crystallographic data. (h2) Morimoto, Nagao, and Tokuda (1969): H_2O adsorption isotherm method; Sample I, pretreated by heating to 250°C. (h3) Morimoto, Nagao, and Tokuda (1969): H_2O adsorption isotherm method; Sample I, heating to 600°C. (h4) Morimoto, Nagao, and Tokuda (1969): H_2O adsorption isotherm method; Sample I, heating to 800°C. (h5) Morimoto, Nagao, and Tokuda (1969): H_2O adsorption method; Sample II, heating to 250°C. (h6) Morimoto, Nagao, and Tokuda (1969): H_2O adsorption method; Sample II, heating to 600°C. (h7) Morimoto, Nagao, and Tokuda (1969): H_2O adsorption method; Sample II, heating to 800°C. (i) Boehm (1971): using various adsorbates in solution. (j) Jones and Hockey (1971b). (k1) Yates (ms): weight loss measurements. (k2) Yates (ms). (l) Altmann (ms): tritium exchange method. (m) Barron and Torrent (1996). (n) Rustad, Felmy, and Hay (1996b). (o) McCafferty and Zettlemoyer (1971): H_2O adsorption after outgassing to 475°C. (p) Blum and Lasaga (1991): acid-base titrations. (q) Blum and Lasaga (1991): Na^+ release. (r) Boily and Fein (1996): acid-base titrations. (s) Lövgren, Sjöberg, and Schindler (1990): acid-base titrations. (t1) Hsi and Langmuir (1985): tritium exchange method on a natural sample. (t2) Hsi and Langmuir (1985): tritium exchange method on synthetic sample.

Much surface IR and surface NMR work has been completed on high-surface area amorphous silica (Little, 1966; Hair, 1967; Iler, 1979; Bergna, 1994). The results of numerous studies suggest that approx 4.6 OH/nm^2 occur on amorphous silica, of which 82.5 percent are vicinal or isolated >SiOH groups, and the remaining 17.5 percent are geminal >Si(OH)$_2$ groups (Bergna, 1994).

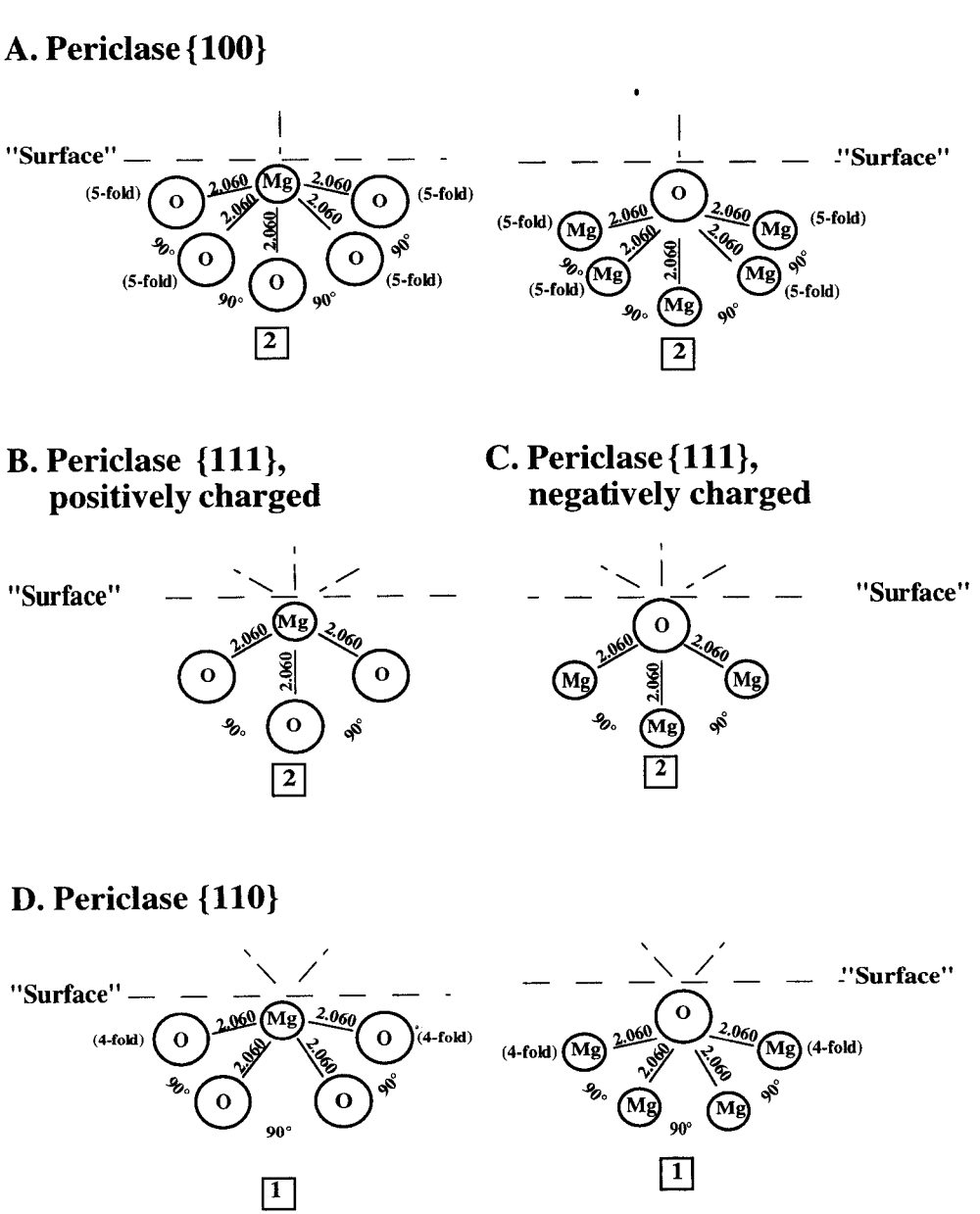

Fig. 3. Schematic depiction of the coordinatively unsaturated atoms that occur on periclase. In this, and in subsequent figures, numbers in parentheses indicate the coordination number of atoms that are not coordinatively saturated. Structure of unsaturated atoms which occur on (A) periclase {100}, (B) the positively charged periclase {111} surface, (C) the negatively charged periclase {111} surface, and (D) periclase {110}.

between coordinatively unsaturated atoms is indicated in figure 3A and D and in all subsequent figures by notations next to each coordinatively unsaturated atom indicating the actual coordination number (before protonation or hydroxylation).

Estimated site densities for the periclase {100}, {111}, and {110} surfaces range from 0 to 40.8 sites/nm^2 (table 1). The {100} face of periclase cleaves perfectly, whereas {111} is only a poor cleavage plane. Therefore, the site densities for the {100} face are recom-

mended as average periclase cleavage values (table 2). Periclase growth faces may also include {111}, so the unweighted average of the {111} and {100} site densities are given as average periclase growth face site densities (table 3).

Spectroscopic evidence.–Infrared spectra of periclase contain both a sharp band at 3752 cm^{-1} and a broad band centered at 3610 cm^{-1} (Anderson, Horlock, and Oliver, 1965). These were interpreted by Anderson, Horlock, and Oliver as isolated >MgOH surface groups (3752 cm^{-1}) and hydrogen-bonded surface OH groups (3610 cm^{-1}). Tsyganenko and Filimonov (1973) concluded from the same spectra that the two bands represent two different types of hydroxyl groups on periclase {100}, due to hydroxylation of a 5-fold coordinated Mg atom and to protonation of a 5-fold coordinated O atom.

It is difficult to compare our results directly with those of Anderson, Horlock, and Oliver (1965), because the surface planes actually present on their prepared periclase crystals were not reported. However, on periclase {100}, two types of surface >MgOH groups might form, corresponding to the two bands observed by Anderson, Horlock, and Oliver (1965), if the 5-fold coordinated Mg and O atoms at the surface hydroxylate and protonate, respectively, to regain their bulk coordination numbers. One set of these surface hydroxyl groups would then be $>Mg^{VI}OH$ groups with 6-fold coordinated Mg atoms and 2-fold coordinated O atoms (from hydroxylation of 5-fold coordinated surface Mg atoms), whereas the other set of surface hydroxyl groups would be bridged $>Mg_6OH$ groups with both 6-fold coordinated O and Mg atoms (from protonation of 5-fold coordinated surface O atoms). However, consideration of the partial charges (+0.37 and −0.37) on these two atoms indicates that hydroxylated surface groups may not form at all on periclase {100}.

On the periclase {111} and {110} faces, at least two types of surface hydroxyl groups are expected on each surface. On periclase {111}, the 3-fold coordinated Mg atoms may hydroxylate to form $>Mg^{IV}OH$ groups with 4-fold coordinated Mg atoms, whereas the 3-fold coordinated O atoms may protonate to form bridged $>Mg_3OH$ groups with 6-fold coordinated Mg atoms. The differing coordination numbers of the Mg and O atoms in these two surface hydroxyl groups should lead to two distinguishable bands in the infrared. Similarly, on periclase {110}, the 4-fold coordinated Mg atoms may hydroxylate to form $>Mg^{V}OH$ groups, whereas the 4-fold coordinated O atoms may protonate, forming bridged $>Mg_4OH$ groups. Again, this should lead to two distinguishable bands in the infrared. Therefore, if either the {110} or the {111} surfaces dominated the sample of periclase used by Anderson, Horlock, and Oliver (1965), then one of these two sets of two types of hydroxyl groups may have contributed to the presence of the two distinct hydroxyl bands observed in the infrared.

Other estimates.–The number of hydroxyl groups at the periclase surface has also been calculated by Anderson, Horlock, and Oliver (1965) based on the periclase crystal structure for the {100}, {110}, and {111} faces (table 5). Densities of surface OH groups were calculated by assuming that H_2O molecules dissociate over the periclase surface such that each "near-surface" Mg adds a hydroxyl and each "near-surface" O adds a hydrogen, regardless of coordinative saturation state.

Rutile (TiO_2)

In the rutile structure, all Ti atoms are in octahedral coordination with respect to the O atoms and all O atoms are coordinated to three Ti atoms. The rutile octahedra share edges to form chains that are cross-linked by the sharing of corners (Klein and Hurlbut, 1993). Rutile has a good cleavage on {110}, as well as a moderate cleavage on {100}, (Deer, Howie, and Zussman, 1993). Common growth faces include {110}, {100}, {101}, and {111}, (Zoltai and Stout, 1984). The {100}, {001}, {110}, {101} and {111} faces were considered in this study.

Figure 4 illustrates the coordinatively unsaturated atoms predicted to occur on these five ideal rutile surfaces. The estimated site densities for the rutile surfaces considered in

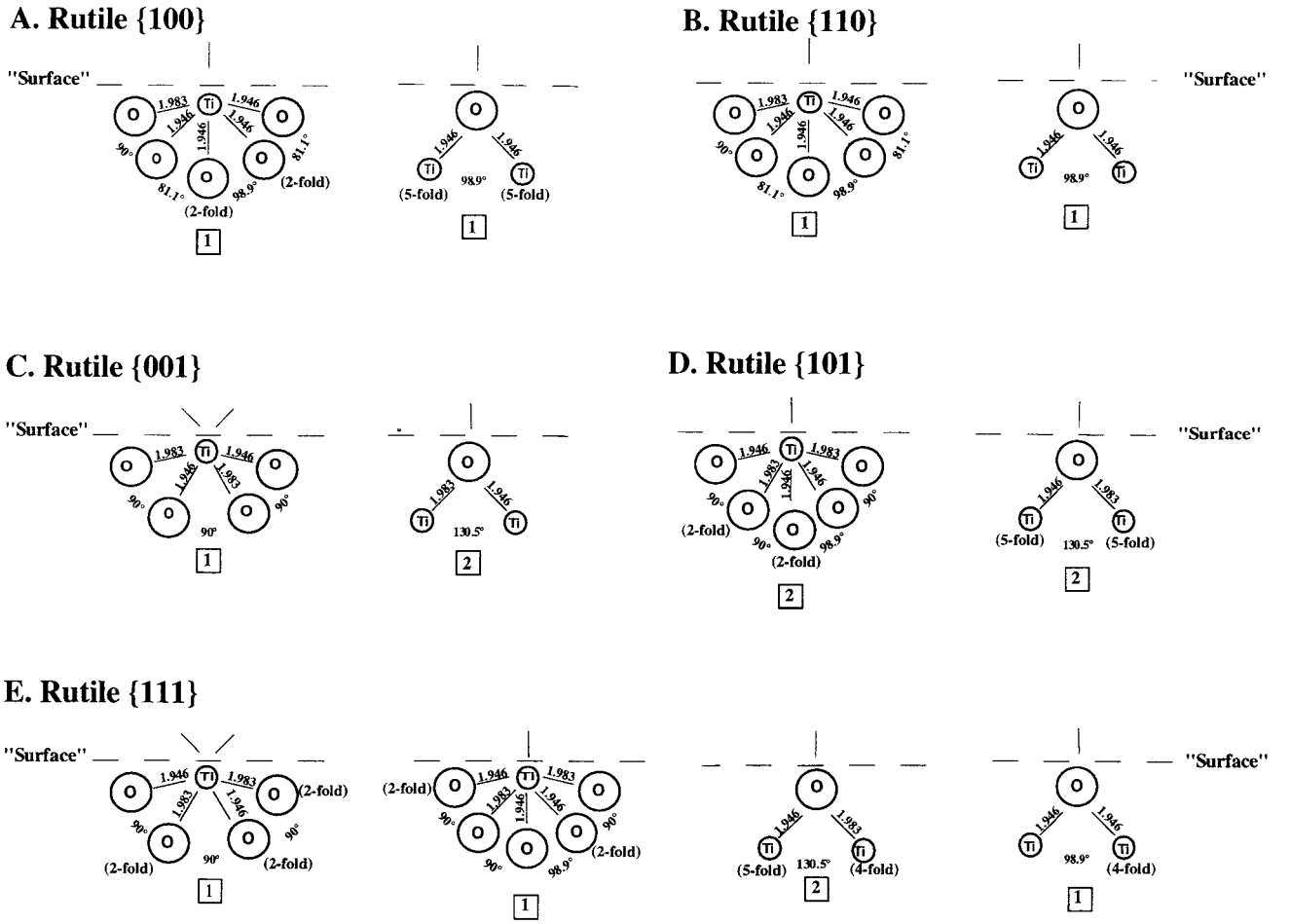

Fig. 4. Schematic depiction of the coordinatively unsaturated atoms that occur on rutile. Structure of coordinatively unsaturated atoms on (A) rutile {100}, (B) rutile {110}, (C) rutile {001}, (D) rutile {101}, and (E) rutile {111}.

this study range from 7.4 to 26.0 sites/nm^2 (table 1). Jones and Hockey (1971b) assumed that crystallized rutile has surfaces composed of approx 60 percent {110}, 20 percent {101}, and 20 percent {100}. For comparison, the same weighted average was used in this study (table 2). In addition, the predicted site densities for the good {110} and the moderate {100} cleavage plane values were simply averaged (table 2). An unweighted average of the predicted site densities for the {100}, {110}, {101}, and {111} was used to estimate average site densities for growth faces (table 3).

Spectroscopic evidence.–The ideal rutile cleavage planes considered in this study ({110}, {100}, and {101}) have only two types of coordinatively unsaturated atoms: 5-fold coordinated Ti atoms and 2-fold coordinated O atoms. In contact with air, the Ti^{V} atoms may hydroxylate to regain their bulk coordination number of six, forming $>Ti^{VI}OH$ surface groups, while the O^{II} atoms may protonate to form bridged $>Ti_2OH$ surface groups. These >TiOH and $>Ti_2OH$ surface groups should occur in equal proportions on each of the three rutile cleavage surfaces.

Yates (1961) observed two IR bands at 3680 and 3320 cm^{-1} on rutile after evacuation at 350°C. He attributed the bands to hydrogen bonded and non-hydrogen bonded surface hydroxyl groups. However, it is also possible that these two bands correspond to >TiOH and $>Ti_2OH$ groups. Jones and Hockey (1971a) studied rutile surface hydroxylation using infrared spectroscopy combined with heating studies and dosing experiments using pyridine and HCl. They concluded from these experiments that IR bands at 3650 and 3410 cm^{-1} arise from hydroxylated 5-fold coordinated or 4-fold coordinated surface Ti atoms. Based on the surfaces constructed in this study, however, the two surface OH groups might instead be assigned to >TiOH and $>Ti_2OH$ groups.

Boehm (1971) studied several samples of rutile. He assumed initially that >TiOH and $>Ti_2OH$ groups would be present at the rutile surface. He postulated that the hydroxyl group bonded to a single Ti atom would be rather acidic in character, while the hydroxyl group bonded to two Ti atoms would be more basic. Using a variety of adsorbates, he found evidence of two types of hydroxyl groups on rutile, which he assigned to basic and acidic groups in support of his initial assumption. His results are also consistent with our prediction that these two types of surface OH groups, >TiOH and $>Ti_2OH$, should occur on the cleavage surfaces of rutile.

Other estimates.–Morimoto, Nagao, and Tokuda (1969) assumed that one hydroxyl group forms on each surface metal atom (table 5). Using this method, they calculated site densities for the commonly occurring rutile cleavage planes, {100} and {110}. Jones and Hockey (1971b) assumed that rutile is typically composed of 60 percent {110}, 20 percent {101}, and 20 percent {100} surface planes. They calculated hydroxyl concentrations for each of these faces by assuming that near-surface titanium atoms hydroxylate, whereas near-surface oxygen atoms protonate to regain their bulk coordination numbers (table 5).

Goethite (α-FeOOH)

In the goethite structure, Fe atoms are in 6-fold coordination with respect to the O. Goethite has a perfect cleavage on {010}, as well as common growth faces on {110}, {120}, {121}, {021}, and {010} (Zoltai and Stout, 1984). The goethite {100}, {010}, and {001} faces were considered in this study.

The coordinatively unsaturated atoms predicted to occur on the ideal goethite {100}, {010}, and {001} surfaces are shown in figure 5. The ideal goethite {100} surface has one 5-fold coordinated Fe and one 3-fold coordinated O in an O^{IV} site per surface unit cell (fig. 5A). Because protonation or hydroxylation will not reduce the partial charge of either of these coordinatively unsaturated atoms, no sites are predicted to occur on this surface using the partial charge method of site estimation.

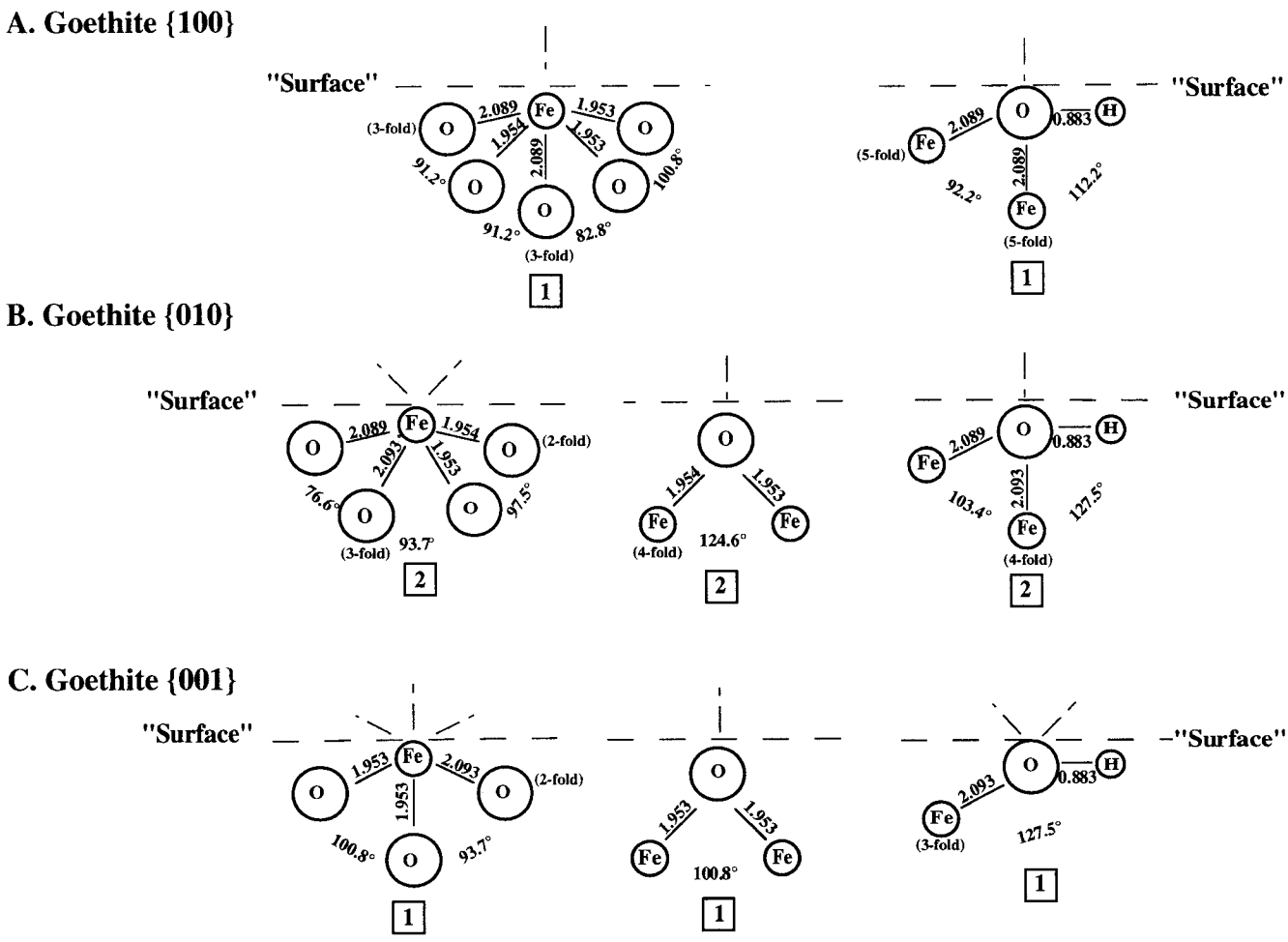

Fig. 5. Schematic depiction of the coordinatively unsaturated atoms that occur on goethite. Structure of coordinatively unsaturated atoms on (A) goethite {100}, (B) goethite {010}, and (C) goethite {001}.

The estimated site densities for the three goethite surfaces range from 0 to 20.0 sites/nm^2 (table 1). Since goethite has only a single good cleavage, on {010}, the goethite {010} site densities are recommended as an average for crushed goethite (table 2). Of the planes considered in this study, {010} probably occurs most often as a growth face on goethite, so these values are recommended for average growth face site densities as well (table 3).

Spectroscopic evidence.–On the ideal goethite {100} surface considered in this study (fig. 5A), two types of surface groups should occur in goethite exposed to air, $>Fe^{VI}OH$ groups (due to hydroxylation of 5-fold coordinated Fe atoms) and $>Fe_2(OH)_2$ groups (due to protonation of 3-fold coordinated O atoms). Thus, it might be expected that two infrared peaks should be observed on platy samples with high {100} surface areas relative to edge plane surface areas. Russell and others (1974) and Parfitt, Russell, and Farmer (1976) measured the infrared spectra of a synthetic goethite with a platy habit. In both studies, three OH infrared bands at 3145, 3486, and 3660 cm^{-1} were found. The 3145 cm^{-1} band was attributed to bulk OH groups, because of its relatively low frequency and because it did not rapidly exchange to form OD groups when the sample was exposed to deuterium. The 3486 cm^{-1} band was attributed to hydrogen bonded surface OH groups, in which the OH was bonded to three Fe atoms and the 3660 cm^{-1} band was attributed to two separate types of non-hydrogen bonded surface OH groups. The observation of two surface OH bands on this goethite sample is also consistent with the existence of the two types of surface OH groups predicted to occur on the {100} goethite in this study.

Other estimates.–Yates (ms) calculated exchangeable proton densities on goethite {100}, {010}, and {001} planes by assuming that near surface iron atoms hydroxylate, while near surface oxygen atoms protonate (table 5). Barron and Torrent (1996) studied goethite {100}, {010}, {110}, and {021}. They chose to consider the surface planes with the least number of coordinatively unsaturated Fe atoms. In cases where there were two or more such planes, the planes with the highest ion density near the surface were chosen. Barron and Torrent counted numbers of singly, doubly, and triply coordinated Fe to find the total sites on a given surface. Rustad, Felmy, and Hay (1996a,b) have also considered the structure of various goethite surface groups. In both studies, it was assumed that no coordinatively unsaturated Fe atoms occur at the surface. Coordinatively unsaturated oxygen atoms were then assumed to protonate until the surface is left with an overall neutral charge. Using molecular statics calculations, the reactivity of surface oxygen atoms on goethite {100}, {110}, {001}, {021}, and {010} was estimated.

Corundum (α-Al_2O_3)

In the corundum structure, all the Al atoms are in octahedral coordination with O, and the O atoms are in tetrahedral coordination with the Al atoms. Corundum does not have a cleavage plane but does have a parting on {001}. Common growth planes include {001}, {101}, {223}, and {221} (Zoltai and Stout, 1984). The {100}, {001}, and {1-12} planes were considered in this study.

The coordinatively unsaturated atoms that are predicted to occur on the three ideal corundum surfaces considered in this study are shown in figure 6. The estimated site densities for these surfaces range from 5.1 to 30.5 sites/nm^2 (table 1). Because corundum has a parting plane on {001}, the {001} site densities are recommended for average crushed corundum (table 2), and because the {001} plane is a common growth face on corundum, these values are recommended for uncrushed corundum as well (table 3).

Spectroscopic evidence.–Morterra and others (1976) used infrared spectroscopy to characterize surface hydroxyl groups on two samples of α-Al_2O_3 prepared from heated transition aluminas. They found a single band between 3733 and 3738 cm^{-1} on both samples, which they attributed to surface $>Al^{VI}OH$ groups. On one of the samples, they also found bands at 3755 to 3757 and 3691 to 3693 cm^{-1}, which they attributed to surface

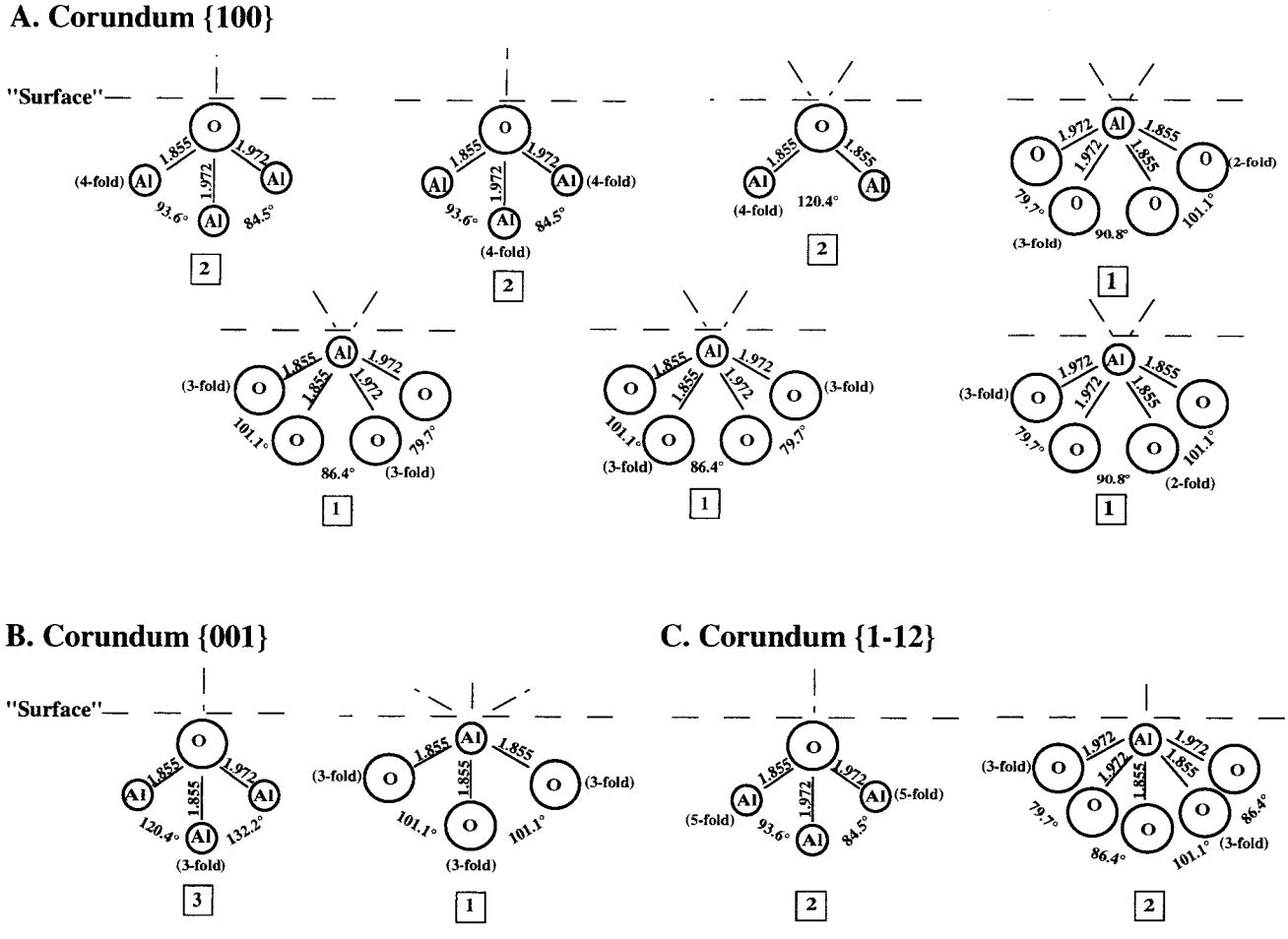

Fig. 6. Schematic depiction of the coordinatively unsaturated atoms that occur on corundum. Structure of coordinatively unsaturated atoms on (A) corundum {100}, (B) corundum {001}, and (C) corundum {1-12}.

$>Al^{IV}OH$ groups due to incompletely reacted transition alumina. In a later study of CO adsorption on α-Al_2O_3, Morterra, Magnacca, and Del Favero (1993) found two bands in the infrared at 3746 and 3668 cm^{-1}, which they assigned to two non-hydrogen bonded surface >AlOH groups. The 3746 cm^{-1} band is described as nearly coincident with the 3733 cm^{-1} band observed in the earlier study.

If the parting corundum {001} plane is primarily present in these samples, two types of surface groups should occur: $>Al_3OH$ groups from protonation of the 3-fold coordinated O atoms in O^{IV} sites, and >AlOH groups from hydroxylation of 3-fold coordinated Al in Al^{VI} sites. This is consistent with the observation by Morterra, Magnacca, and Del Favero (1993) of two distinct non-hydrogen bonded surface >AlOH groups on α-Al_2O_3.

Hematite (α-Fe_2O_3)

Hematite is isostructural with corundum, with Fe^{+3} replacing Al^{+3} in the octahedral sites. Hematite, like corundum, does not have a good cleavage plane but does have partings on {001} and {101}. Common growth faces on hematite include {101}, {001}, and {012} (Zoltai and Stout, 1984). The {100}, {001}, and {1-12} hematite surfaces were considered in this study.

The predicted coordinatively unsaturated atoms for each of the three ideal hematite surfaces are shown in figure 7. The estimated site densities for the three hematite surfaces range from 4.5 to 27.3 sites/nm^2 (table 1). Since hematite has a parting on {001} and no cleavage planes, the {001} site densities were chosen as the average crushed hematite values (table 2). Like corundum, hematite has a common growth face on {001}, so the {001} values are also given as averages for hematite growth planes (table 3).

Spectroscopic evidence.–Hematite samples prepared using different procedures were studied by Rochester and Topham (1979). Samples were measured at temperatures from 423 to 1073 K, heated either in vacuum or under flowing oxygen. Rochester and Topham found eleven bands which they assigned to surface hydroxyl groups. They attributed the complexity of their spectra and the large variety of surface hydroxyl groups in part to the varied morphology of the hematite crystals used in their study. However, they did not attempt to determine the actual morphology of the crystals, so a direct comparison of our predicted site types with their observed spectra is not possible.

Other estimates.–The hematite {100}, {110}, {012}, {104}, {018}, {113}, and {001} surfaces were all considered in a theoretical study of surface site densities by Barrón and Torrent (1996, table 5). As for goethite, they chose surfaces planes in such a way that the number of near-surface coordinatively unsaturated Fe atoms was minimized and counted each singly, doubly, or triply coordinated Fe atom at the surface as a single site. Morimoto, Nagao, and Tokuda (1969) also used crystallographic data to estimate site densities on hematite, assuming in their study that each near surface Fe atom forms one surface hydroxyl group.

Andalusite (Al_2SiO_5)

The andalusite structure consists of chains of edge-shared octahedra parallel to [001]. Half the Al occupy these octahedral sites, while the other half of the Al occupy distorted trigonal bipyramids with irregular 5-fold coordination. Andalusite has two cleavage planes: a good cleavage along {110} and a poor cleavage along {100}. Common growth faces on andalusite include {110}, {011}, and {001} (Zoltai and Stout, 1984). The {100}, {010}, {001}, and {011} faces were considered in this study.

Figure 8 shows the coordinatively unsaturated atoms predicted to occur on the four ideal andalusite surfaces considered in this study. Estimated site densities for these andalusite surfaces range from 10.6 to 21.3 sites/nm^2. Andalusite has a very good

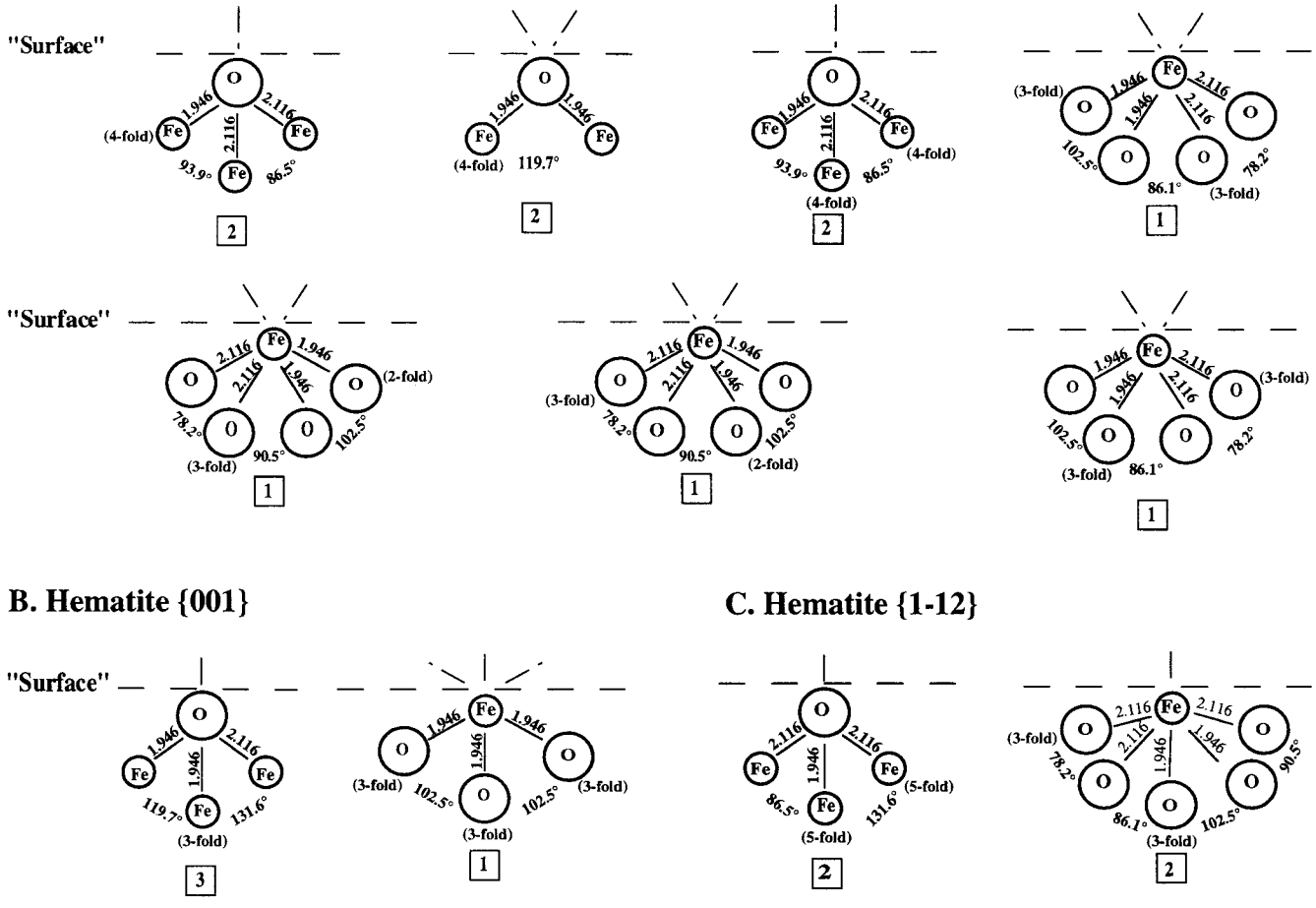

Fig. 7. Schematic depiction of the coordinatively unsaturated atoms that occur on hematite. Structure of coordinatively unsaturated atoms on (A) hematite {100}, (B) hematite {001}, and (C) hematite {1-12}.

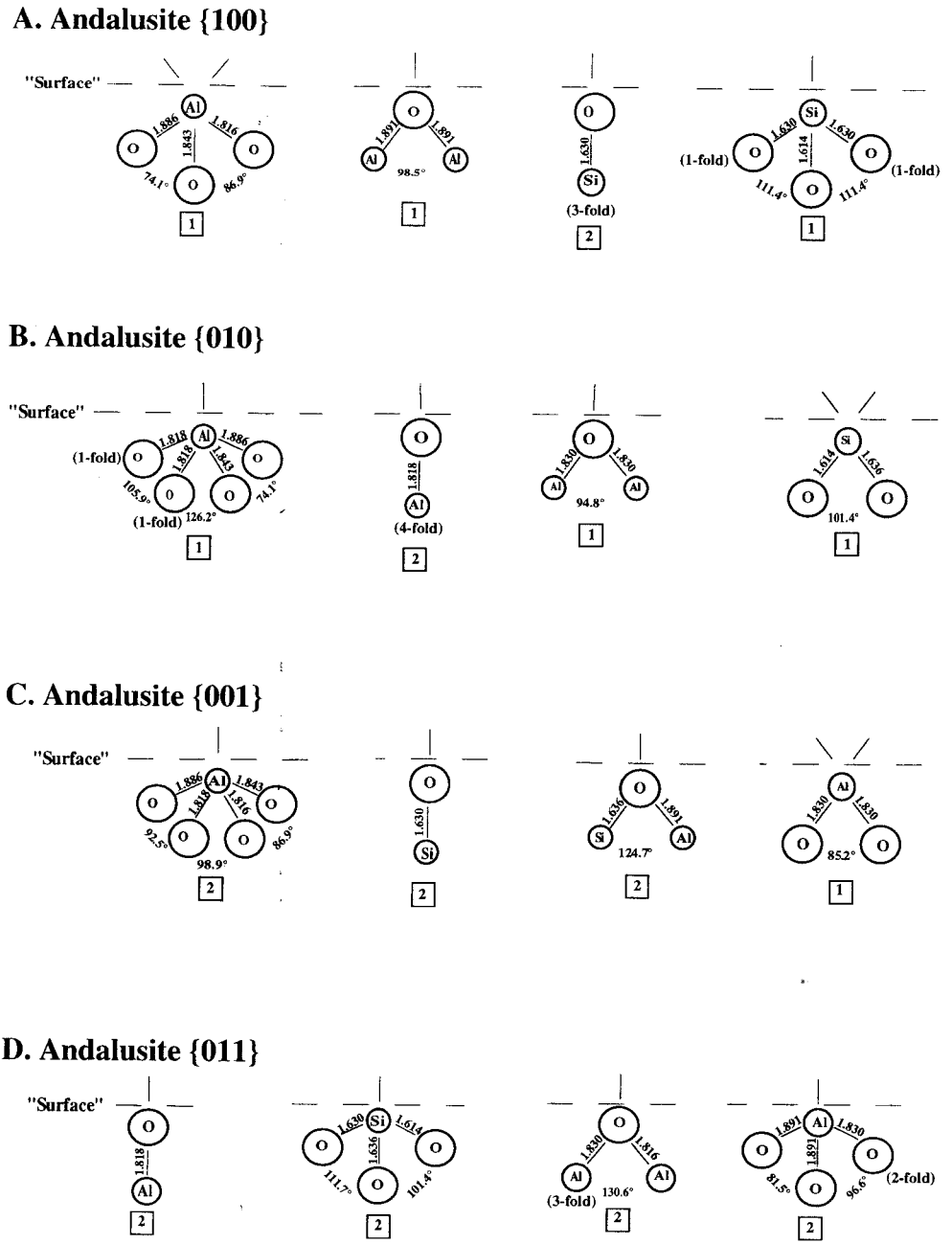

Fig. 8. Schematic depiction of the coordinatively unsaturated atoms that occur on andalusite. Structure of coordinatively unsaturated atoms on (A) andalusite {100}, (B) andalusite {010}, (C) andalusite {001}, and (D) andalusite {011}.

cleavage on {110} and a poor cleavage on {100}. The calculated site densities for the {100} plane were used to give the average cleavage values given in table 2. Common growth planes include the {110}, {011}, and {001} surfaces. The site densities for the {001} and {011} planes were averaged to give the andalusite growth plane values reported in table 3.

Sillimanite (Al_2SiO_5)

In the sillimanite structure, chains of edge-sharing octahedra form parallel to [001]. Half the Al cations in sillimanite occupy these octahedral sites, while the other half of the Al cations are in tetrahedra. The Al and Si tetrahedra alternate to form a double chain parallel to [001]. Sillimanite has a perfect cleavage on {010} as well as common growth faces on {110}, {010}, and {001} (Zoltai and Stout, 1984). The {100}, {010}, {001}, and {110} faces were considered in this study.

The coordinatively unsaturated atoms predicted to occur on the four ideal sillimanite surfaces considered in this study are shown in figure 9. An unreconstructed slice on sillimanite {001} will not leave a charge-neutral surface. Minimizing the strength of broken bonds gives one of two ideal, charged surfaces (fig. 9C and D). Site densities for sillimanite {001} were calculated assuming that on average half the sites will be like those on the positively charged surface and half of the sites will be like those on the negatively charged surface.

The predicted site densities for the four ideal sillimanite surfaces range from 8.1 to 22.6 sites/nm^2 (table 1). Sillimanite has a perfect cleavage on {010}, so the {010} site densities are given in table 2 as average cleavage values for sillimanite. The three common growth faces, {110}, {010}, and {001} were averaged to give the sillimanite growth plane site densities in table 3.

Kaolinite ($Al_2Si_2O_5(OH)_5$)

Kaolinite is a dioctahedral 1:1 layer silicate. Because the tetrahedral and octahedral layers of kaolinite are weakly held together by H-bonding, kaolinite has a perfect cleavage along the {001} basal plane. The edges of kaolinite are frequently bounded by the {110} and {010} planes (Zoltai and Stout, 1984). Therefore, the {001}, {110}, and {010} planes were considered here.

The coordinatively unsaturated atoms predicted to occur on kaolinite {110} and {010} are depicted in figure 10. It is not possible to form a slice of kaolinite on (010) or (0-10) that has no charge. Site densities for kaolinite {010} were predicted assuming that the positively charged kaolinite (0-10) and the negatively charged kaolinite (010) surfaces occur with the same frequency. It was assumed that the {001} cleavage occurs between the kaolinite layers. This creates a surface in which all the cations and anions are still in their fully coordinatively saturated states, such that 0 sites/nm^2 are predicted to occur on this surface using either the number of broken bonds or the number of unsaturated atoms to predict site density. As for the kaolinite {010} surface, it is also not possible to form an uncharged surface on kaolinite {110}. Site densities were again calculated assuming that the positively charged (110) and negatively charged (-1-10) surfaces occur with equal frequency.

Predicted site densities for kaolinite ranged from 0 to 21.8 sites/nm^2 (table 1). Kaolinite has a perfect cleavage on the basal plane, {001}. Therefore, the kaolinite {001} values are used as average site densities for cleaved kaolinite (table 2). Common growth planes on kaolinite include {001}, {010}, and {110}. Therefore, the site densities calculated for these three planes were averaged to give the kaolinite growth face averages reported in table 3.

Sanidine ($KAlSi_3O_8$)

Sanidine, like all feldspars, contains both Al and Si in a tetrahedral framework. In sanidine, the high temperature form of K-feldspar, the Al and Si are completely disordered over the tetrahedral sites. In the CrystalMaker© program, the Al and Si sites are indistinguishable because of this disordering and are referred to as Al^{IV}/Si^{IV}, with a 25 percent probability that any one of these sites will have an Al atom and a 75 percent probability that it will have a Si atom. Sanidine has a perfect cleavage on {001}, and a

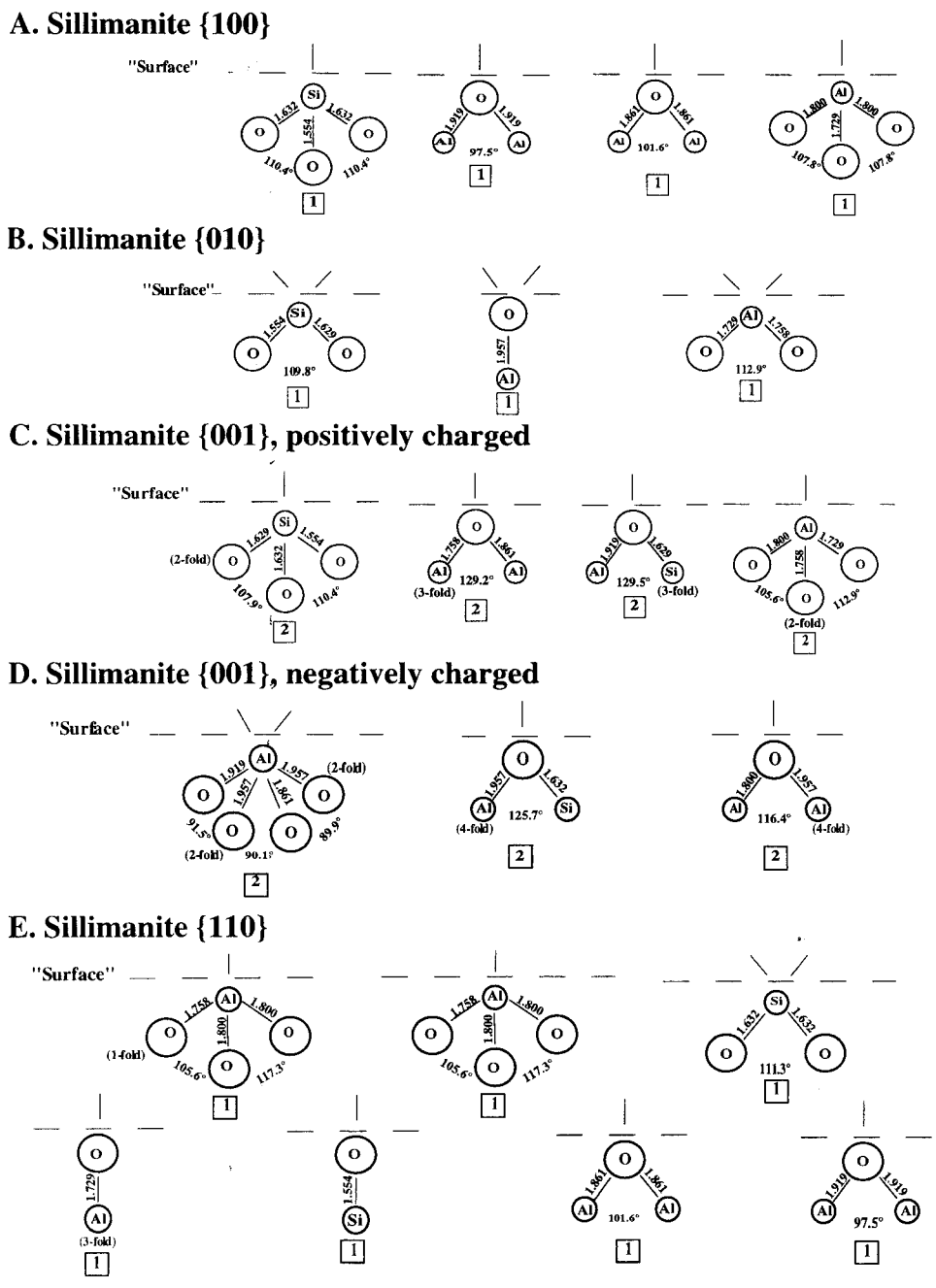

Fig. 9. Schematic depiction of the coordinatively unsaturated atoms that occur on sillimanite. Structure of coordinatively unsaturated atoms on (A) sillimanite {100}, (B) sillimanite {010}, (C) positively charged sillimanite {001}, (D) negatively charged sillimanite {001}, and (E) sillimanite {110}.

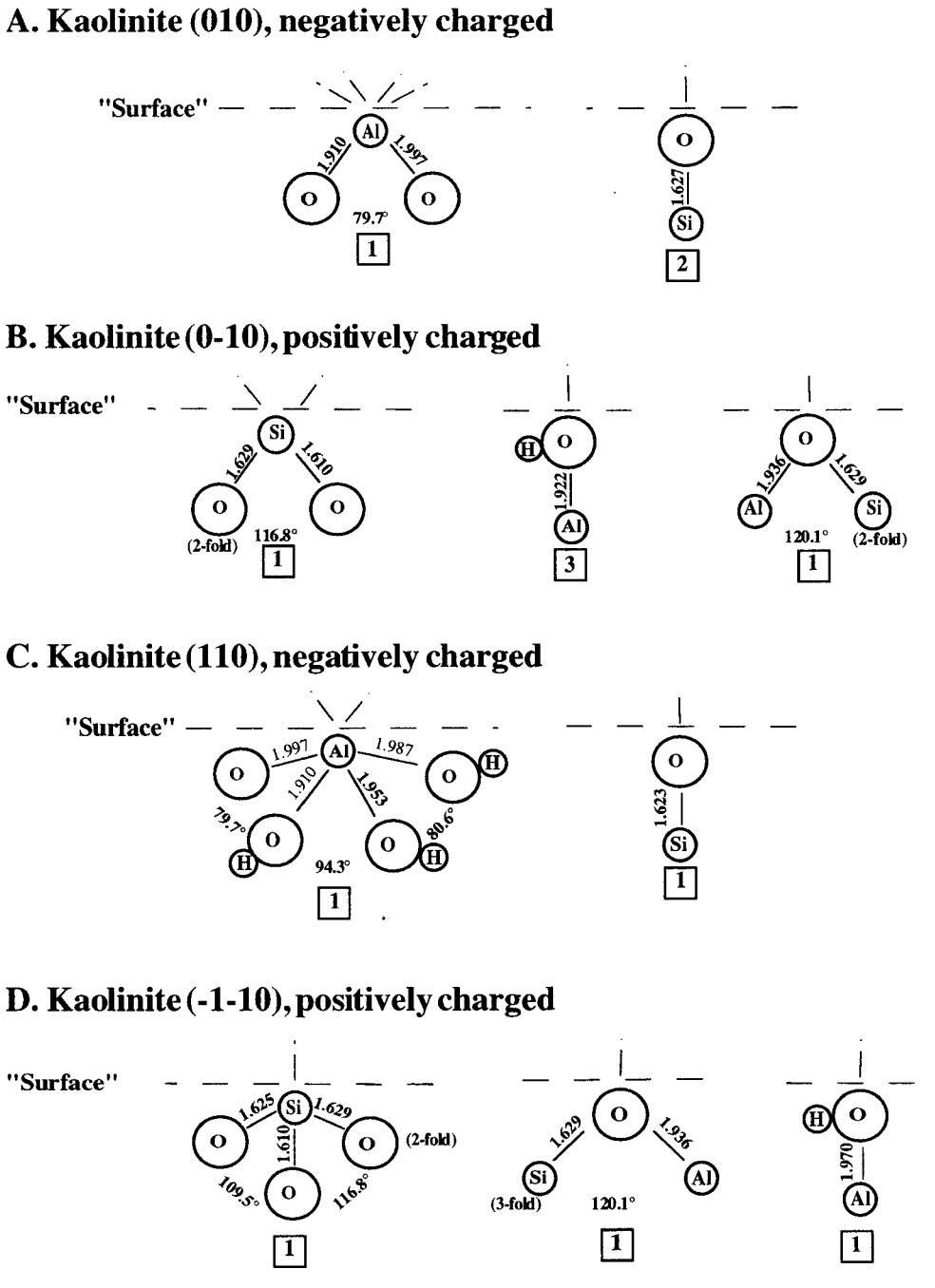

Fig. 10. Schematic depiction of the coordinatively unsaturated atoms that occur on kaolinite. Structure of coordinatively unsaturated atoms on (A) negatively charged kaolinite (010), (B) positively charged kaolinite (0-10), (C) negatively charged kaolinite (110), and (D) positively charged kaolinite (-1-10).

good cleavage on {010}. These two planes are also common growth planes on sanidine (Zoltai and Stout, 1984). For this reason, the {001} and {010} planes were considered in this study.

The coordinatively unsaturated atoms predicted to occur on sanidine {001} and {010} are shown in figure 11. The range of predicted site densities for these two surfaces is from 7.1 to 19.9 sites/nm^2 (table 1). The {010} and {001} are both common cleavage and common growth planes on sanidine. Therefore, the averaged site densities of these two planes are recommended as average sanidine cleavage or growth plane values in tables 2 and 3.

Spectroscopic evidence.–Koretsky and others (1997) used diffuse reflectance Fourier-transform infrared spectroscopy to study surface hydroxyl groups on both synthetic and natural feldspars of various compositions. On K-feldspar samples, including sanidine, a single sharp band at approx 3740 cm^{-1} was observed. This band was assigned to non-hydrogen bonded surface >Si^{IV}OH groups. Some evidence of hydrogen bonded groups was also observed, but Koretsky and others (1997) found no direct evidence of either surface >KOH or surface >AlOH groups.

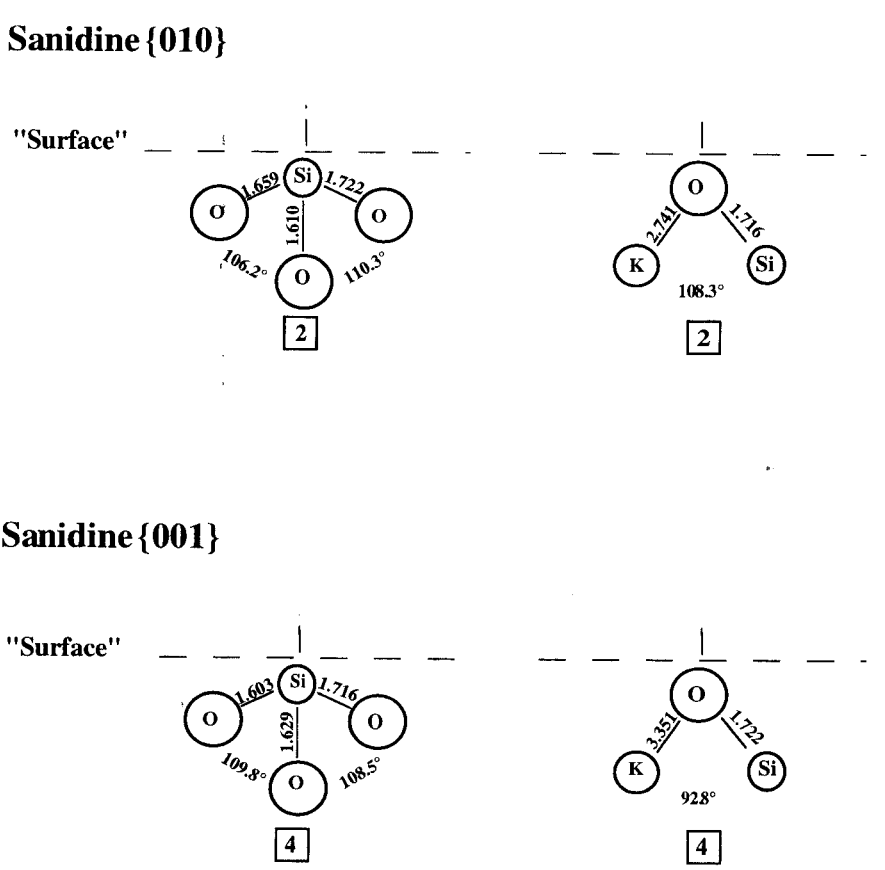

Fig. 11. Schematic depiction of the coordinatively unsaturated atoms that occur on sanidine. Structure of coordinatively unsaturated atoms on (A) sanidine {010} and (B) sanidine {001}. Atoms marked "Si" have a 75 percent probability of being filled by Si atoms and a 25 percent probability of being filled by Al atoms. Bond lengths and angles represent the average value of Si and Al filled tetrahedra.

Albite ($NaAlSi_3O_8$)

Albite is the sodium endmember of the alkali and plagioclase feldspar series. The structure of albite is analogous to that of sanidine, with Na atoms replacing the K atoms found in sanidine. Low albite, the most ordered of the albite structures, was considered in this study. Albite has a perfect cleavage on {001} and a good cleavage on {010}. Common growth planes on albite include {010} and {001} (Zoltai and Stout, 1984). Therefore, the {010} and {001} albite planes were considered in this study.

The coordinatively unsaturated atoms predicted to occur on the ideal albite {010} and {001} surfaces are shown in figure 12. Predicted albite site densities on these two surfaces range from 3.8 to 11.5 sites/nm^2 (table 1). The {010} and {001} albite surfaces are likely to occur as both cleavage and growth planes. Therefore, the site densities predicted for these two planes were averaged to give albite average site densities for both crushed and uncrushed samples (tables 2 and 3).

Spectroscopic evidence.–Koretsky and others (1997) used diffuse reflectance infrared spectroscopy to study albite samples from various locales. On both synthetic and natural albite samples, a sharp band at approx 3740 cm^{-1} was assigned to non-hydrogen bonded surface >Si^{IV}OH groups. A smaller band at approx 3758 cm^{-1} was also observed on some of the samples. This band may be due to either surface >AlOH or surface >NaOH groups on albite but could not be definitively assigned to either.

Anorthite ($CaAl_2Si_2O_6$)

Anorthite is the calcic endmember of the plagioclase feldspar series. Like albite and sanidine, it is a framework silicate with Al and Si in tetrahedral coordination. Because there are equal proportions of Al and Si in anorthite, there is a strict ordering of Al and Si over the tetrahedral sites. Anorthite has a perfect cleavage on {001} and a good cleavage on {010}. Common growth planes include both the {010} and {001} planes (Zoltai and Stout, 1984). Therefore, the anorthite {010} and {001} planes were considered in this study.

The coordinatively unsaturated atoms predicted to occur on the ideal anorthite {010} and {001} surfaces are shown in figure 13. Predicted site densities for these two anorthite surfaces range from 5.7 to 11.5 sites/nm^2 (table 1). The anorthite {010} and {001} planes are both common cleavage planes and common growth planes. Therefore, the average of the predicted site densities for the {010} and {001} planes are given for either average crushed or uncrushed anorthite (tables 2 and 3).

Spectroscopic evidence.–Koretsky and others (1997) used diffuse reflectance infrared spectroscopy to study both natural and synthetic samples of anorthite. On heated anorthite powders, they observed a single, sharp band at 3740 cm^{-1}, which was attributed to isolated >Si^{IV}OH surface groups. No evidence of either >AlOH or >CaOH surface groups was found.

COMPARISON OF CALCULATED SITE DENSITIES WITH EXPERIMENTAL VALUES

Experimental determinations of surface hydroxyl site concentrations have been made using techniques including the weight loss method, the H_2O adsorption isotherm method, and the tritium exchange method. Reactive or ionizable surface site densities have been measured using techniques such as acid-base titration or by using chemical probes (James and Parks, 1982).

In the tritium exchange method, the concentration of exchangeable protons is measured and is assumed to equal the concentration of surface hydroxyl groups. It should be noted that tritium exchange results depend upon the outgassing temperature used in the experiment. For example, Yates (ms) outgassed samples under vacuum at room temperature, whereas Altmann (ms) outgassed samples under vacuum at 105°C. As might be expected, Altmann found lower densities of exchangeable protons than

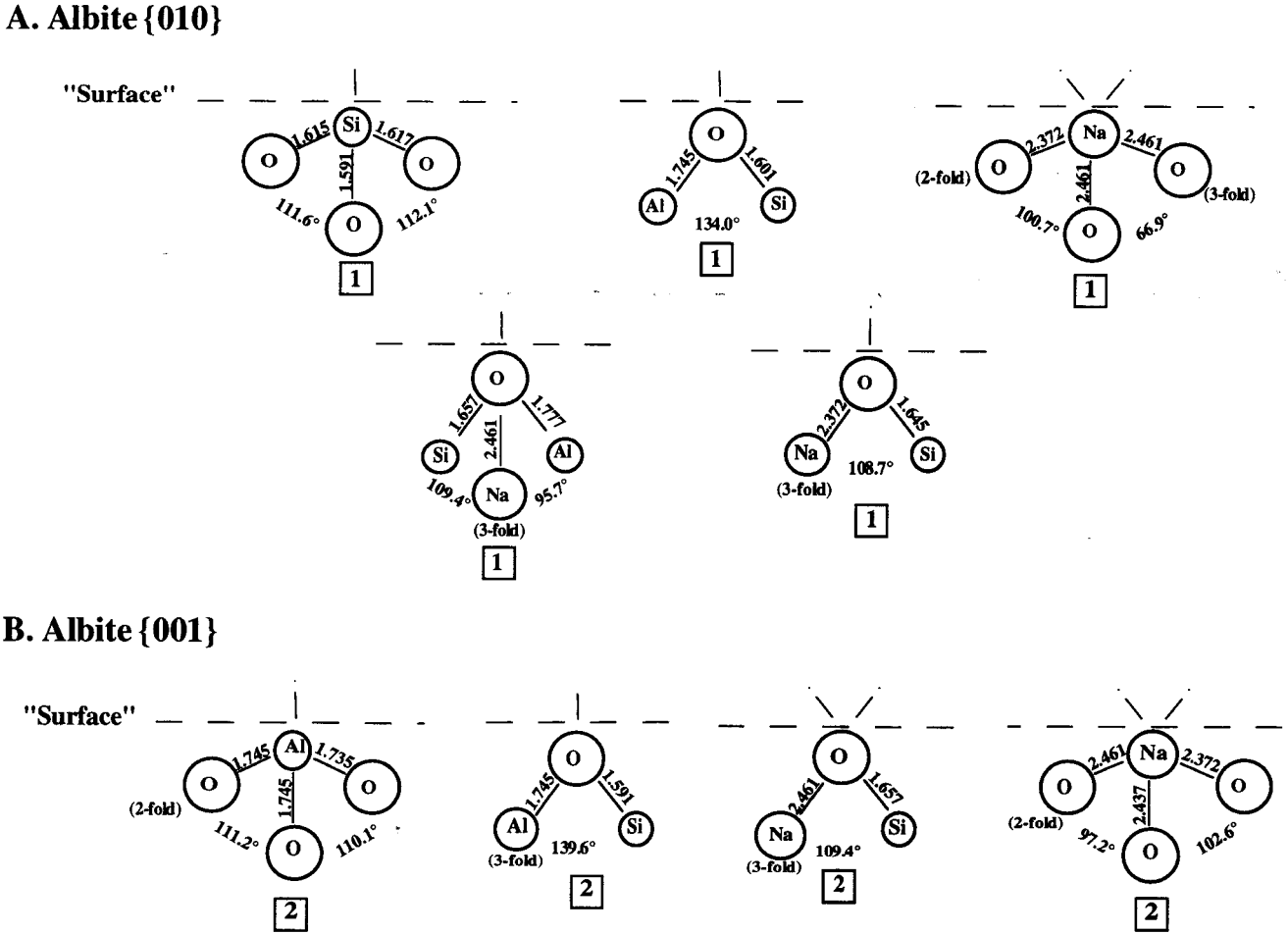

Fig. 12. Schematic depiction of the coordinatively unsaturated atoms that occur on albite. Structure of coordinatively unsaturated atoms on (A) albite {010} and (B) albite {001}.

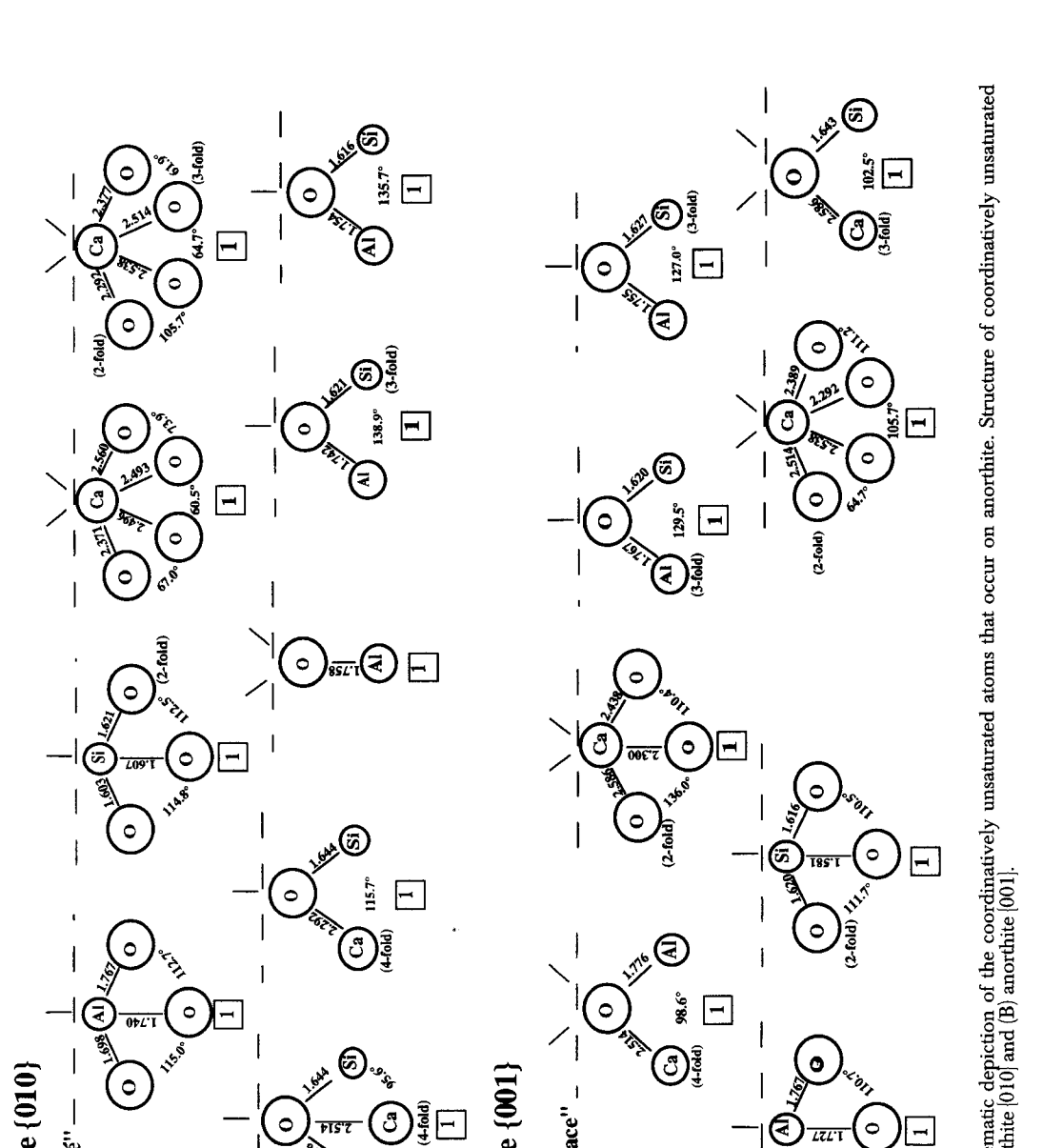

Fig. 13. Schematic depiction of the coordinatively unsaturated atoms that occur on anorthite. Structure of coordinatively unsaturated atoms on (A) anorthite {010} and (B) anorthite {001}.

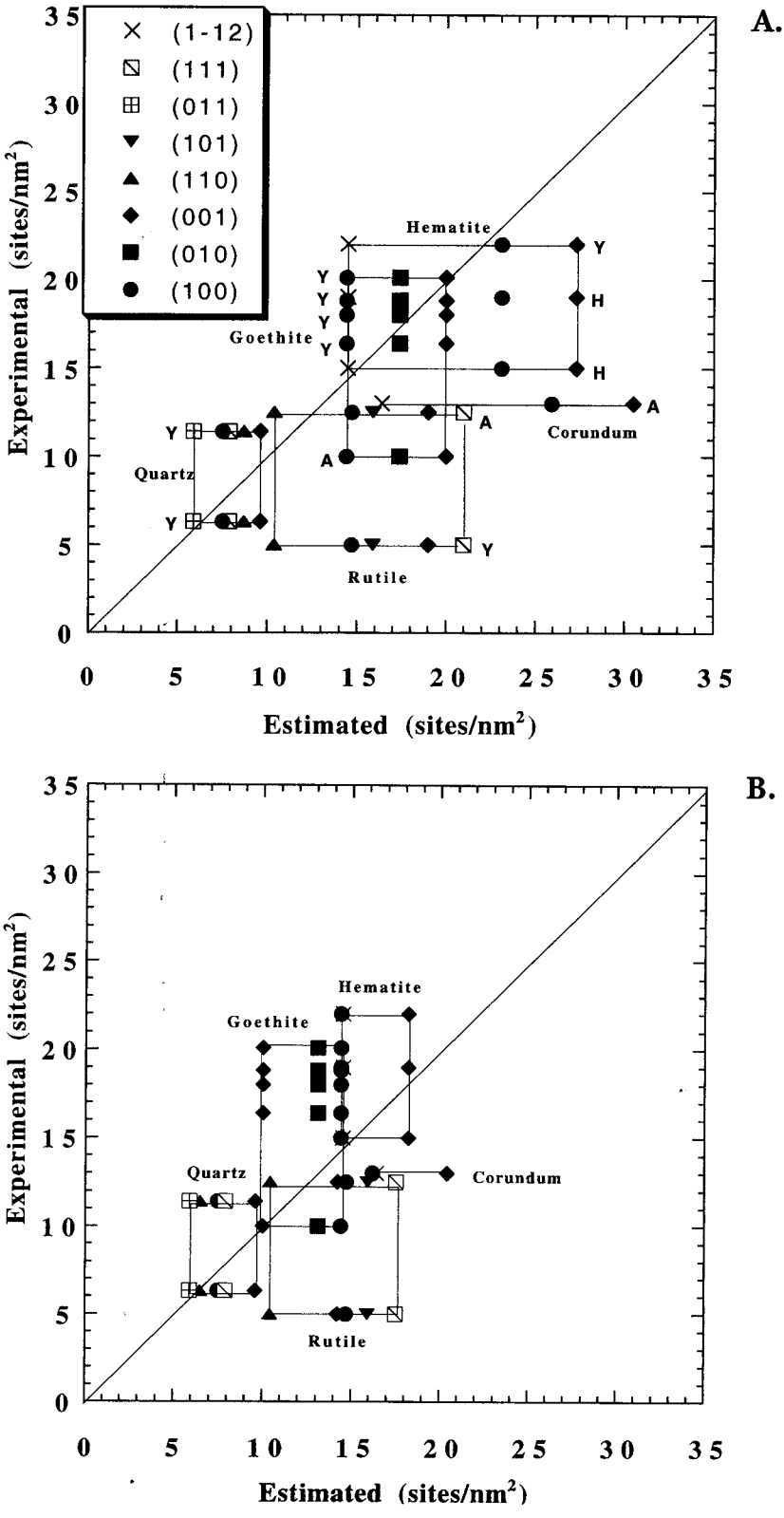

Fig. 14. Plots of experimentally determined site densities from the tritium exchange method versus estimated site densities from this study. Experimental data are given in table 5; site density estimates are given in table 1. Note that the experimental data come from three separate experimental studies: these are denoted by Y (Yates, ms), A (Altmann, ms), and H (Hsi and Langmuir, 1985). Estimated site densities are indicated by: filled circles for {100} planes, filled squares for {010} planes, filled diamonds for {001} planes, filled triangles for {110} planes, filled upside down triangles for {101} planes, open squares with a cross for {011} planes, open squares with a hatch for {111} planes and X's for (1-12) planes. The range of experimental and estimated data for each mineral is indicated by a box. Estimated site densities are from: (A) the number of broken bonds, (B) the number of coordinatively unsaturated atoms,

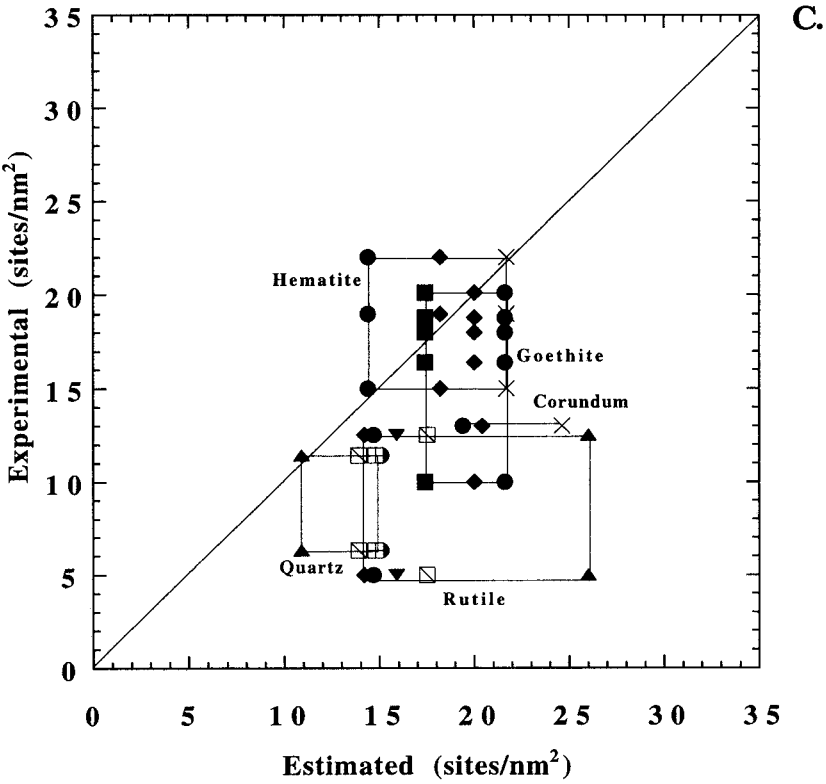

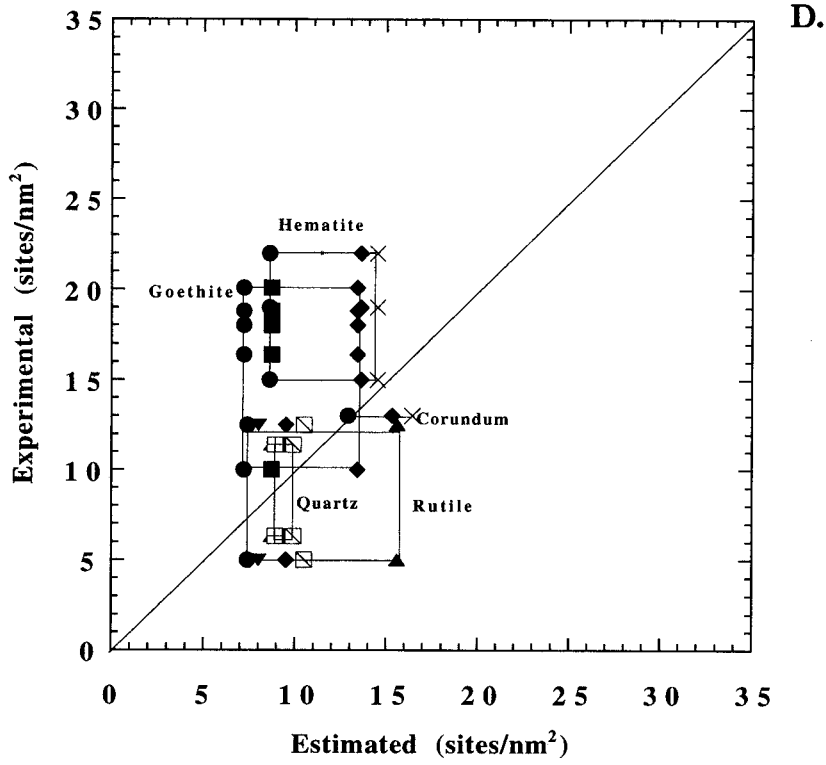

Fig. 14(C) the number of atoms within 1.4 Å of the surface, (D) the number of oxygen atoms within 1.4 Å of the surface.

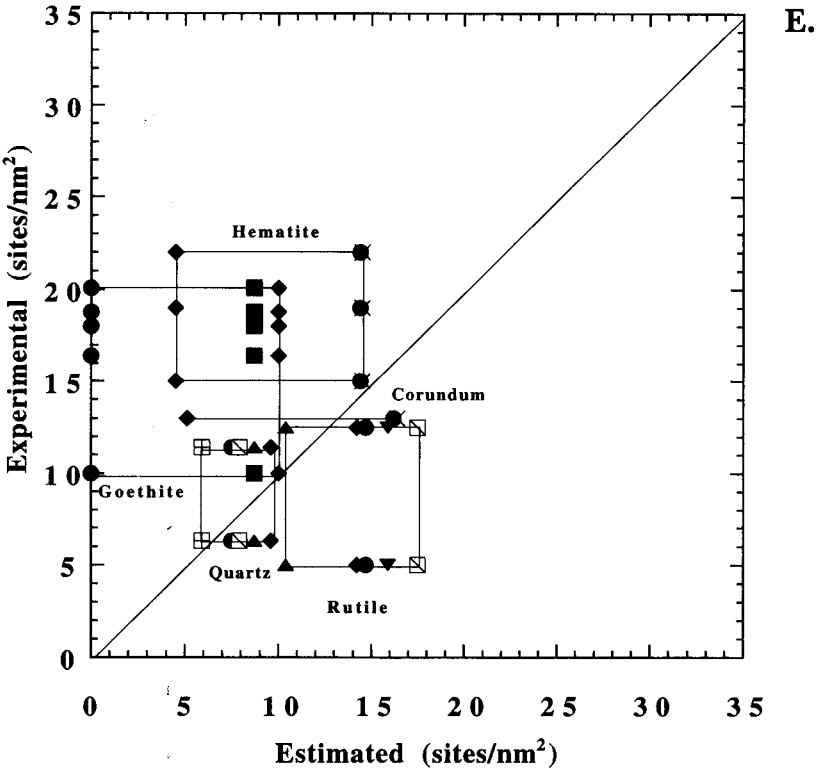

Fig. 14(E) Partial charges of the coordinatively unsaturated atoms.

Yates, by at least 6.4 sites/nm^2 and approx 7.5 sites/nm^2, respectively, for goethite and rutile.

The H_2O adsorption isotherm method has also been used to measure surface hydroxyl concentrations (Hollabaugh and Chessick, 1961; Anderson, Horlock, and Oliver, 1965; Morimoto, Nagao, and Tokuda, 1969; McCafferty and Zettlemoyer, 1971; Jones and Hockey, 1972). However, the assumptions inherent in this method make this type of site density measurement relatively inaccurate. An even simpler and probably less accurate method for calculating surface hydroxyl concentrations is the weight loss method (Yates, ms).

Ionizable or reactive surface site densities may be measured by acid-base titrations and by chemical reactions (James and Parks, 1982). In the chemical reaction method, various surface acidic and basic chemical probes are exposed to the surface. The extent of reaction of these probes with surface hydroxyl groups provides a measure of the reactive surface site density. This technique may lead to lower measured site densities than methods designed to measure all surface hydroxyl groups (for example, the tritium exchange method), if the chemical probes do not react with surface sites of very weak acid or base character, or if steric interactions prevent reaction of the probe molecules with all of the potential sites. Acid-base titrations may also give lower estimates of site densities than techniques such as the tritium exchange method because accumulation of surface charge may prevent ionization of all surface hydroxyl groups.

For the oxides and silicates considered in this study, experimentally determined site densities have been compiled (table 5) and compared to our site density estimates.

Comparison of Experimental Site Densities with Estimated Densities

Data from H_2O adsorption and weight loss methods are available for periclase, rutile, and hematite. Because results from these methods are probably quite inaccurate (Yates, ms), these data are listed in table 5 but are not plotted against the estimated site densities, nor are they used as a test of the five site density evaluation methods considered in this study. Instead, the surface site densities from tritium exchange, acid-base titration, and chemical reaction on quartz, rutile, goethite, corundum, and hematite were compared to the calculated site densities. Data for albite (Blum and Lasaga, 1991) were not included in these comparisons because of the difficulties associated with interpretation of acid-base titration of silicates (Stillings, Brantley, and Machesky, 1995).

Attempts to compare experimental data directly with our estimates are hampered by the lack of morphological data concerning samples used in most experimental studies. Crystal morphologies are rarely reported, yet different crystal morphologies imply that different crystallographic planes will be exposed at the surface. This will affect both the number and type of surface sites that exist at the surface. For this reason, the experimentally determined site densities for a given mineral are plotted against values derived for each face of that mineral in figures 14 and 15. Because a range of experimentally derived site densities exist for many of these minerals, boxes encompassing both the range of experimental site densities and the range of estimated site densities for the various faces of each mineral, are shown.

In figure 14A site densities measured in tritium exchange studies are plotted against site densities calculated in this study by setting the number of broken bonds equal to the number of sites. There is good agreement between the range of experimentally determined site densities on quartz, hematite, and goethite with our estimated site densities. Site densities calculated for rutile, and particularly for corundum, using the number of broken bonds as a proxy for the number of sites give calculated site densities somewhat higher than data from the tritium exchange studies. It should be noted that the data in figure 14 are from three separate sources (Yates, ms; Altmann, ms; Hsi and Langmuir, 1985), in which slightly different methods were used (see discussion above). The corundum and the lower set of rutile data are from the study of Altmann (ms). It is possible that our estimated site densities are higher than those from Altmann's study, because the high outgassing temperatures used in that study to remove H_2O from the mineral surfaces also desorbed some of the surface hydroxyl groups. It is also possible that calculated site densities from the number of broken bonds will tend to be too high due to steric hindrance effects that will not allow reaction with more than one or two atoms or molecules on a single coordinatively unsaturated atom. Also, in many cases, the partial charge left on a single surface group is less than $+1$ or greater than -1. Therefore, a single hydroxyl or proton, for example, may satisfy or nearly satisfy the charge on the coordinatively unsaturated surface group without achieving the original coordination. This issue is addressed in more detail in discussions of method 5 for site density evaluation (fig. 14E).

In figure 14B tritium exchange site densities are plotted against site densities calculated by setting the number of coordinatively unsaturated atoms equal to the number of sites. It can be seen in figure 14B that these calculated site densities also agree reasonably well with experimental values for quartz, goethite, hematite, and rutile. However, the calculated corundum site densities are again higher than experimental estimates from Altmann (ms). In figure 14C calculated site densities from the number of atoms within 1.4 Å are compared to densities measured using the tritium exchange method. The agreement between experimental and calculated data are somewhat poorer than in either figure 14A or B: for goethite, corundum, rutile, and quartz, calculated site densities using the number of atoms within 1.4 Å are larger than the experimentally

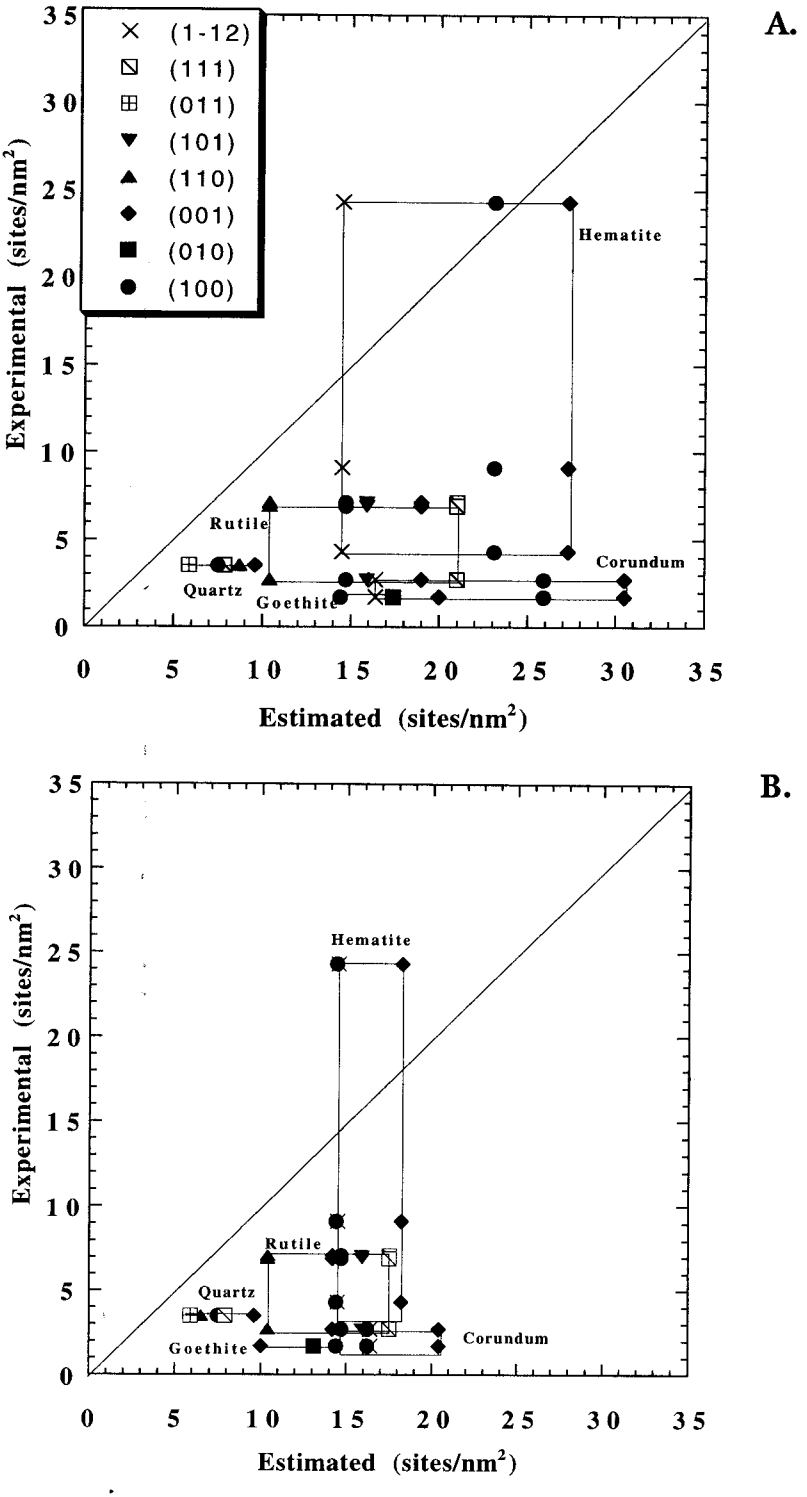

Fig. 15. Plots of experimentally determined site densities from acid-base titrations and chemical methods versus estimated site densities from this study. Experimental data are given in table 5; site density estimates are given in table 1. Estimated site densities are indicated by: filled circles for {100} planes, filled squares for {010} planes, filled diamonds for {001} planes, filled triangles for {110} planes, filled upside down triangles for {101} planes, open squares with a cross for {011} planes, open squares with a hatch for {111} planes and X's for (1-12) planes. The range of experimental and estimated data for each mineral is indicated by a box. Estimated site densities are from: (A) the number of broken bonds, (B) the number of coordinatively unsaturated atoms,

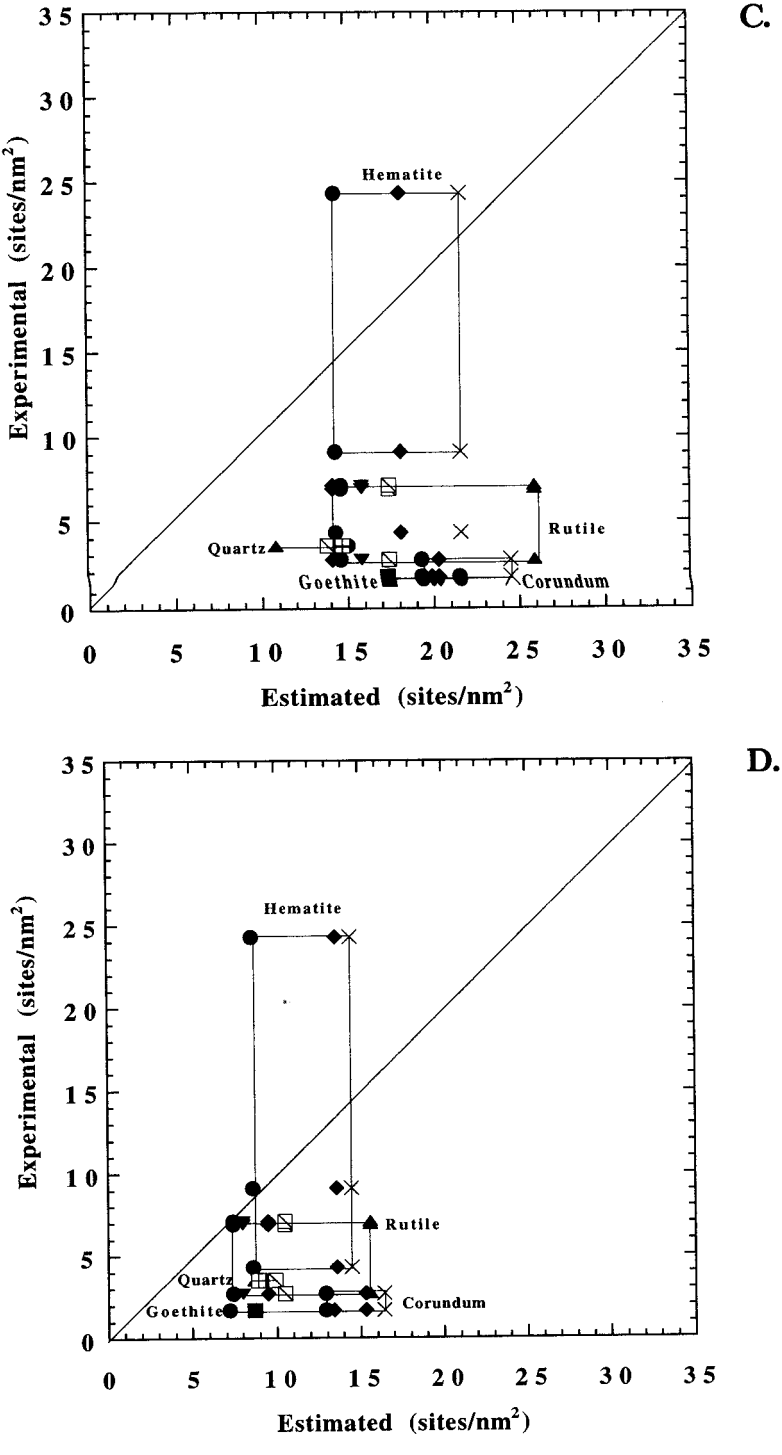

Fig. 15(C) the number of atoms within 1.4 Å of the surface, (D) the number of oxygen atoms within 1.4 Å of the surface.

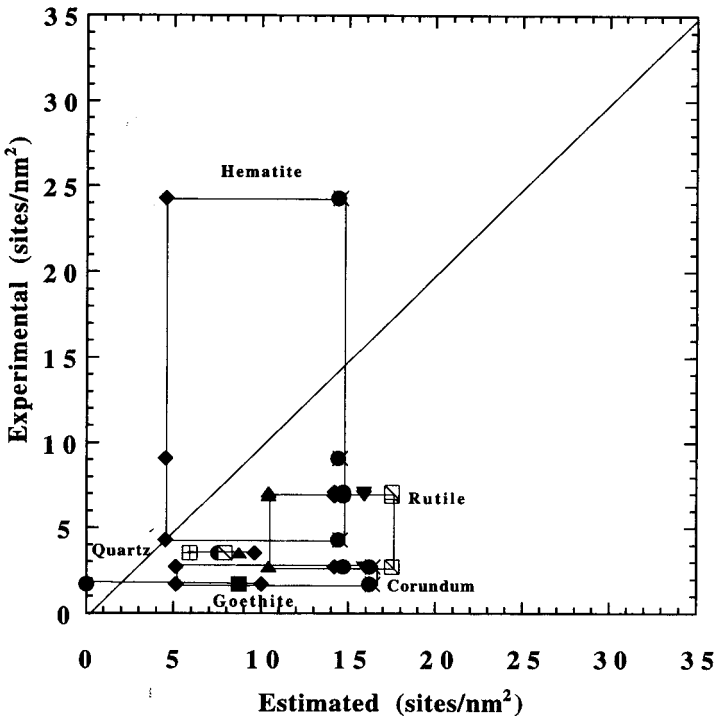

Fig. 15(E) Partial charges of the coordinatively unsaturated atoms.

derived values. It can be seen in figure 14D that calculated site densities for quartz, rutile, and corundum based on the number of O atoms within 1.4 Å depth are consistent with tritium exchange values. However, the site density estimates for goethite and especially for hematite are considerably lower than the experimentally determined site densities.

Finally, in figure 14E, site densities based on the partial charges of coordinatively unsaturated atoms at the surface are compared to the tritium exchange data. As discussed earlier (see "Method for Evaluation of Site Densities and Types" section), in this method it is assumed that coordinatively unsaturated atoms hydroxylate or protonate only if this brings the charge of the unsaturated atom closer to zero. The calculated site densities shown in this plot for quartz and corundum are in good agreement with experimental methods. Experimentally measured site densities for rutile and goethite are also consistent with this method of counting sites. However, calculated site densities for goethite and especially hematite are lower than the experimentally measured site densities.

In figure 15, estimated site densities from this study are compared to site densities measured using acid-base titration or chemical methods. It is clear from figure 15 that data derived from these methods with the exception of acid-base titration data for hematite (Huang, ms) are consistently lower than our site densities estimates. This is not unexpected, nor is it inconsistent with our site density estimates, since acid-base titrations and chemical reaction methods measure only the reactive or ionizable sites, whereas our estimation methods are meant to provide total (maximum) surface site densities. It is beyond the scope of this study to determine the proportion of our estimated sites that may be reactive with various chemical compounds or that may be ionizable in an acid-base titration for more direct comparison with the calculated data shown in figure 15.

Summary of Calculated Versus Measured Site Densities

Quantitative comparisons of our estimated site densities with experimental data are essentially impossible due to the range in experimental data for a given mineral and the lack of morphological data concerning minerals used in most experimental studies. Nonetheless, it can be seen qualitatively in figure 14 that the closest agreement between estimated site densities from this study and site densities obtained using the tritium exchange method appears to occur in figure 14A, for which estimates based on the number of broken bonds left at the mineral surface were used to obtain estimated site densities. In addition, consideration of the number of broken bonds left at the surface leads to the prediction that all kaolinite sites occur on edges rather than basal planes in agreement with experimental evidence (Sposito, 1984). This criterion is also satisfied, however, by consideration of the number of coordinatively unsaturated atoms left at the surface or by consideration of their partial charges. Surprisingly, none of the estimation methods considered in this study is clearly superior to the others.

IMPLICATIONS OF THE PRESENT STUDY

Surface Infrared Spectroscopy

Infrared spectroscopy is a valuable tool for identifying different types of surface hydroxyl groups. This is true because O-H bonds give rise to a stretching frequency in a particular region of the infrared spectrum (typically between 3200-4000 cm^{-1}), but the exact position of the IR band depends upon the underlying structure of the surface species and mineral (see for example, Little, 1966). For example, >Al-OH groups on γ-alumina are believed to give rise to distinct bands depending upon whether the aluminum atom is tetrahedrally or octahedrally coordinated (for example, Boehm and Knozinger, 1983; Koretsky and others, 1997). For this reason, the number of bands due to *non-hydrogen bonded* species in the O-H stretching region of the infrared may be indicative of the number of types of surface hydroxyl species on a given mineral.

Tsyganenko and Filimonov (1973) used considerations of crystal structure to predict the number of OH bands that will occur in the infrared spectra of various minerals. They assumed that the total number of surface hydroxyl species for a given mineral would be equal to the coordination number of oxygen in the bulk structure minus one. For example, in the anatase structure, each oxygen is bonded to four Ti atoms, so Tsyganenko and Filimonov predicted that three surface hydroxyl species should occur, giving rise to three bands in the infrared. Predicted species were labeled types I, II, III, and so on, where a type I group consists of an OH bonded to one metal atom, a type II OH is bonded to two metal atoms, a type III OH is bridged to three metal atoms, and so on.

Tsyganenko and Filimonov's predictions are not always consistent with experimental evidence. Their theory did correctly predict the occurrence of one band on quartz and three bands on γ-alumina. However, they were to forced to assume that the type (II) groups on anatase and rutile give rise to two separate bands and that type (II) groups do not occur on BeO, ZnO, ThO_2, CeO_2, HfO_2, and ZrO_2. In addition, spectra of MgO, ZnO, and NiO could only be explained by making ad hoc assumptions concerning the occurrence of particular surface planes on the samples used to obtain the spectra together with ad hoc assumptions concerning the distribution of different site types on different surface planes.

Tsyganenko and Filimonov also did not consider the occurrence of surface hydroxyl species on metal atoms with less than their bulk coordination number. In addition, they did not explore the question of which plane actually occurs out of the set of possibilities in each direction. Both these problems may have contributed to the disagreement between experimentally observed numbers of O-H bands and their predicted values.

However, there are also many difficulties associated with the interpretation of bands in the infrared O-H stretching region (for example, Little, 1966). It is often difficult to distinguish between isolated, vicinal hydrogen bonded, and geminal groups using infrared spectroscopy. (Vicinal groups are surface hydroxyl species on the mineral surface that are close enough to hydrogen bond to each other. Geminal groups occur when two hydroxyl groups are strongly bound or chemisorbed to a single cation but may

TABLE 6

Summary of the "principal" site types expected for mineral surfaces, assuming that coordinatively unsaturated atoms protonate or hydroxylate until they regain their bulk coordination number.

Mineral	Plane	Types	Total
α-Quartz (SiO_2)	{100}	$>Si^{IV}\text{-}O^{II}\text{-}H$	1
	{001}	$>Si^{IV}\text{-}(O^{II}\text{-}H)_2$	1
	{110}	$>Si^{IV}\text{-}O^{II}\text{-}H$, $>Si^{IV}\text{-}(O^{II}\text{-}H)_2$	2
	{011}	$>Si^{IV}\text{-}O^{II}\text{-}H$	1
	{111}	$>Si^{IV}\text{-}O^{II}\text{-}H$, $>Si^{IV}\text{-}(O^{II}\text{-}H)_2$	2
	Total		2
Periclase (MgO)	{100}	$>Mg^{VI}\text{-}O^{II}\text{-}H$, $>Mg_6\text{-}O^{VI}\text{-}H$	2
	{111}, pos	$>Mg^{VI}\text{-}(O^{II}H)_3$	1
	{111}, neg	$>Mg_3\text{-}O^{VI}\text{-}H_3$	1
	{110}	$>Mg^{VI}\text{-}(O^{II}H)_2$, $>Mg_4\text{-}O^{VI}\text{-}H_2$	2
	Total		6
Rutile (TiO_2)	{100}	$>Ti^{VI}\text{-}O^{II}\text{-}H$, $>Ti_2\text{-}O^{III}\text{-}H$	2
	{001}	$>Ti^{VI}\text{-}(O^{II}\text{-}H)_2$, $>Ti_2\text{-}O^{III}\text{-}H$	2
	{110}	$>Ti^{VI}\text{-}O^{II}\text{-}H$, $>Ti_2\text{-}O^{III}\text{-}H$	2
	{101}	$>Ti^{VI}\text{-}O^{II}\text{-}H$, $>Ti_2\text{-}O^{III}\text{-}H$	2
	{111}	$>Ti^{VI}\text{-}(O^{II}\text{-}H)_2$, $>Ti_2\text{-}O^{III}\text{-}H$, $>Ti^{VI}\text{-}O^{II}\text{-}H$	3
	Total		3
Goethite (α-FeOOH)	{100}	$>Fe^{VI}\text{-}O^{II}\text{-}H$, $>Fe_2\text{-}O^{IV}\text{-}H_2$	2
	{010}	$>Fe^{VI}\text{-}(O^{II}\text{-}H)_2$, $>Fe_2\text{-}O^{III}\text{-}H$, $>Fe_2\text{-}O^{IV}\text{-}H_2$	3
	{001}	$>Fe^{VI}\text{-}[(O^{II}\text{-}H)_3][(O^{IV}\text{-}H_3)]$, $>Fe_2\text{-}O^{III}\text{-}H$	2
	Total		5
Corundum (α-Al_2O_3)	{100}	$>Al^{VI}\text{-}(O^{II}\text{-}H)_2$, $>Al_2\text{-}O^{IV}\text{-}H_2$, $>Al_3\text{-}O^{IV}\text{-}H$	3
	{001}	$>Al_3\text{-}O^{IV}\text{-}H$, $>Al^{VI}\text{-}(O^{II}\text{-}H)_3$	2
	{1-12}	$>Al_3\text{-}O^{IV}\text{-}H$, $>Al^{VI}\text{-}O^{II}\text{-}H$	2
	Total		5

TABLE 6
(continued)

Mineral	Plane	Types	Total
Hematite (α - Fe_2O_3)	{100}	$>Fe^{VI}\text{-}(O^{II}\text{-}H)_2$, $>Fe_3\text{-}O^{IV}\text{-}H$, $>Fe_2\text{-}O^{IV}\text{-}H_2$	3
	{001}	$>Fe^{VI}\text{-}(O^{II}\text{-}H)_3$, $>Fe_3\text{-}O^{IV}\text{-}H$	2
	{1-12}	$>Fe_3\text{-}O^{IV}\text{-}H$, $>Fe^{VI}\text{-}O^{II}\text{-}H$	2
	Total		5
Andalusite (Al_2SiO_5)	{100}	$>Al^{V}\text{-}O^{II}\text{-}H_2$, $>Al_2\text{-}O^{III}\text{-}H$, $>Si^{IV}\text{-}(O^{II}\text{-}H)_3$	3
	{010}	$>Si^{IV}\text{-}(O^{II}\text{-}H)_2$, $>Al^{V}\text{-}(O^{II}\text{-}H)_3$, $>Al_2\text{-}O^{III}\text{-}H$	3
	{001}	$>Al^{V}\text{-}O^{II}\text{-}H$, $>Al^{IV}\text{-}(O^{II}\text{-}H)_2$, $>Si^{IV}\text{-}O^{II}\text{-}H$, $>[(Si)(Al)]\text{-}O^{III}\text{-}H$	4
	{011}	$>Al^{IV}\text{-}O^{II}\text{-}H$, $>Al^{V}\text{-}O^{II}\text{-}H$, $>Al_2\text{-}O^{III}\text{-}H$, $>Si^{IV}\text{-}O^{II}\text{-}H$	4
	Total		10
Sillimanite (Al_2SiO_5)	{100}	$>Si^{IV}\text{-}O^{II}\text{-}H$, $>Al^{IV}\text{-}O^{II}\text{-}H$, $>(Al^{VI})_2\text{-}O^{III}\text{-}H$	3
	{010}	$>Si^{IV}\text{-}(O^{II}\text{-}H)_2$, $>Al^{IV}\text{-}O^{III}\text{-}H_2$, $>Al^{VI}\text{-}(O^{II}\text{-}H)$	3
	{001}, pos	$>Si^{IV}\text{-}O^{II}\text{-}H$, $>Al^{IV}\text{-}O^{II}\text{-}H$, $>(Al^{VI})_2\text{-}O^{III}\text{-}H$, $>[(Al^{VI})(Si)]\text{-}O^{III}\text{-}H$,	4
	{001}, neg	$>Al^{VI}\text{-}(O^{II}\text{-}H)_2$, $>[(Si)(Al^{VI})]\text{-}O^{III}\text{-}H$, $>[(Al^{IV})(Al^{VI})]\text{-}O^{III}\text{-}H$	3
	{110}	$>(Al^{VI})_2\text{-}O^{III}\text{-}H$, $>Si^{IV}\text{-}O^{II}\text{-}H$, $>Si^{IV}\text{-}(O^{II}\text{-}H)_2$, $>Al^{IV}\text{-}O^{II}\text{-}H$, $>Al^{IV}\text{-}(O^{II}\text{-}H)_2$	5
	Total		13
Kaolinite ($Al_2Si_2O_5(OH)_4$)	(010)	$>Al^{VI}\text{-}(O^{II}\text{-}H)_4$, $>Si^{IV}\text{-}O^{II}\text{-}H$	2
	(0-10)	$>Si^{IV}\text{-}(O^{II}\text{-}H)_2$, $>Al^{VI}\text{-}O^{III}\text{-}H_2$, $>[(Al^{VI})(Si^{IV})]\text{-}O^{III}\text{-}H$	3
	(110)	$>Al^{VI}\text{-}(O^{II}\text{-}H)_2$, $>Si^{IV}\text{-}O^{II}\text{-}H$	2
	(-1-10)	$>Si^{IV}\text{-}O^{II}\text{-}H$, $>Al^{VI}\text{-}O^{III}\text{-}H_2$ $>[(Si^{IV})(Al^{VI})]\text{-}O^{III}\text{-}H$	3
	Total		6

TABLE 6
(continued)

Mineral	Plane	Types	Total
Sanidine ($KAlSi_3O_8$)	{010}	>Si^{IV}-O^{II}-H, >Al^{IV}-O^{II}-H, >(K)(Si)-O^{III}-H, >(K)(Al)-O^{III}-H	4
	{001}	>Si^{IV}-O^{II}-H, >Al^{IV}-O^{II}-H, >(K)(Si)-O^{III}-H, >(K)(Al)-O^{III}-H	4
	Total		4
Albite ($NaAlSi_3O_8$)	{010}	>Si^{IV}-O^{II}-H, >Na^{V}-(O^{II}-H)$_2$, >[(Al)(Si)]-O^{III}-H, >[(Na)(Si)]-O^{III}-H. >[(Na)(Si)(Al)]-O^{IV}-H	5
	{001}	>Al^{IV}-O^{II}-H, >[(Al)(Si)]-O^{III}-H, >[(Na)(Si)]-O^{IV}-H_2, >Na^{V}-(O^{II}-H)$_2$	4
	Total		8
Anorthite ($CaAl_2Si_2O_6$)	{010}	>Al^{IV}-O^{II}-H, >Si^{IV}-O^{II}-H, >Ca^{VI}-(O^{II}-H)$_2$, >[(Al)(Si)(Ca)]-O^{IV}-H, >[(Si)(Ca)]-O^{III}-H, >Al^{IV}-(O^{II}-H)$_2$, >[(Al)(Si)]-O^{III}-H	7
	{001}	>Si^{IV}-O^{II}-H, >[(Al)(Si)]-O^{III}-H, >Al^{IV}-O^{II}-H, >[(Ca)(Al)]-O^{IV}-H, >[(Ca)(Si)]-O^{III}-H, >Ca^{V}-(O^{II}-H)$_2$, >Ca^{VI}-(O^{II}-H)$_2$	7
	Total		10

also be hydrogen bonded to each other.) In addition, many nominally anhydrous minerals incorporate OH into their bulk structures (for example, Aines and Rossman, 1984). These bulk OH groups may produce bands that obscure part of the infrared spectra. Weakly bound or physisorbed H_2O can also give rise to strong bands in the infrared. The O-H stretching bands of some surface species may occur at nearly the same frequency, while other species may not give sufficiently intense bands to be easily observed. Finally, infrared spectroscopy is generally done on powdered samples, where the relative abundances of various surface planes are often completely unknown.

For all these reasons, it is extremely difficult to make simple predictions concerning the number or position of O-H stretching bands that will occur in the infrared spectrum of a given mineral. Nonetheless, detailed considerations of crystal structure and the occurrence of various surface species on different planes of a mineral can be quite valuable in the interpretation of infrared spectra. In fact, without such considerations, it is nearly impossible to make even the most qualitative interpretation of surface infrared spectra. In addition, qualitative predictions of the types of surface hydroxyl species expected to occur on a mineral surface can serve as the basis for quantitative calculations

of O-H stretching band frequencies and intensities. For example, Kubicki, Blake, and Apitz (1996) used molecular orbital calculations to make quantitative predictions of the infrared frequency and intensity of the O-H stretching bands due to surface $>Al^{IV}\text{-}O^{II}\text{-}H$ and $>Si^{IV}\text{-}O^{II}\text{-}H$ groups on aluminosilicates.

As a basis for calculations such as these and to aid in the qualitative interpretation of infrared spectra, a list of "principal" species was selected by making several assumptions (table 6). First, it was assumed that two or more species on a mineral surface that differed only with respect to bond angles and lengths could be treated as a single "principal" species. For example, on sillimanite (110) two $>Al_2OH$ groups occur which differ with respect to their Al-O-Al angles, as well as in the length of the Al-O bonds. These are shown as two separate species in figure 9E but were treated as a single species in table 6. Next, it was assumed that surface groups that differ with respect to the second nearest neighbors of the metal atoms could also be treated as a single "principal" species. For instance, on corundum (100), there are four 4-fold Al atoms in Al^{VI} sites. Two of these Al atoms are bonded to two coordinatively saturated O atoms and to two 3-fold coordinatively unsaturated O atoms. The other two Al atoms are bonded to two coordinatively saturated O atoms, one 2-fold coordinatively unsaturated O atom, and one 3-fold coordinatively unsaturated O atom. However, all four of these Al atoms were assumed to give rise to a single "principal" $>O_4\text{-}Al\text{-}(OH)_2$ species. This assumption was made in all cases *except* when a first nearest neighbor oxygen was bonded only to the metal of the surface species, such that it could form another hydroxyl moiety. For example, one of the two 3-fold coordinated Si atoms at the surface of quartz (111) is bonded to two coordinatively saturated O atoms and to one 1-fold coordinatively unsaturated atom. If this 1-fold coordinatively unsaturated O protonates, an $>Si(OH)_2$ group forms, clearly distinct from the >SiOH group that forms on the 3-fold coordinated Si atom that is bonded to three coordinatively saturated O atoms. Finally, it has been tacitly assumed in all the above examples and for the species given in table 6 that surface hydroxyl groups form on coordinatively unsaturated atoms such that they regain their bulk coordination numbers (that is, using assumptions of the first method for estimating site densities). If a different set of assumptions concerning hydroxylation and protonation is chosen, such as assuming that coordinatively unsaturated atoms protonate or hydroxylate only when this brings their charge closer to zero, a different set of "principal" surface species would result.

The surface hydroxyl species listed in table 6 should be regarded as one set of possibilities that incorporate several simplifications and assumptions. Many of these species have been discussed above (see "Spectroscopic Evidence" subsections in "Results" section) and have been shown to be consistent with observed infrared spectra. In particular, periclase, rutile, goethite, and corundum infrared spectra could be interpreted using the species given in table 6. These species should serve as a valuable guide in the interpretation of infrared spectra, and they should be a useful starting point for quantitative investigations of the O-H stretching frequencies and intensities of surface hydroxyl species, particularly if surface infrared studies of single crystal surfaces become available.

Adsorption and Kinetic Models

It must be emphasized that the surface sites described in this study are from consideration of *idealized* mineral surfaces, such as might be observed in vacuum or in air. In contact with mineral solutions, these surfaces may react with H_2O, H^+, OH^-, and other cations and anions in the solution to produce surfaces with very different surface configurations. Nonetheless, site densities and types observed from spectroscopy of samples in contact with air or solution and theoretical estimates based on very simplistic considerations of mineral structures are routinely used in models of adsorption or

dissolution (James and Parks, 1982; Davis and Kent, 1990; Dzombak and Morel, 1990). In future work, such models of surface sites, including those described in this study, should be modified for use in adsorption or dissolution studies, if possible, to reflect the equilibration of the mineral surface with the solution (for example, Rustad, Hay, and Felmy, 1996a,b). In the present study, however, only the unreacted idealized surfaces are considered.

The quantitative effect of variations in site density values on surface complexation models has been examined in the sensitivity analysis of Hayes and others (1991). Hayes and others (1991) fitted data from potentiometric titrations of rutile, goethite, and corundum to obtain log K values for reactions such as

$$>SOH + H^+ = >SOH_2^+ \tag{3}$$

and

$$>SOH = >SO^- + H^+ \tag{4}$$

Therefore, (using the notation of Hayes and others, 1991),

$$K^+ = \{[>SOH_2^+]/[>SOH][H^+]\} \cdot \exp(F\psi_0/RT) \tag{5}$$

and

$$K^- = \{[SO^-][H^+]/[SOH]\} \cdot \exp(-F\psi_0/RT) \tag{6}$$

where $[>SOH_2^+]$, [>SOH], and $[>SO^-]$ represent the concentrations of protonated, neutral, and deprotonated surface groups, respectively, F is Faraday's constant, ψ_0 represents the surface potential, R is the gas constant, and T is temperature. For the diffuse-layer model, the constant capacitance model, and the triple layer model, Hayes and others (1991) found that a change from 1 to 10 sites/nm^2 or from 10 to 100 sites/nm^2 resulted in changes in fitted K^+ and K^- values of at least one order of magnitude, and in some cases as much as two orders of magnitude.

This sensitivity of fitted K^+ and K^- values to the total site density may complicate comparison of K^+ and K^- values for the same mineral obtained by experiments using different samples of the mineral. For example, it can be seen in table 1 that using the partial charge of coordinatively unsaturated atoms to evaluate site densities gives a site density of 0 sites/nm^2 on goethite (100) and a density of 10.0 sites/nm^2 on goethite (001). If two potentiometric titrations were done, one on a goethite samples with a high abundance of (100) faces and the other on a goethite sample with a high abundance of (001) faces, fitted log K^+ and log K^- values might differ by a full log unit. Thus, setting all site densities equal to a single constant may confound interpretation of experimentally determined values of log K^+ and log K^-.

Recently, there have been attempts to develop multi-site models of adsorption. Among the most notable of these models is the MUSIC model (Hiemstra, Riemsdijk, and Bolt, 1989; Hiemstra, Wit, and Riemsdijk, 1989), in which singly, doubly, and triply coordinated hydroxyl groups are considered. However, as in many other studies, no account is taken for the formation of groups on coordinatively unsaturated metal atoms at the surface. The various surface species suggested in this study might serve as the basis for a multi-site model similar to the MUSIC model.

Site densities are also important in oxide and silicate dissolution rate models analogous to the model developed by Furrer and Stumm (1986). In their model, Furrer and Stumm (1986) suggested that for surface-controlled dissolution reactions, the rate of

reaction must depend on the concentration of surface species. They proposed a rate law of the form,

$$R = k \cdot [C_H^S]^n + k^{L-}[C_L^S], \quad (7)$$

where R is the dissolution rate, k is the apparent rate coefficient for proton-promoted dissolution, k^{L-} is the apparent rate coefficient for ligand-promoted dissolution, C_H^S is the concentration of protonated surface species, C_L^S is the concentration of surface sites with sorbed ligand, and n is an integer if only one dissolution mechanism is involved at the protonated surface site.

Furrer and Stumm (1986) successfully modeled BeO and δ-Al_2O_3 dissolution rates using eq (7). Rate models of the same form have since been extended successfully to model other oxide and silicate mineral dissolution rates. For example, Amrhein and Suarez (1988) modeled anorthite dissolution using the rate law

$$R = k_H \cdot [>SOH_2^+]^4 + k_L \cdot [>S - L] + k_0 \cdot [>SOH], \quad (8)$$

where R is the dissolution rate, k_H, k_L, and k_0 are the apparent rate coefficients for proton-promoted dissolution, ligand-promoted dissolution, and dissolution when there is no net sorption of protons or hydroxide ions; brackets indicate concentrations of the various surface species. Wieland and Stumm (1992) were able to model kaolinite dissolution using a rate law that depended on the concentrations of >AlOH surface groups on edge and gibbsite-type surfaces and on the concentration of $>SiO^-$ surface groups. Brady and Walther (1989) interpreted quartz dissolution, and Casey, Hochella, and Westrich (1993) interpreted tephroite dissolution using rate laws with dependence on the concentrations of protonated and deprotonated surface species. Quartz dissolution in NaCl solutions was also modeled by Dove and Elston (1992) using the rate law

$$R = k^0 \cdot [X_{>SiOH}] + k^{sum} \cdot [X_{>sum}] + k^{sum} \cdot [X_{>sum}]^2, \quad (9)$$

where R is the dissolution rate, k^0 and k^{sum} are apparent rate coefficients, $X_{>SiOH}$ is the mole fraction of neutral >SiOH surface species, and $X_{>sum}$ is the sum of the mole fractions of the $>SO^-$ and $>SO^- Na^+$ surface species. Sverjensky and others (1995) suggested that silicate dissolution rates in general might be modeled using the expression,

$$R = k^+[>SOH_2^+]^{n+} + k^0[>SOH]^{n0} + k^-[>SO^-]^{n-} \quad (10)$$

where R is the dissolution rate, $[>SOH_2^+]$ is the concentration of protonated surface hydroxyl groups, [>SOH] is the concentration of >SOH groups at the surface, $[>SO^-]$ is the concentration of deprotonated surface hydroxyl groups, k^+, k^-, and k^0 are apparent rate coefficients, and n^+, n^-, and n^0 are empirical reaction orders.

In expressions such as eq (10) relative concentrations of surface species with adsorbed proton or ligand at a given temperature, pressure, and fluid composition are generally evaluated using surface complexation models with equilibrium surface stability constants. However, as discussed above, these equilibrium constants depend on assumed site density values. Therefore, the site densities used in the surface complexation models may influence the success of applying these types of rate models. In addition, if values of k^+, k^-, and k^0 are obtained by fitting rate data, then these values will also depend on the assumed total site density used in the surface complexation models.

CONCLUSIONS

The concentrations and types of surface sites that occur on rock-forming minerals are of significance in the quantitative interpretation of a variety of geological processes.

Estimates of far from equilibrium dissolution rates for many silicates include terms to account for the speciation of chemically bound hydrogen at the silicate surface. Estimates of surface site concentrations on silicate minerals are therefore of use in the quantitative interpretation of dissolution rates. In addition, adsorption at mineral surfaces is influenced by site densities and distributions. In spite of the crucial role that surface site densities play in both adsorption and dissolution processes, there are few estimates or measurements of site densities on commonly occurring minerals.

Because of this paucity of site density data, the concentrations of various types of surface hydroxyl groups have been predicted for commonly occurring cleavage and growth planes of twelve rock-forming minerals, chosen to represent a range of structures and compositions. Five separate methods for calculating site densities on charge-neutral or nearly charge-neutral cleavage or growth surfaces with a minimum strength of broken bonds were assessed. The five methods of calculating site densities from these predicted surfaces were: (1) equating the number of broken bonds on a given surface to the number of sites, (2) equating the number of coordinatively unsaturated atoms with the site density, (3) setting the site density equal to the number of atoms within 1.4 Å of the surface (regardless of coordinative saturation state), (4) setting the site density equal to the number of oxygen atoms within 1.4 Å of the surface, and (5) calculating the site density from the charge of coordinatively unsaturated surface atoms.

Comparing estimates of surface site densities with experimentally derived values is often hampered by a lack of crystal morphological data. Estimates are derived for individual planes on each mineral, whereas experimental measurements are usually made on crystals or powders with an unknown distribution of surface planes. The distribution of planes can drastically affect measured or estimated site densities, yet most experimental studies do not include any data pertaining to the crystal morphologies of the samples used to determine surface site concentrations. Using the five separate methods, site densities were calculated for common cleavage and growth planes and were found to range from zero to approx 40 sites/nm^2. Calculated site densities for various mineral faces were compared to the available experimental data. The best agreement with tritium exchange data was obtained by setting the number of sites equal to the number of broken bonds at the surface. The predicted site densities on commonly occurring cleavage or growth planes were also averaged to give a single "cleavage" or "growth" face site density for each mineral.

The distribution of different types of surface hydroxyl sites on the cleavage and growth planes was also predicted in this study. Although quantitative comparison of site type distributions on oxide and silicate minerals with infrared data is not possible, qualitative comparison is. Infrared spectroscopic evidence for quartz, periclase, rutile, corundum, hematite, albite, anorthite, and sanidine site distributions is at least qualitatively consistent with the predictions made in this study. Predicted site types should aid in the interpretation of infrared spectroscopic data. In addition, the estimates not only of site densities but also of site types should be extremely useful in the future development of multi-site models of adsorption, as well as in quantifying mineral dissolution kinetics.

ACKNOWLEDGMENTS

A review of an early version of this manuscript by David Veblen is greatly appreciated. This research was also significantly improved by conversations with David Noe, David Elbert, Louise Criscenti, Julia King, and Johnson Haas. The authors very much appreciate thorough reviews by J. Kubicki, M. Schlegel, L. Charlet, and one anonymous reviewer. This research was supported by NSF Grant EAR 9526623 to D.A.S., DOE Grant DE-FG02-96ER-14616 to D.A.S. and by the Morton K. Blaustein Department of Earth and Planetary Sciences Eugster Summer Research Fund to C.M.K.

APPENDIX

APS: Sum of the absolute values of the Pauling bond strengths for each broken bond in this unit cell.
ABS: Sum of the absolute values of the Brown bond strengths for each broken bond in this unit cell.
TBS: Sum of the Brown bond strengths for each broken bond in this unit cell, where broken cation bonds are given positive values and broken anion bonds are given negative values.
Method 1: Each broken bond counted as one site
Method 2: Each coordinatively unsaturated atom counted as one site
Method 3: Each atom, regardless of coordinative saturation state, within 1.4 Å of mineral surface, counted as one site.
Method 4: Each oxygen atom, regardless of coordinative saturation state, within 1.4 Å of mineral surface, counted as one site.
Method 5: Each cation with a charge of +0.5 to +1.0 counted as one site; each cation with a charge of +1.5 to + 2.0 counted as two sites. Each anion with a charge of -0.5 to -1.0 counted as one site; each anion with a charge of -1.5 to -2.0 counted as two sites.

α-Quartz (100)

Site	Coordination	Depth (Å)	Broken Bond Type	Length Broken Bond	Brown Strength Broken Bonds
Si^{IV}	4	3.118	-	-	-
Si^{IV}	4	1.120		-	-
Si^{IV}	3	0.862	Si^{IV}-O^{II}	1.605	1.052
O^{II}	2	3.740		-	-
O^{II}	1	0	Si^{IV}-O^{II}	1.605	-1.052
O^{II}	2	2.497		-	-
O^{II}	2	0.622		-	-
O^{II}	2	1.981		-	-
O^{II}	2	1.360		-	-
#broken bonds:	$7.5/nm^2$		APS	$7.5/nm^2$	
#unsaturated atoms:	$7.5/nm^2$		ABS	$7.9/nm^2$	
#atoms within 1.4 Å depth	$18.8/nm^2$		TBS	0	
#O atoms within 1.4 Å depth	$11.3/nm^2$		Area unit cell:	0.2656 nm^2	
# sites from partial charges	$7.5/nm^2$				

α-Quartz (001)

Site	Coordination	Depth (Å)	Broken Bond Type	Length Broken Bond	Brown Strength Broken Bonds
Si^{IV}	3	0.642	Si^{IV}-O^{II}	1.613	1.029
Si^{IV}	4	4.245	-	-	-
Si^{IV}	4	2.443	-	-	-
O^{II}	2	4.887	-	-	-
O^{II}	2	1.284	-	-	-
O^{II}	2	3.603	-	-	-

APPENDIX

(continued)

α-Quartz (001)

O^{II}	2	3.085	-	-	-
O^{II}	1	0	Si^{IV}-O^{II}	1.613	-1.029
O^{II}	2	1.801	-	-	-
#broken bonds:	9.6/nm^2		APS	9.6/nm^2	
#unsaturated atoms:	9.6/nm^2		ABS	9.8/nm^2	
#atoms within 1.4 Å depth	14.3/nm^2		TBS	0	
#O atoms within 1.4 Å depth	9.6/nm^2		Area unit cell:	0.2091 nm^2	
# sites from partial charge	9.6/nm^2				

α-Quartz (110)

Site	Coordination	Depth (Å)	Broken Bond Type	Length Broken Bond	Brown Strength Broken Bonds
Si^{IV}	4	1.452	-	-	-
Si^{IV}	2	0.447	Si^{IV}-O^{II}, Si^{IV}-O^{II}	1.613, 1.613	1.029, 1.029
Si^{IV}	4	1.452	-	-	-
O^{II}	2	1.970	-	-	-
O^{II}	1	0	Si^{IV}-O^{II}	1.613	-1.029
O^{II}	2	1.380	-	-	-
O^{II}	2	1.380	-	-	-
O^{II}	1	0	Si^{IV}-O^{II}	1.613	-1.029
O^{II}	2	1.970	-	-	-
#broken bonds:	8.7/nm^2		APS	8.7/nm^2	
#unsaturated atoms:	6.5/nm^2		ABS	8.9/nm^2	
#atoms within 1.4 Å depth:	10.9/nm^2		TBS	0	
#O atoms within 1.4 Å depth:	8.7/nm^2		Area unit cell:	0.4600 nm^2	
# sites from partial charges	8.7/nm^2				

α-Quartz (011)

Site	Coordination	Depth (Å)	Broken Bond Type	Length Broken Bond	Brown Strength Broken Bonds
Si^{IV}	4	1.746	-	-	-
Si^{IV}	3	0.834	Si^{IV}-O^{II}	1.613	1.029
Si^{IV}	4	1.290	-	-	-
O^{II}	2	1.061	-	-	-
O^{II}	1	0	Si^{IV}-O^{II}	1.613	-1.029
O^{II}	2	1.160	-	-	-
O^{II}	2	1.420	-	-	-

APPENDIX

(continued)

α-Quartz (011)

O^{II}	2	1.519	-	-	-
O^{II}	2	2.581	-	-	-
#broken bonds:	5.9/nm^2		APS	5.9/nm^2	
#unsaturated atoms:	5.9/nm^2		ABS	6.1/nm^2	
#atoms within 1.4 Å depth:	14.8/nm^2		TBS	0	
#O atoms within 1.4 Å depth:	8.9/nm^2		Area unit cell:	0.3380 nm^2	
# sites from partial charges	5.9/nm^2				

α-Quartz (111)

Site	Coordination	Depth (Å)	Broken Bond Type	Length Broken Bond	Brown Strength Broken Bonds
O^{II}	1	1.746	Si^{IV}-O^{II}	1.613	-1.029
O^{II}	1	0.834	Si^{IV}-O^{II}	1.605	-1.052
Si^{IV}	3	1.290	Si^{IV}-O^{II}	1.613	1.029
Si^{IV}	3	1.061	Si^{IV}-O^{II}	1.605	1.052
O^{II}	2	0	-	-	-
O^{II}	2	1.160	-	-	-
O^{II}	2	1.420	-	-	-
O^{II}	2	1.519	-	-	-
Si^{IV}	4	2.581	-	-	-
#broken bonds:	7.9/nm^2		APS	1.0/nm^2	
#unsaturated atoms:	7.9/nm^2		ABS	1.0/nm^2	
#atoms within 1.4 Å depth:	13.9/nm^2		TBS	0	
#O atoms within 1.4 Å depth:	9.9/nm^2		Area unit cell:	0.5050 nm^2	
# sites from partial charges	7.9/nm^2				

Periclase (100)

Site	Coordination	Depth (Å)	Broken Bond Type	Length Broken Bond	Brown Strength Broken Bonds
Mg^{VI}	5	0	Mg^{VI}-O^{VI}	2.060	0.3709
Mg^{VI}	5	0	Mg^{VI}-O^{VI}	2.060	0.3709
O^{VI}	6	2.060	-	-	-
O^{VI}	6	2.060	-	-	-
O^{VI}	5	0	Mg^{VI}-O^{VI}	2.060	- 0.3709
O^{VI}	5	0	Mg^{VI}-O^{VI}	2.060	- 0.3709
Mg^{VI}	6	2.060	-	-	-
Mg^{VI}	6	2.060	-	-	-

APPENDIX

(continued)

Periclase (100)

#broken bonds:	23.6/nm^2		APS	7.8/nm^2	
#unsaturated atoms:	23.6/nm^2		ABS	8.7/nm^2	
#atoms within 1.4 Å depth:	23.6/nm^2		TBS	0	
#O atoms within 1.4 Å depth:	11.8/nm^2		Area Unit Cell:	0.1697 nm^2	
# sites from partial charges	0/nm2				

Periclase (110)

Site	Coordination	Depth (Å)	Broken Bond Type	Length Broken Bond	Brown Strength Broken Bonds
Mg^{VI}	6	1.457	-	-	-
O^{VI}	6	1.457	-	-	-
O^{VI}	4	0	Mg^{VI}-O^{VI}, Mg^{VI}-O^{VI}	2.060, 2.060	- 0.3709, -0.3709
Mg^{VI}	4	0	Mg^{VI}-O^{VI}, Mg^{VI}-O^{VI}	2.060, 2.060	0.3709, 0.3709
Mg^{VI}	6	2.914	-	-	-
Mg^{VI}	6	4.370	-	-	-
O^{VI}	6	2.914	-	-	-
O^{VI}	6	4.370	-	-	-
#broken bonds:	33.3/nm^2		APS	11.1/nm^2	
#unsaturated atoms:	16.7/nm^2		ABS	12.4/nm^2	
#atoms within 1.4 Å depth:	16.7/nm^2		TBS	0/nm^2	
#O atoms within 1.4 Å depth:	8.3/nm^2		Area Unit Cell:	0.1200 nm^2	
# sites from partial charges	16.7/nm^2				

Periclase (111)-positively charged

Site	Coordination	Depth(Å)	Broken Bond Type	Length Broken Bond	Brown Strength Broken Bonds
O^{VI}	6	1.189	-	-	-
Mg^{VI}	3	0	Mg^{VI}-O^{VI}, Mg^{VI}-O^{VI}, Mg^{VI}-O^{VI}	2.060, 2.060, 2.060	0.3709, 0.3709, 0.3709
O^{VI}	6	3.568	-	-	-
Mg^{VI}	6	2.378	-	-	-
Mg^{VI}	6	2.378	-	-	-
O^{VI}	6	1.189	-	-	-

APPENDIX

(continued)

Periclase (111)-positively charged

Mg^{VI}	3	0	Mg^{VI}-O^{VI}, Mg^{VI}-O^{VI}, Mg^{VI}-O^{VI}	2.060, 2.060, 2.060	0.3709, 0.3709, 0.3709
O^{VI}	6	3.568	-	-	-
#broken bonds:	40.8/nm^2		APS	13.6/nm^2	
#unsaturated atoms:	13.6/nm^2		ABS	15.1/nm^2	
#atoms within 1.4 Å depth:	27.2/nm^2		TBS	+15.1/nm^2	
#O atoms within 1.4 Å depth:	13.6/nm^2		Area Unit Cell:	0.1470 nm^2	
# sites from partial charges	13.6/nm^2				

Periclase (111)-negatively charged

Site	Coordination	Depth (Å)	Broken Bond Type	Length Broken Bond	Brown Strength Broken Bonds
O^{VI}	3	0	Mg^{VI}-O^{VI}, Mg^{VI}-O^{VI}, Mg^{VI}-O^{VI}	2.060, 2.060, 2.060	-0.3709, -0.3709, -0.3709
Mg^{VI}	6	3.568	-	-	-
O^{VI}	6	2.379	-	-	-
Mg^{VI}	6	1.189	-	-	-
Mg^{VI}	6	1.189	-	-	-
O^{VI}	3	0	Mg^{VI}-O^{VI}, Mg^{VI}-O^{VI}, Mg^{VI}-O^{VI}	2.060, 2.060, 2.060	-0.3709, -0.3709, -0.3709
Mg^{VI}	6	3.568	-	-	-
O^{VI}	6	2.379	-	-	-
#broken bonds:	40.8/nm^2		APS	13.6/nm^2	
#unsaturated atoms:	13.6/nm^2		ABS	15.1/nm^2	
#atoms within 1.4 Å depth:	27.2/nm^2		TBS	-15.1/nm^2	
#O atoms within 1.4 Å depth:	13.6/nm^2		Area Unit Cell:	0.1470 nm^2	
# sites from partial charges	13.6/nm^2				

Rutile (100)

Site	Coordination	Depth (Å)	Broken Bond Type	Length Broken Bond	Brown Strength Broken Bonds
Ti^{VI}	6	3.192	-	-	-
Ti^{VI}	5	0.895	Ti^{VI}-O^{III}	1.983	0.6344
O^{III}	2	0	Ti^{VI}-O^{III}	1.983	-0.6344
O^{III}	3	2.297	-	-	-

APPENDIX

(continued)

Rutile (100)

O^{III}	3	1.789	-	-	-
O^{III}	3	4.086	-	-	-
#broken bonds:	14.7/nm^2		APS	9.6/nm^2	
#unsaturated atoms:	14.7/nm^2		ABS	9.6/nm^2	
#atoms within 1.4 Å depth:	14.7/nm^2		TBS	0/nm^2	
#O atoms within 1.4 Å depth:	7.4/nm^2		Area Unit Cell:	0.1359 nm^2	
# sites from partial charges	14.7/nm^2				

Rutile (001)

Site	Coordination	Depth (Å)	Broken Bond Type	Length Broken Bond	Brown Strength Broken Bonds
Ti^{VI}	6	1.497	-	-	-
O^{III}	3	1.497	-	-	-
O^{III}	2	0	Ti^{VI}-O^{III}	1.946	-0.7015
Ti^{VI}	4	0	Ti^{VI}-O^{III}, Ti^{VI}-O^{III}	1.946, 1.946	0.7015, 0.7015
O^{III}	2	0	Ti^{VI}-O^{III}	1.946	-0.7015
O^{III}	3	1.497	-	-	-
#broken bonds:	19.0/nm^2		APS	12.7/nm^2	
#unsaturated atoms:	14.2/nm^2		ABS	13.3/nm^2	
#atoms within 1.4 Å depth:	14.2/nm^2		TBS	0/nm^2	
#O atoms within 1.4 Å depth:	9.5/nm^2		Area Unit Cell:	0.2110 nm^2	
# sites from partial charges	14.2/nm^2				

Rutile (110)

Site	Coordination	Depth (Å)	Broken Bonds	Length Broken Bond	Brown Strength Broken Bonds
Ti^{VI}	6	1.265	-	-	-
O^{III}	2	0	Ti^{VI}-O^{III},	1.983	-0.6344
O^{III}	3	1.265	-	-	-
Ti^{VI}	5	1.265	Ti^{VI}-O^{III}	1.983	0.6344
O^{III}	3	1.265	-	-	-
O^{III}	3	2.529	-	-	-
#broken bonds:	10.4/nm^2		APS	7.0/nm^2	
#unsaturated atoms:	10.4/nm^2		ABS	6.8/nm^2	
#atoms within 1.4 Å depth:	26.0/nm^2		TBS	0/nm^2	

APPENDIX

(continued)

Rutile (110)

#O atoms within 1.4 Å depth:	15.6/nm^2		Area Unit Cell:	0.1922 nm^2	
# sites from partial charges	10.4/nm^2				

Rutile (101)

Site	Coordination	Depth (Å)	Broken Bonds	Length Broken Bond	Brown Strength Broken Bonds
Ti^{VI}	5	0.759	Ti^{VI}-O^{III}	1.946	.7015
O^{III}	2	0	Ti^{VI}-O^{III}	1.946	-.7015
O^{III}	3	1.519			
Ti^{VI}	5	0.759	Ti^{VI}-O^{III}	1.946	.7015
O^{III}	2	0	Ti^{VI}-O^{III}	1.946	-.7015
O^{III}	3	1.519			
#broken bonds:	15.9/nm^2		APS	10.7/nm^2	
#unsaturated atoms:	15.9/nm^2		ABS	11.2/nm^2	
#atoms within 1.4 Å depth:	15.9/nm^2		TBS	0	
#O atoms within 1.4 Å depth:	8.0/nm^2		Area Unit Cell:	0.2510 nm^2	
# sites from partial charges	15.9/nm^2				

Rutile (111)

Site	Coordination	Depth (Å)	Broken Bonds	Length Broken Bond	Brown Strength Broken Bonds
Ti^{VI}	4	0	Ti^{VI}-O^{III}, Ti^{VI}-O^{III}	1.946, 1.946	.70146, .70146
Ti^{VI}	5	1.094	Ti^{VI}-O^{III}	1.983	0.6344
O^{III}	2	0	Ti^{VI}-O^{III}	1.946	-.7015
O^{III}	2	0	Ti^{VI}-O^{III}	1.946	-.7015
O^{III}	2	0.242	Ti^{VI}-O^{III}	1.983	-0.6344
O^{III}	3	1.946			
#broken bonds:	21.0/nm^2		APS	12.3/nm^2	
#unsaturated atoms:	17.5/nm^2		ABS	14.0/nm^2	
#atoms within 1.4 Å depth:	17.5/nm^2		TBS	0	
#O atoms within 1.4 Å depth:	10.5/nm^2		Area Unit Cell:	0.2854 nm^2	
# sites from partial charges	17.5/nm^2				

APPENDIX

(continued)

Goethite (100)

Site	Coordination	Depth (Å)	Broken Bond Type	Length Broken Bond	Brown Strength Broken Bonds
Fe^{VI}	5	0.916	Fe^{VI}-O^{IV}	2.093	0.4054
Fe^{VI}	6	5.891	-	-	-
Fe^{VI}	6	3.005	-	-	-
Fe^{VI}	6	7.980	-	-	-
H^{I}	1	3.652	-	-	-
H^{I}	1	0.269	-	-	-
H^{I}	1	5.244	-	-	-
O^{IV}	4	8.896	-	-	-
O^{IV}	4	3.921	-	-	-
O^{III}	3	7.443	-	-	-
O^{III}	3	2.468	-	-	-
O^{III}	3	6.428	-	-	-
O^{III}	3	1.453	-	-	-
O^{IV}	4	4.975	-	-	-
O^{IV}	3	0	Fe^{VI}-O^{IV}	2.093	-0.4054
H^{I}	1	8.627	-	-	-
#broken bonds:	14.4/nm^2		APS	7.2/nm^2	
#unsaturated atoms:	14.4/nm^2		ABS	5.8/nm^2	
#atoms within 1.4 Å depth:	21.6/nm^2		TBS	0/nm^2	
#O atoms within 1.4 Å depth:	7.2/nm^2		Area Unit Cell:	0.1391 nm^2	
# sites from partial charges	0/nm^2				

Goethite (010)

Site	Coordination	Depth (Å)	Broken Bond Type	Length Broken Bond	Brown Strength Broken Bonds
Fe^{VI}	4	0	Fe^{VI}-O^{III}, Fe^{VI}-O^{IV}	1.953, 2.089	0.5920, 0.4100
Fe^{VI}	6	1.505	-	-	-
Fe^{VI}	4	0	Fe^{VI}-O^{III}, Fe^{VI}-O^{IV}	1.953, 2.089	0.5920, 0.4100
Fe^{VI}	6	1.505	-	-	-
H^{I}	1	0	-	-	-
H^{I}	1	0	-	-	-
H^{I}	1	1.505	-	-	-
H^{I}	1	1.505	-	-	-
O^{III}	3	1.505	-	-	-
O^{IV}	3	0	Fe^{VI}-O^{IV}	2.089	-0.4100

APPENDIX

(continued)

Goethite (010)

O^{III}	3	1.505	-	-	-
O^{IV}	3	0	Fe^{VI}-O^{IV}	2.089	-0.4100
O^{IV}	4	1.505	-	-	-
O^{III}	2	0	Fe^{VI}-O^{III}	1.953	-0.5920
O^{IV}	4	1.505	-	-	-
O^{III}	2	0	Fe^{VI}-O^{III}	1.953	-0.5920
#broken bonds:	17.4/nm^2		APS	9.4/nm^2	
#unsaturated atoms:	13.1/nm^2		ABS	8.7/nm^2	
#atoms within 1.4 Å depth:	17.4/nm^2		TBS	0/nm^2	
#O atoms within 1.4 Å depth:	8.7/nm^2		Area Unit Cell:	0.4596 nm^2	
# sites from partial charges	8.7/nm^2				

Goethite (001)

Site	Coordination	Depth (Å)	Broken Bond Type	Length Broken Bond	Brown Strength Broken Bonds
Fe^{VI}	6	4.204	-	-	-
O^{III}	2	0.771	Fe^{VI}-O^{III}	1.954	-0.5899
H^{I}	1	3.858	-	-	-
O^{IV}	4	3.017	-	-	-
Fe^{VI}	6	2.310	-	-	-
O^{III}	3	1.123	-	-	-
H^{I}	1	2.656	-	-	-
O^{IV}	4	3.497	-	-	-
O^{IV}	2	0.707	Fe^{VI}-O^{IV}, Fe^{VI}-O^{IV}	2.089, 2.089	-0.4100, -0.4100
H^{I}	1	1.548	-	-	-
O^{III}	3	3.081	-	-	-
Fe^{VI}	6	1.894	-	-	-
O^{IV}	4	1.187	-	-	-
H^{I}	1	0.346	-	-	-
O^{III}	3	3.433	-	-	-
Fe^{VI}	3	0	Fe^{VI}-O^{III}, Fe^{VI}-O^{IV}, Fe^{VI}-O^{IV}	1.954, 2.089, 2.089	0.5899, 0.4100, 0.4100
#broken bonds:	20.0/nm^2		APS	10.6/nm^2	
#unsaturated atoms:	10.0/nm^2		ABS	9.4/nm^2	
#atoms within 1.4 Å depth:	20.0/nm^2		TBS	0/nm^2	
#O atoms within 1.4 Å depth:	13.4/nm^2		Area Unit Cell:	0.2995 nm^2	
# sites from partial charges	10.0/nm^2				

APPENDIX

(continued)

Corundum (100)

Site	Coordination	Depth (Å)	Broken Bond Type	Length Broken Bond	Brown Strength Broken Bonds
O^{IV}	4	1.375	-	-	-
O^{IV}	3	0.111	Al^{VI}-O^{IV}	1.855	-0.5755
O^{IV}	4	2.970	-	-	-
O^{IV}	2	0	Al^{VI}-O^{IV}, Al^{VI}-O^{IV}	1.972, 1.972	-0.4195, -0.4195
O^{IV}	4	2.860	-	-	-
O^{IV}	4	1.596	-	-	-
O^{IV}	4	1.485	-	-	-
O^{IV}	3	0.221	Al^{VI}-O^{IV}	1.855	-0.5755
O^{IV}	4	2.749	-	-	-
O^{IV}	3	0.111	Al^{VI}-O^{IV}	1.855	-0.5755
O^{IV}	4	2.970	-	-	-
O^{IV}	4	1.375	-	-	-
O^{IV}	4	1.596	-	-	-
O^{IV}	2	0	Al^{VI}-O^{IV}, Al^{VI}-O^{IV}	1.972, 1.972	-0.4195, -0.4195
O^{IV}	4	2.860	-	-	-
O^{IV}	3	0.221	Al^{VI}-O^{IV}	1.855	-0.5755
O^{IV}	4	2.749	-	-	-
O^{IV}	4	1.485	-	-	-
Al^{VI}	6	1.485	-	-	-
Al^{VI}	6	2.860	-	-	-
Al^{VI}	4	0.111	Al^{VI}-O^{IV}, Al^{VI}-O^{IV}	1.855, 1.972	0.5755, 0.4195
Al^{VI}	6	1.485	-	-	-
Al^{VI}	6	2.860	-	-	-
Al^{VI}	4	0.111	Al^{VI}-O^{IV}, Al^{VI}-O^{IV}	1.855, 1.972	0.5755, 0.4195
Al^{VI}	6	1.485	-	-	-
Al^{VI}	6	2.860	-	-	-
Al^{VI}	4	0.111	Al^{VI}-O^{IV}, Al^{VI}-O^{IV}	1.855, 1.972	0.5755, 0.4195
Al^{VI}	6	1.485	-	-	-
Al^{VI}	6	2.860	-	-	-
Al^{VI}	4	0.111	Al^{VI}-O^{IV}, Al^{VI}-O^{IV}	1.855, 1.972	0.5755, 0.4195
#broken bonds:	25.9/nm^2		APS	12.9/nm^2	

APPENDIX

(continued)

Corundum (100)

#unsaturated atoms:	16.2/nm^2		ABS	12.9/nm^2	
#atoms within 1.4 Å depth:	19.4/nm^2		TBS	0/nm^2	
#O atoms within 1.4 Å depth:	12.9/nm^2		Area Unit Cell:	0.6188 nm^2	
# sites from partial charges	16.2/nm^2				

Corundum (001)

Site	Coordination	Depth (Å)	Broken Bond Type	Length Broken Bond	Brown Strength Broken Bonds
Al^{VI}	6	1.678	-	-	-
Al^{VI}	6	2.166	-	-	-
Al^{VI}	3	0	Al^{VI}-O^{IV}, Al^{VI}-O^{IV}, Al^{VI}-O^{IV}	1.972, 1.972, 1.972	0.4195, 0.4195, 0.4195
Al^{VI}	6	4.513	-	-	-
Al^{VI}	6	6.009	-	-	-
Al^{VI}	6	3.844	-	-	-
Al^{VI}	6	8.175	-	-	-
Al^{VI}	6	8.663	-	-	-
Al^{VI}	6	6.497	-	-	-
Al^{VI}	6	10.829	-	-	-
Al^{VI}	6	12.507	-	-	-
Al^{VI}	6	10.341	-	-	-
O^{IV}	4	3.004	-	-	-
O^{IV}	3	0.839	Al^{VI}-O^{IV}	1.972	-0.4195
O^{IV}	4	3.005	-	-	-
O^{IV}	3	0.839	Al^{VI}-O^{IV}	1.972	-0.4195
O^{IV}	3	0.839	Al^{VI}-O^{IV}	1.972	-0.4195
O^{IV}	4	3.005	-	-	-
O^{IV}	4	7.336	-	-	-
O^{IV}	4	5.170	-	-	-
O^{IV}	4	7.336	-	-	-
O^{IV}	4	5.170	-	-	-
O^{IV}	4	5.170	-	-	-
O^{IV}	4	7.336	-	-	-
O^{IV}	4	11.668	-	-	-
O^{IV}	4	9.502	-	-	-
O^{IV}	4	11.668	-	-	-
O^{IV}	4	9.502	-	-	-
O^{IV}	4	9.502	-	-	-
O^{IV}	4	11.668	-	-	-

APPENDIX

(continued)

Corundum (001)

#broken bonds:	30.5/nm^2		APS	15.3/nm^2	
#unsaturated atoms:	20.4nm^2		ABS	12.7/nm^2	
#atoms within 1.4 Å depth:	20.4/nm^2		TBS	0/nm^2	
#O atoms within 1.4 Å depth:	15.3/nm^2		Area Unit Cell:	0.1964 nm^2	
# sites from partial charges	5.1/nm^2				

Corundum (1-12)

Site	Coordination	Depth (Å)	Broken Bond Type	Length Broken Bond	Brown Strength Broken Bonds
Al^{VI}	5	0.356	Al^{VI}-O^{IV}	1.855	0.5755
Al^{VI}	5	0.356	Al^{VI}-O^{IV}	1.855	0.5755
O^{IV}	3	0	Al^{VI}-O^{IV}	1.855	-0.5755
O^{IV}	3	0	Al^{VI}-O^{IV}	1.855	-0.5755
Al^{VI}	6	5.260	-	-	-
Al^{VI}	6	5.260	-	-	-
Al^{VI}	6	8.742	-	-	-
Al^{VI}	6	8.742	-	-	-
Al^{VI}	6	1.778	-	-	-
Al^{VI}	6	1.778	-	-	-
Al^{VI}	6	3.838	-	-	-
Al^{VI}	6	3.838	-	-	-
Al^{VI}	6	7.319	-	-	-
Al^{VI}	6	7.319	-	-	-
O^{IV}	4	1.067	-	-	-
O^{IV}	4	1.067	-	-	-
O^{IV}	4	2.134	-	-	-
O^{IV}	4	2.134	-	-	-
O^{IV}	4	3.482	-	-	-
O^{IV}	4	3.482	-	-	-
O^{IV}	4	4.549	-	-	-
O^{IV}	4	4.549	-	-	-
O^{IV}	4	5.616	-	-	-
O^{IV}	4	5.616	-	-	-
O^{IV}	4	6.964	-	-	-
O^{IV}	4	6.964	-	-	-
O^{IV}	4	8.031	-	-	-
O^{IV}	4	8.031	-	-	-
O^{IV}	4	9.098	-	-	-
O^{IV}	4	9.098	-	-	-
#broken bonds:	16.4/nm^2		APS	8.2/nm^2	

APPENDIX

(continued)

Corundum (1-12)

#unsaturated atoms:	16.4/nm^2		ABS	9.4/nm^2	
#atoms within 1.4 Å depth:	24.6/nm^2		TBS	0/nm^2	
#O atoms within 1.4 Å depth:	16.4/nm^2		Area Unit Cell:	0.2443 nm^2	
# sites from partial charges	16.4/nm^2				

Hematite (100)

Site	Coordination	Depth (Å)	Broken Bond Type	Length Broken Bond	Brown Strength Broken Bonds
O^{IV}	4	1.454	-	-	-
O^{IV}	3	0.119	Fe^{VI}-O^{IV}	1.946	-0.6038
O^{IV}	4	3.148	-	-	-
O^{IV}	2	0	Fe^{VI}-O^{IV}, Fe^{VI}-O^{IV}	2.116, 2.116	-0.3808, -0.3808
O^{IV}	4	3.028	-	-	-
O^{IV}	4	1.693	-	-	-
O^{IV}	4	1.574	-	-	-
O^{IV}	3	0.239	Fe^{VI}-O^{IV}	1.946	-0.6038
O^{IV}	4	2.908	-	-	-
O^{IV}	3	0.119	Fe^{VI}-O^{IV}	1.946	-0.6038
O^{IV}	4	3.148	-	-	-
O^{IV}	4	1.454	-	-	-
O^{IV}	4	1.693	-	-	-
O^{IV}	2	0	Fe^{VI}-O^{IV}, Fe^{VI}-O^{IV}	2.116, 2.116	-0.3808, -0.3808
O^{IV}	4	3.028	-	-	-
O^{IV}	3	0.239	Fe^{VI}-O^{IV}	1.946	-0.6038
O^{IV}	4	2.908	-	-	-
O^{IV}	4	1.574	-	-	-
Fe^{VI}	6	1.574	-	-	-
Fe^{VI}	6	3.028	-	-	-
Fe^{VI}	4	0.119	Fe^{VI}-O^{IV}, Fe^{VI}-O^{IV}	1.946, 2.116	0.6038, 0.3808
Fe^{VI}	6	1.574	-	-	-
Fe^{VI}	6	3.028	-	-	-
Fe^{VI}	4	0.119	Fe^{VI}-O^{IV}, Fe^{VI}-O^{IV}	1.946, 2.11	0.6038, 0.3808
Fe^{VI}	6	1.574	-	-	-
Fe^{VI}	6	3.028	-	-	-
Fe^{VI}	4	0.119	Fe^{VI}-O^{IV}, Fe^{VI}-O^{IV}	1.946, 2.116	0.6038, 0.3808
Fe^{VI}	6	1.574	-	-	-

APPENDIX

(continued)

Hematite (100)

Fe^{VI}	6	3.028	-	-	-
Fe^{VI}	4	0.119	Fe^{VI}-O^{IV}, Fe^{VI}-O^{IV}	1.946, 2.116	0.6038, 0.3808
#broken bonds:	23.1/nm^2		APS	11.5/nm^2	
#unsaturated atoms	14.4/nm^2		ABS	11.4/nm^2	
#atoms w/in 1.4 Å	14.4/nm^2		TBS	0/nm^2	
#O atoms w/in 1.4 Å	8.6/nm^2		Area Unit Cell:	0.6938 nm^2	
# sites from partial charges	14.4/nm^2				

Hematite (001)

Site	Coordination	Depth (Å)	Broken Bond Type	Length Broken Bond	Brown Strength Broken Bonds
Fe^{VI}	6	1.690	-	-	-
Fe^{VI}	6	2.295	-	-	-
Fe^{VI}	3	0	Fe^{VI}-O^{IV}, Fe^{VI}-O^{IV}, Fe^{VI}-O^{IV}	2.116, 2.116, 2.116	0.3808, 0.3808, 0.3808
Fe^{VI}	6	4.590	-	-	-
Fe^{VI}	6	6.280	-	-	-
Fe^{VI}	6	3.985	-	-	-
Fe^{VI}	6	8.576	-	-	-
Fe^{VI}	6	9.180	-	-	-
Fe^{VI}	6	6.886	-	-	-
Fe^{VI}	6	11.476	-	-	-
Fe^{VI}	6	13.166	-	-	-
Fe^{VI}	6	10.871	-	-	-
O^{IV}	4	3.140	-	-	-
O^{IV}	3	0.845	Fe^{VI}-O^{IV}	2.116	-0.3808
O^{IV}	4	3.140	-	-	-
O^{IV}	3	0.845	Fe^{VI}-O^{IV}	2.116	-0.3808
O^{IV}	3	0.845	Fe^{VI}-O^{IV}	2.116	-0.3808
O^{IV}	4	3.140	-	-	-
O^{IV}	4	7.731	-	-	-
O^{IV}	4	5.435	-	-	-
O^{IV}	4	7.731	-	-	-
O^{IV}	4	5.435	-	-	-
O^{IV}	4	5.435	-	-	-
O^{IV}	4	7.731	-	-	-
O^{IV}	4	12.321	-	-	-
O^{IV}	4	10.026	-	-	-
O^{IV}	4	12.321	-	-	-
O^{IV}	4	10.026	-	-	-

APPENDIX

(continued)

Hematite (001)

O^{IV}	4	10.026	-	-	-
O^{IV}	4	12.321	-	-	-
#broken bonds:	27.3/nm^2		APS	13.6/nm^2	
#unsaturated atoms	18.2/nm^2		ABS	10.4/nm^2	
#atoms w/in 1.4 Å	18.2/nm^2		TBS	0/nm^2	
#O atoms w/in 1.4 Å	13.6/nm^2		Area Unit Cell:	0.2198 nm^2	
# sites from partial charges	4.5/nm^2				

Hematite (1-12)

Site	Coordination	Depth (Å)	Broken Bond Type	Length Broken Bond	Brown Strength Broken Bonds
Fe^{VI}	5	0.352	Fe^{VI}-O^{IV}	1.946	0.6038
Fe^{VI}	5	0.352	Fe^{VI}-O^{IV}	1.946	0.6038
Fe^{VI}	6	1.904	-	-	-
Fe^{VI}	6	1.904	-	-	-
Fe^{VI}	6	4.037	-	-	-
Fe^{VI}	6	4.037	-	-	-
Fe^{VI}	6	5.589	-	-	-
Fe^{VI}	6	5.589	-	-	-
Fe^{VI}	6	7.723	-	-	-
Fe^{VI}	6	7.723	-	-	-
O^{IV}	4	0	Fe^{VI}-O^{IV}	1.946	-0.6038
O^{IV}	4	0	Fe^{VI}-O^{IV}	1.946	-0.6038
O^{IV}	3	1.128	-	-	-
O^{IV}	3	1.128	-	-	-
O^{IV}	4	2.255	-	-	-
O^{IV}	4	2.255	-	-	-
O^{IV}	4	3.686	-	-	-
O^{IV}	4	3.686	-	-	-
O^{IV}	4	4.813	-	-	-
O^{IV}	4	4.813	-	-	-
O^{IV}	4	5.941	-	-	-
O^{IV}	4	5.941	-	-	-
O^{IV}	4	7.371	-	-	-
O^{IV}	4	7.371	-	-	-
O^{IV}	4	8.499	-	-	-
O^{IV}	4	8.499	-	-	-
O^{IV}	4	9.626	-	-	-
O^{IV}	4	9.626	-	-	-
Fe^{VI}	6	9.275	-	-	-
Fe^{VI}	6	9.275	-	-	-

APPENDIX

(continued)

Hematite (1-12)

#broken bonds:	14.5/nm^2		APS	7.2/nm^2	
#unsaturated atoms	14.5/nm^2		ABS	8.7/nm^2	
#atoms w/in 1.4 Å	21.7/nm^2		TBS	0/nm^2	
#O atoms w/in 1.4 Å	14.5/nm^2		Area Unit Cell:	0.2763 nm^2	
# sites from partial charges	14.5/nm^2				

Andalusite (100)

Site	Coordination	Depth (Å)	Broken Bond Type	Length Broken Bond	Brown Strength Broken Bonds
Al^{VI}	6	5.82	-	-	-
Al^{VI}	6	5.82	-	-	-
O^{III}	3	5.22	-	-	-
O^{II}	2	7.61	-	-	-
Al^{V}	3	0.91	Al^{V}- O^{II}, Al^{V}- O^{II}	1.818, 1.818	0.6366, 0.6366
O^{III}	3	5.22	-	-	-
O^{III}	3	2.73	-	-	-
O^{II}	2	7.61	-	-	-
Si^{IV}	4	7.74	-	-	-
Si^{IV}	4	3.84	-	-	-
O^{III}	2	1.33	Si^{IV}-O^{III}	1.636	-0.9691
Al^{V}	5	4.81	-	-	-
O^{III}	3	6.63	-	-	-
O^{II}	2	3.71	-	-	-
O^{III}	3	1.32	-	-	-
O^{II}	2	3.71	-	-	-
Al^{VI}	6	1.92	-	-	-
Al^{VI}	6	1.92	-	-	-
O^{III}	3	5.01	-	-	-
Al^{V}	5	6.82	-	-	-
O^{III}	3	2.51	-	-	-
O^{II}	1	0.12	Al^{V}- O^{II}	1.818	-0.6366
O^{III}	3	2.52	-	-	-
O^{II}	1	0.12	Al^{V}- O^{II}	1.818	-0.6366
Si^{IV}	4	3.90	-	-	-
Si^{IV}	3	0	Si^{IV}-O^{III}	1.636	0.9691
O^{III}	3	6.42	-	-	-
O^{II}	2	4.02	-	-	-
O^{III}	3	6.41	-	-	-
Al^{V}	5	2.93	-	-	-
O^{III}	3	1.11	-	-	-

APPENDIX

(continued)

Andalusite (100)

O^{II}	2	4.02	-	-	-
#broken bonds:	13.7/nm^2		APS	11.1/nm^2	
#unsaturated atoms:	11.4/nm^2		ABS	10.2/nm^2	
#atoms within 1.4 Å depth:	15.9/nm^2		TBS	0/nm^2	
#O atoms within 1.4 Å depth:	11.4/nm^2		Area Unit Cell:	0.4391 nm^2	
# sites from partial charges	11.4/nm^2				

Andalusite (010)

Site	Coord	Depth	Broken Bonds	Length Broken Bond	Brown Strength Broken Bonds
O^{III}	3	4.816	-	-	-
O^{III}	3	1.172	-	-	-
Al^{V}	5	3.047	-	-	-
Si^{IV}	2	0	Si^{IV}-O^{II}, Si^{IV}-O^{II}	1.630, 1.630	0.9829, 0.9829
O^{III}	3	0.868	-	-	-
O^{III}	3	3.034	-	-	-
Si^{IV}	4	3.903	-	-	-
O^{III}	3	2.731	-		-
Al^{V}	4	0.856	Al^{V}-O^{III}	1.816	0.6406
O^{III}	3	6.985	-	-	-
Al^{VI}	6	5.901	-	-	-
O^{II}	2	6.961	-	-	-
O^{II}	2	3.012	-	-	-
Al^{VI}	6	1.951	-	-	-
O^{II}	1	0.890	Si^{IV}-O^{II}	1.630	-0.9829
O^{II}	2	4.840	-	-	-
O^{III}	3	4.818	-	-	-
Si^{IV}	4	3.949	-	-	-
O^{III}	3	5.121	-	-	-
Al^{V}	5	6.996	-	-	-
O^{III}	2	0.867	Al^{V}-O^{III}	1.816	-0.6406
O^{III}	3	3.036	-	-	-
Al^{V}	5	4.805	-	-	-
O^{III}	3	6.680	-	-	-
Si^{IV}	4	7.852	-	-	-
O^{III}	3	6.983	-	-	-
Al^{VI}	6	5.901	-	-	-
O^{II}	2	6.961	-	-	-
O^{II}	2	3.012	-	-	-

APPENDIX

(continued)

Andalusite (010)

Al^{VI}	6	1.951	-	-	-
O^{II}	1	0.890	Si^{IV} - O^{II}	1.630	-0.9829
O^{II}	2	4.840	-	-	-
#broken bonds:	13.8/nm^2		APS	12.9/nm^2	
#unsaturated atoms:	11.5/nm^2		ABS	12.0/nm^2	
#atoms within 1.4 Å depth	16.2/nm^2		TBS	0/nm^2	
#O atoms within 1.4 Å depth	11.5/nm^2		Area Unit Cell:	0.4333 nm^2	
# sites from partial charges	13.8/nm^2				

Andalusite (001)

Site	Coordination	Depth (Å)	Broken Bond Type	Length Broken Bond	Brown Strength Broken Bonds
Si^{IV}	4	4.116	-	-	-
Si^{IV}	4	1.337	-	-	-
Si^{IV}	4	1.337	-	-	-
Si^{IV}	4	4.116	-	-	-
Al^{V}	4	1.337	Al^{V} - O^{II}	1.818	0.6366
Al^{IV}	2	0	Al^{V} -O^{III}, Al^{V} - O^{III}	1.891, 1.891	0.5222, 0.5222
Al^{V}	4	1.337	Al^{V} - O^{II}	1.818	0.6336
Al^{V}	5	4.116	-	-	-
Al^{V}	5	4.116	-	-	-
Al^{IV}	4	2.770	-	-	-
Al^{IV}	4	2.683	-	-	-
Al^{IV}	4	5.462	-	-	-
O^{II}	2	2.787	-	-	-
O^{III}	3	1.337	-	-	-
O^{III}	2	1.337	Al^{V} -O^{III}	1.891	-0.5222
O^{III}	3	4.116	-	-	-
O^{III}	3	1.337	-	-	-
O^{II}	1	0.008	Al^{V} - O^{II}	1.818	-0.6366
O^{II}	1	0.008	Al^{V} - O^{II}	1.818	-0.6366
O^{III}	3	1.337	-	-	-
O^{III}	3	4.116	-	-	-
O^{III}	2	1.337	Al^{V} -O^{III}	1.891	-0.5222
O^{III}	3	1.337	-	-	-
O^{II}	2	2.787	-	-	-
O^{II}	2	2.665	-	-	-
O^{II}	2	2.665	-	-	-
O^{II}	2	5.445	-	-	-
O^{III}	3	4.116	-	-	-

APPENDIX

(continued)

Andalusite (001)

O^{III}	3	4.116	-	-	-
O^{III}	3	4.116	-	-	-
O^{III}	3	4.116	-	-	-
O^{II}	2	5.445	-	-	-
#broken bonds:	13.0/nm^2		APS	9.0/nm^2	
#unsaturated atoms:	11.4/nm^2		ABS	7.5/nm^2	
#atoms within 1.4 Å depth:	21.1/nm^2		TBS	0/nm^2	
#O atoms within 1.4 Å depth:	13.0/nm^2		Area Unit Cell:	0.6156 nm^2	
# sites from partial charges	11.4/nm^2				

Andalusite (011)

Site	Coordination	Depth (Å)	Broken Bond Type	Length Broken Bond	Brown Strength Broken Bonds
Al^{IV}	3	0.625	Al^{IV}-O^{III},	1.830	0.6173
Al^{IV}	3	0.625	Al^{IV}-O^{III}	1.830	0.6173
O^{III}	2	0.148	Al^{IV}-O^{III}	1.830	-0.6173
O^{III}	2	0.148	Al^{IV}-O^{III}	1.830	-0.6173
O^{II}	1	0	Si^{IV} - O^{II}	1.630	-0.9829
O^{II}	1	0	Si^{IV} - O^{II}	1.630	-0.9829
Si^{IV}	3	0.674	Si^{IV} - O^{II}	1.630	0.9829
Si^{IV}	3	0.674	Si^{IV} - O^{II}	1.630	0.9829
Al^{IV}	4	2.969	-	-	-
Al^{IV}	4	2.924	-	-	-
Al^{V}	5	2.427	-	-	-
Al^{V}	5	1.166	-	-	-
Al^{V}	5	1.166	-	-	-
Al^{V}	5	2.427	-	-	-
O^{III}	3	3.446	-	-	-
O^{III}	3	3.446	-	-	-
O^{III}	3	2.420	-	-	-
O^{III}	3	1.174	-	-	-
O^{III}	3	2.420	-	-	-
O^{III}	3	1.174	-	-	-
O^{III}	3	1.348	-	-	-
O^{III}	3	2.246	-	-	-
O^{III}	3	2.246	-	-	-
O^{III}	3	1.348	-	-	-
O^{II}	2	3.594	-	-	-
O^{II}	2	1.221	-	-	-

APPENDIX

(continued)

Andalusite (011)

O^{II}	2	2.373	-	-	-
O^{II}	2	3.594	-	-	-
O^{II}	2	1.221	-	-	-
O^{II}	2	2.373	-	-	-
Si^{IV}	4	2.920	-	-	-
Si^{IV}	4	2.920	-	-	-
#broken bonds:	10.6/nm^2		APS	9.1/nm^2	
#unsaturated atoms	10.6/nm^2		ABS	8.5/nm^2	
#atoms within 1.4 Å depth:	21.3/nm^2		TBS	0	
#O atoms within 1.4 Å depth:	13.3/nm^2		Area Unit Cell:	0.7528 nm^2	
# sites from partial charges	10.6/nm^2				

Sillimanite (100)

Site	Coordination	Depth (Å)	Broken Bond Type	Length Broken Bond	Brown Strength Broken Bonds
Al^{VI}	6	4.892	-	-	-
Al^{VI}	6	4.892	-	-	-
Al^{IV}	4	2.211	-	-	-
Al^{IV}	4	5.954	-	-	-
Al^{VI}	6	1.149	-	-	-
Al^{VI}	6	1.149	-	-	-
Al^{IV}	4	3.829	-	-	-
Al^{IV}	3	0.087	Al^{IV}-O^{III}	1.758	0.7495
Si^{IV}	4	2.298	-	-	-
Si^{IV}	4	6.041	-	-	-
Si^{IV}	4	3.743	-	-	-
Si^{IV}	3	0	Si^{IV}-O^{III}	1.629	0.9858
O^{II}	2	0.964	-	-	-
O^{II}	2	1.334	-	-	-
O^{III}	3	3.826	-	-	-
O^{III}	3	3.843	-	-	-
O^{III}	3	5.826	-	-	-
O^{III}	3	2.083	-	-	-
O^{III}	3	5.826	-	-	-
O^{III}	3	2.083	-	-	-
O^{III}	2	0.100	Si^{IV}-O^{III}	1.629	-0.9858
O^{II}	2	5.076	-	-	-
O^{III}	3	2.215	-	-	-
O^{III}	2	0.083	Al^{IV}-O^{III}	1.758	-0.7495
O^{II}	2	4.707	-	-	-

APPENDIX

(continued)

Sillimanite (100)

O^{III}	3	2.198	-	-	-
O^{III}	3	0.215	-	-	-
O^{III}	3	3.957	-	-	-
O^{III}	3	0.215	-	-	-
O^{III}	3	3.957	-	-	-
O^{III}	3	5.940	-	-	-
O^{III}	3	5.958	-	-	-
#broken bonds:	9.0/nm^2		APS	7.0/nm^2	
#unsaturated atoms:	9.0/nm^2		ABS	7.8/nm^2	
#atoms within 1.4 Å depth:	22.6/nm^2		TBS	0/nm^2	
#O atoms within 1.4 Å depth:	13.6/nm^2		Area Unit Cell:	0.4428 nm^2	
# sites from partial charges	9.0/nm^2				

Sillimanite (010)

Site	Coordination	Depth (Å)	Broken Bond Type	Length Broken Bond	Brown Strength Broken Bonds
O^{III}	1	0.000	Al^{IV}-O^{III}, Si^{IV}-O^{III}	1.800, 1.632	-0.6680, -0.9776
O^{III}	1	0.000	Al^{IV}-O^{III}, Si^{IV}-O^{III}	1.800, 1.632	-0.6680, -0.9776
Al^{IV}	2	0.525	Al^{IV}-O^{III}, Al^{IV}-O^{III}	1.800, 1.800	0.6680, 0.6680
Si^{IV}	2	0.492	Si^{IV}-O^{III}, Si^{IV}-O^{III}	1.632, 1.632	0.9776, 0.9776
Al^{VI}	6	1.717	-	-	-
Al^{VI}	6	1.717	-	-	-
Al^{VI}	6	5.554	-	-	-
Al^{VI}	6	5.554	-	-	-
Al^{IV}	4	4.362	-	-	-
Al^{IV}	4	6.746	-	-	-
Al^{IV}	4	2.909	-	-	-
Si^{IV}	3	4.329	-	-	-
Si^{IV}	4	2.942	-	-	-
Si^{IV}	4	6.779	-	-	-
O^{II}	2	1.711	-	-	-
O^{II}	2	5.548	-	-	-
O^{II}	2	1.723	-	-	-
O^{II}	2	5.560	-	-	-
O^{III}	3	3.434	-	-	-
O^{III}	3	3.837	-	-	-

APPENDIX

(continued)

Sillimanite (010)

O^{III}	3	2.214	-	-	-
O^{II}	2	1.009	-	-	-
O^{III}	3	2.424	-	-	-
O^{III}	2	3.434	-	-	-
O^{III}	3	3.837	-	-	-
O^{III}	3	4.846	-	-	-
O^{III}	3	1.220	-	-	-
O^{III}	3	5.057	-	-	-
O^{III}	3	7.270	-	-	-
O^{III}	3	7.270	-	-	-
O^{III}	3	6.051	-	-	-
O^{III}	3	6.261	-	-	-
#broken bonds:	18.5/nm^2		APS	14.3/nm^2	
#unsaturated atoms:	9.3/nm^2		ABS	15.2/nm^2	
#atoms within 1.4 Å depth:	13.9/nm^2		TBS	0/nm^2	
#O atoms within 1.4 Å depth:	9.3/nm^2		Area Unit Cell:	0.4319 nm^2	
# sites from partial charges	16.2/nm^2				

Sillimanite (001)-positively charged

Site	Coordination	Depth (Å)	Broken Bond Type	Length Broken Bond	Brown Strength Broken Bonds
Al^{VI}	6	1.443	-	-	-
Al^{IV}	3	0	Al^{IV}-O^{III}	1.800	0.6680
Al^{IV}	3	0	Al^{IV}-O^{III}	1.800	0.6680
Al^{VI}	6	1.443	-	-	-
Al^{IV}	4	2.885	-	-	-
Al^{IV}	4	2.885	-	-	-
Al^{VI}	6	4.328	-	-	-
Al^{VI}	6	4.328	-	-	-
Si^{IV}	4	2.885	-	-	-
Si^{IV}	3	0	Si^{IV}-O^{III}	1.632	0.9776
Si^{IV}	4	2.885	-	-	-
Si^{IV}	3	0	Si^{IV}-O^{III}	1.632	0.9766
O^{II}	2	0	-	-	-
O^{II}	2	2.885	-	-	-
O^{III}	2	0	Al^{VI}-O^{III}	1.861	-0.5666
O^{III}	3	2.885	-	-	-
O^{III}	3	1.348	-	-	-
O^{III}	3	1.538	-	-	-
O^{II}	2	2.885	-	-	-

APPENDIX

(continued)

Sillimanite (001)-positively charged

O^{II}	2	0	-	-	-
O^{III}	2	0	Al^{VI}-O^{III}	1.919	-0.4852
O^{III}	3	2.885	-	-	-
O^{III}	2	0	Al^{VI}-O^{III}	1.861	-0.5666
O^{III}	3	2.885	-	-	-
O^{III}	3	1.348	-	-	-
O^{III}	3	1.538	-	-	-
O^{III}	2	0	Al^{VI}-O^{III}	1.919	-0.4852
O^{III}	3	2.885	-	-	-
O^{III}	3	4.233	-	-	-
O^{III}	3	4.422	-	-	-
O^{III}	3	4.233	-	-	-
O^{III}	3	4.422	-	-	-
#broken bonds:	13.9/nm^2		APS	10.4/nm^2	
#unsaturated atoms:	13.9/nm^2		ABS	9.4/nm^2	
#atoms within 1.4 Å depth:	20.9/nm^2		TBS	+2.1/nm^2	
#O atoms within 1.4 Å depth	13.9/nm^2		Area Unit Cell:	0.5745 nm^2	
# sites from partial charges	10.4/nm^2				

Sillimanite (001)-negatively charged

Site	Coordination	Depth (Å)	Broken Bond Type	Length Broken Bond	Brown Strength Broken Bonds
Al^{VI}	4	0.095	Al^{VI}-O^{III}, Al^{VI}-O^{III}	1.861, 1.919	0.5666, 0.4852
Al^{IV}	4	4.422	-	-	-
Al^{IV}	4	1.537	-	-	-
Al^{VI}	4	0.095	Al^{VI}-O^{III}, Al^{VI}-O^{III}	1.861, 1.919	0.5666, 0.4852
Al^{IV}	4	4.422	-	-	-
Al^{IV}	4	1.537	-	-	-
Al^{VI}	6	2.980	-	-	-
Al^{VI}	6	2.980	-	-	-
Si^{IV}	4	1.537	-	-	-
Si^{IV}	4	4.422	-	-	-
Si^{IV}	4	1.537	-	-	-
Si^{IV}	4	4.422	-	-	-
O^{II}	2	4.422	-	-	-
O^{II}	2	1.537	-	-	-
O^{III}	3	4.422	-	-	-
O^{III}	3	1.537	-	-	-

APPENDIX

(continued)

Sillimanite (001)-negatively charged

O^{III}	2	0	Si^{IV}-O^{III}	1.632	-0.9776
O^{III}	2	0.190	Al^{IV}-O^{III}	1.800	-0.6680
O^{II}	2	1.537	-	-	-
O^{II}	2	4.422	-	-	-
O^{III}	3	4.422	-	-	-
O^{III}	3	1.537	-	-	-
O^{III}	3	4.422	-	-	-
O^{III}	3	1.537	-	-	-
O^{III}	2	0	Si^{IV}-O^{III}	1.632	-0.9776
O^{III}	2	0.190	Al^{IV}-O^{III}	1.800	-0.6680
O^{III}	3	4.422	-	-	-
O^{III}	3	1.537	-	-	-
O^{III}	3	2.885	-	-	-
O^{III}	3	2.885	-	-	-
O^{III}	3	3.074	-	-	-
O^{III}	3	3.074			
#broken bonds:	13.9/nm^2		APS	8.1/nm^2	
#unsaturated atoms:	10.4/nm^2		ABS	9.4/nm^2	
#atoms within 1.4 Å depth:	10.4/nm^2		TBS	-2.1/nm^2	
#O atoms within 1.4 Å depth:	7.0/nm^2		Area Unit Cell:	0.5745 nm^2	
# sites from partial charges	10.4/nm^2				

Sillimanite (110)

Site	Coordination	Depth (Å)	Broken Bond Type	Length Broken Bond	Brown Strength Broken Bonds
Al^{IV}	4	3.733	-	-	-
Al^{IV}	3	0.039	Al^{IV}-O^{III}	1.758	0.7495
Al^{VI}	6	2.646	-	-	-
Al^{VI}	6	2.646	-	-	-
Al^{IV}	4	1.560	-	-	-
Al^{IV}	3	5.254	Al^{IV}-O^{II}	1.729	0.8095
Al^{VI}	6	2.646	-	-	-
Al^{VI}	6	2.646	-	-	-
O^{III}	2	1.362	Si^{IV} - O^{II}	-1.554	-0.9858
O^{III}	2	2.351	-	-	-
O^{III}	3	2.864	-	-	-
O^{III}	3	3.852	-	-	-
O^{III}	3	1.497	-	-	-
O^{III}	3	2.191	-	-	-
O^{II}	1	3.023	Al^{IV}-O^{III}	-1.758	-0.7495

APPENDIX

(continued)

Sillimanite (110)

O^{III}	3	3.718	-	-	-
O^{III}	3	0.065	-	-	-
O^{III}	3	0.056	-	-	-
O^{III}	3	5.150	-	-	-
O^{III}	3	5.158	-	-	-
O^{III}	2	0.740	Si^{IV}-O^{III}	-1.629	-0.9858
O^{III}	3	0.740	-	-	-
O^{III}	3	2.077	-	-	-
O^{III}	3	2.077	-	-	-
O^{III}	3	3.137	-	-	-
O^{II}	2	3.137	-	-	-
O^{III}	3	4.475	-	-	-
O^{II}	1	4.475	Al^{IV}- O^{II}	-1.729	-0.8095
Si^{IV}	2	0	Si^{IV}-O^{III}, Si^{IV}-O^{II}	1.629, 1.554	0.9858, 1.209
Si^{IV}	4	1.645	-	-	-
Si^{IV}	4	5.293	-	-	-
Si^{IV}	4	3.648	-	-	-
#broken bonds:	12.9/nm^2		APS	11.3/nm^2	
#unsaturated atoms:	11.3/nm^2		ABS	8.1/nm^2	
#atoms within 1.4 Å depth:	11.3/nm^2		TBS	0/nm^2	
#O atoms within 1.4 Å depth:	8.1/nm^2		Area Unit Cell:	0.6185 nm^2	
# sites from partial charges	12.9/nm^2				

Kaolinite (010)

Site	Coordination	Depth (Å)	Broken Bond Type	Length Broken Bond	Brown Strength Broken Bonds
Al^{VI}	2	0	Al^{VI}-OH^{II}, Al^{VI}-OH^{II}, Al^{VI}-O^{III}, Al^{VI}- OH^{II}	1.877, 1.987, 1.909, 1.953	-0.543, -0.403, -0.498, -0.443
O^{II}	1	0.447	Si^{IV}- O^{II}	1.637	0.965
O^{II}	1	1.000	Si^{IV}- O^{II}	1.625	0.997
SI^{IV}	4	8.854	-	-	-
Si^{IV}	4	4.392	-	-	-
Si^{IV}	4	1.518	-	-	-
Si^{IV}	4	5.980	-	-	-
Al^{VI}	6	3.053	-	-	-
Al^{VI}	6	7.515	-	-	-
Al^{VI}	6	4.463	-	-	-
O^{III}	3	8.792	-	-	-

APPENDIX

(continued)

Kaolinite (010)

O^{III}	3	4.329	-	-	-
O^{III}	3	6.016	-	-	-
O^{III}	3	1.553	-	-	-
O^{II}	2	2.990	-	-	-
O^{II}	2	7.453	-	-	-
O^{II}	2	4.909	-	-	-
O^{II}	2	5.463	-	-	-
OH^{II}	2	3.124	-	-	-
OH^{II}	2	7.587	-	-	-
OH^{II}	2	4.374	-	-	-
OH^{II}	2	8.836	-	-	-
OH^{II}	2	5.909	-	-	-
OH^{II}	2	1.446	-	-	-
OH^{II}	2	3.160	-	-	-
OH^{II}	2	7.623	-	-	-
#broken bonds:	$16.4/nm^2$		APS	$10.9/nm^2$	
#unsaturated atoms:	$8.2/nm^2$		ABS	$10.4/nm^2$	
#atoms within 1.4 Å depth:	$8.2/nm^2$		TBS	$-0.2/nm^2$	
#O atoms within 1.4 Å depth:	$5.5/nm^2$		Area Unit Cell:	0.3668 nm^2	
# sites from partial charges	$9.6/nm^2$				

Kaolinite (0-10)

Site	Coordination	Depth (Å)	Broken Bond Type	Length Broken Bond	Brown Strength Broken Bonds
Si^{IV}	2	0	Si^{IV}-O^{II}, Si^{IV}-O^{II}	1.625, 1.637	0.997, 0.965
O^{III}	2	0.063	Al^{VI}-O^{III}	1.909	-0.498
OH^{II}	1	1.268	Al^{VI}- OH^{II}	1.877	-0.543
OH^{II}	1	0.018	Al^{VI}- OH^{II}	1.953	-0.443
OH^{II}	1	1.232	Al^{VI}- OH^{II}	1.987	-0.403
Si^{IV}	4	4.463	-	-	-
Si^{IV}	4	7.337	-	-	-
Si^{IV}	4	2.874	-	-	-
Al^{VI}	6	5.802	-	-	-
Al^{VI}	6	1.339	-	-	-
Al^{VI}	6	8.854	-	-	-
Al^{VI}	6	4.391	-	-	-
O^{III}	3	4.525	-	-	-
O^{III}	3	2.838	-	-	-
O^{III}	3	7.301	-	-	-
O^{II}	2	5.864	-	-	-

APPENDIX

(continued)

Kaolinite (0-10)

O^{II}	2	1.401	-	-	-
O^{II}	2	3.945	-	-	-
O^{II}	2	8.408	-	-	-
O^{II}	2	3.392	-	-	-
O^{II}	2	7.854	-	-	-
OH^{II}	2	5.730	-	-	-
OH^{II}	2	4.481	-	-	-
OH^{II}	2	2.946	-	-	-
OH^{II}	2	7.408	-	-	-
OH^{II}	2	5.694	-	-	-
#broken bonds:	16.4/nm^2		APS	11.4/nm^2	
#unsaturated atoms:	13.6/nm^2		ABS	10.4/nm^2	
#atoms within 1.4 Å depth:	16.4/nm^2		TBS	+0.20/nm^2	
#O atoms within 1.4 Å depth:	10.9/nm^2		Area Unit Cell:	.3668 nm^2	
# sites from partial charges	9.6/nm^2				

Kaolinite (001)

Site	Coordination	Depth (Å)	Broken Bond Type	Length Broken Bond	Brown Strength Broken Bonds
Al^{VI}	6	1.020	-	-	-
Al^{VI}	6	1.020	-	-	-
Al^{VI}	6	1.013	-	-	-
Al^{VI}	6	1.013	-	-	-
Si^{IV}	4	3.744	-	-	-
Si^{IV}	4	3.723	-	-	-
Si^{IV}	4	3.723	-	-	-
Si^{IV}	4	3.744	-	-	-
OH^{II}	2	0.029	-	-	-
OH^{II}	2	0.029	-	-	-
OH^{II}	2	0	-	-	-
OH^{II}	2	0	-	-	-
OH^{II}	2	2.104	-	-	-
OH^{II}	2	2.104	-	-	-
OH^{II}	2	0.014	-	-	-
OH^{II}	2	0.014	-	-	-
O^{III}	3	2.104	-	-	-
O^{III}	3	2.104	-	-	-
O^{III}	3	2.118	-	-	-
O^{III}	3	2.118	-	-	-
O^{II}	2	4.436	-	-	-

APPENDIX

(continued)

Kaolinite (001)

O^{II}	2	4.436	-	-	-
O^{II}	2	4.243	-	-	-
O^{II}	2	4.243	-	-	-
O^{II}	2	4.243	-	-	-
O^{II}	2	4.243	-	-	-
#broken bonds:	$0/nm^2$		APS	$0/nm^2$	
#unsaturated atoms:	$0/nm^2$		ABS	$0/nm^2$	
#atoms within 1.4 Å depth:	$21.8/nm^2$		TBS	$0/nm^2$	
#O atoms within 1.4 Å depth:	$13.1/nm^2$		Area Unit Cell:	$0.4590\ nm^2$	
# sites from partial charges	$0/nm^2$				

Kaolinite (00-1)

Site	Coordination	Depth (Å)	Broken Bond Type	Length Broken Bond	Brown Strength Broken Bonds
Al^{VI}	6	3.223	-	-	-
Al^{VI}	6	3.223	-	-	-
Al^{VI}	6	3.230	-	-	-
Al^{VI}	6	3.230	-	-	-
Si^{IV}	4	0.520	-	-	-
Si^{IV}	4	0.520	-	-	-
Si^{IV}	4	0.499	-	-	-
Si^{IV}	4	0.499	-	-	-
O^{III}	3	2.139	-	-	-
O^{III}	3	2.139	-	-	-
O^{III}	3	2.125	-	-	-
O^{III}	3	2.125	-	-	-
O^{II}	2	0.193	-	-	-
O^{II}	2	0.193	-	-	-
O^{II}	2	0	-	-	-
O^{II}	2	0	-	-	-
OH^{II}	2	0	-	-	-
OH^{II}	2	0	-	-	-
OH^{II}	2	4.243	-	-	-
OH^{II}	2	4.243	-	-	-
OH^{II}	2	4.229	-	-	-
OH^{II}	2	4.229	-	-	-
OH^{II}	2	4.214	-	-	-
OH^{II}	2	4.214	-	-	-
OH^{II}	2	2.139	-	-	-
OH^{II}	2	2.139	-	-	-

APPENDIX

(continued)

Kaolinite (00-1)

#broken bonds:	0/nm^2		APS	0/nm^2	
#unsaturated atoms:	0/nm^2		ABS	0/nm^2	
#atoms within 1.4 Å depth:	21.8/nm^2		TBS	0/nm^2	
#O atoms within 1.4 Å depth:	13.1/nm^2		Area Unit Cell:	0.4590 nm^2	
# sites from partial charges	0/nm^2				

Kaolinite (110)

Site	Coordination	Depth (Å)	Broken Bond Type	Length Broken Bond	Brown Strength Broken Bonds
Al^{VI}	4	0.104	Al^{VI}-OH^{II}, Al^{VI}-O^{III}	1.877, 1.909	0.543, 0.498
O^{II}	1	0.797	Si^{IV}-O^{II}	1.637	-0.965
Si^{IV}	4	3.525	-	-	-
Si^{IV}	4	2.131	-	-	-
Si^{IV}	4	6.462	-	-	-
Si^{IV}	4	7.857	-	-	-
Al^{VI}	6	5.916	-	-	-
Al^{VI}	6	1.585	-	-	-
Al^{VI}	6	4.435	-	-	-
O^{III}	3	3.296	-	-	-
O^{III}	3	1.672	-	-	-
O^{III}	3	6.003	-	-	-
O^{III}	3	2.806	-	-	-
O^{III}	2	7.138	-	-	-
O^{III}	3	7.627	-	-	-
O^{II}	2	7.545	-	-	-
O^{II}	2	5.128	-	-	-
O^{II}	2	3.213	-	-	-
OH^{II}	2	2.815	-	-	-
OH^{II}	2	7.146	-	-	-
OH^{II}	2	1.256	-	-	-
OH^{II}	2	5.587	-	-	-
OH^{II}	2	0	-	-	-
OH^{II}	2	4.331	-	-	-
OH^{II}	2	0.537	-	-	-
OH^{II}	2	4.868	-	-	-
#broken bonds:	7.9/nm^2		APS	5.3/nm^2	
#unsaturated atoms:	5.3/nm^2		ABS	5.3/nm^2	

APPENDIX

(continued)

Kaolinite (110)

#atoms within 1.4 Å depth:	15.9/nm^2		TBS	+0.20/nm^2	
#O atoms within 1.4 Å depth:	13.2/nm^2		Area Unit Cell:	.3779 nm^2	
# sites from partial charges	5.3/nm^2				

Kaolinite (-1-10)

Site	Coordination	Depth (Å)	Broken Bond Type	Length Broken Bond	Brown Strength Broken Bonds
OH^{II}	1	0.710	Al^{VI}-OH^{II}	1.877	-0.543
O^{III}	2	0.230	Al^{VI}-O^{III}	1.909	-0.498
Si^{IV}	3	0	Si^{IV}-O^{II}	1.637	0.965
Si^{IV}	4	4.331	-	-	-
Si^{IV}	4	5.726	-	-	-
Si^{IV}	4	1.395	-	-	-
Al^{VI}	6	1.940	-	-	-
Al^{VI}	6	6.272	-	-	-
Al^{VI}	6	3.422	-	-	-
Al^{VI}	6	7.753	-	-	-
O^{III}	3	4.561	-	-	-
O^{III}	3	1.854	-	-	-
O^{III}	3	6.185	-	-	-
O^{II}	2	0.719	-	-	-
O^{II}	2	5.050	-	-	-
O^{II}	2	2.729	-	-	-
O^{II}	2	7.060	-	-	-
O^{II}	2	0.312	-	-	-
O^{II}	2	4.643	-	-	-
OH^{II}	2	5.042	-	-	-
OH^{II}	2	2.270	-	-	-
OH^{II}	2	6.601	-	-	-
OH^{II}	2	7.857	-	-	-
OH^{II}	2	3.526	-	-	-
OH^{II}	2	2.989	-	-	-
OH^{II}	2	7.320	-	-	-
#broken bonds:	7.9/nm^2		APS	7.1/nm^2	
#unsaturated atoms:	7.9/nm^2		ABS	5.3/nm^2	
#atoms within 1.4 Å depth:	13.3/nm^2		TBS	-0.2/nm^2	
#O atoms within 1.4 Å depth:	10.6/nm^2		Area Unit Cell:	.3779 nm^2	
# sites from partial charges	5.3/nm^2				

APPENDIX

(continued)

Sanidine (010)

Site	Coord	Depth	Broken Bonds	Length Broken Bond	Brown Strength Broken Bonds
K^{X}	10	9.230	-	-	-
K^{X}	10	2.715	-	-	-
K^{X}	10	2.715	-	-	-
K^{X}	10	9.230	-	-	-
O^{IV}	4	0.543	-	-	-
O^{III}	3	11.402	-	-	-
O^{III}	3	0.543	-	-	-
O^{IV}	4	7.058	-	-	-
O^{IV}	4	2.715	-	-	-
O^{III}	2	0.543	Si^{IV}-O^{III}	1.627	
O^{III}	3	7.058	-	-	-
O^{III}	3	7.058	-	-	-
O^{III}	3	0.543	-	-	-
O^{IV}	4	9.230	-	-	-
O^{III}	3	11.402	-	-	-
O^{IV}	4	9.230	-	-	-
O^{III}	3	0.543	-	-	-
O^{III}	3	7.058	-	-	-
O^{III}	3	7.058	-	-	-
O^{III}	2	0.543	Si^{IV}-O^{III}	-1.627	
O^{IV}	4	2.715	-	-	-
O^{III}	3	0.543	-	-	-
Si^{IV}/Al^{IV}	4	1.086	-	-	-
Si^{IV}/Al^{IV}	4	11.945	-	-	-
Si^{IV}/Al^{IV}	4	11.945	-	-	-
Si^{IV}/Al^{IV}	4	1.086	-	-	-
Si^{IV}/Al^{IV}	4	10.859	-	-	-
Si^{IV}/Al^{IV}	4	10.859	-	-	-
Si^{IV}/Al^{IV}	4	7.601	-	-	-
Si^{IV}/Al^{IV}	4	7.601	-	-	-
Si^{IV}/Al^{IV}	3	0	Si^{IV}-O^{III}	1.627	
Si^{IV}/Al^{IV}	3	0	Si^{IV}-O^{III}	1.627	
Si^{IV}/Al^{IV}	4	5.430	-	-	-
Si^{IV}/Al^{IV}	4	5.430	-	-	-
O^{III}	3	4.887	-	-	-
Si^{IV}/Al^{IV}	4	4.344	-	-	-
Si^{IV}/Al^{IV}	4	6.515	-	-	-
Si^{IV}/Al^{IV}	4	6.515	-	-	-
O^{III}	3	4.887	-	-	-
Si^{IV}/Al^{IV}	4	4.344	-	-	-

APPENDIX

(continued)

Sanidine (010)

O^{III}	3	7.058	-	-	-
O^{III}	3	7.058	-	-	-
#broken bonds:	7.3/nm^2		APS		
#unsaturated atoms:	7.3/nm^2		ABS		
#atoms within 1.4 Å depth:	19.9/nm^2		TBS	0/nm^2	
#O atoms within 1.4 Å depth:	12.7/nm^2		Area Unit Cell:	0.5516 nm^2	
# sites from partial charges	7.3/nm^2				

Sanidine (001)

Site	Coordination	Depth (Å)	Broken Bond Type	Length Broken Bond	Brown Strength Broken Bonds
O^{IV}	4	-2.724	-	-	-
O^{IV}	4	-2.724	-	-	-
O^{IV}	4	-2.724	-	-	-
O^{IV}	4	-2.724	-	-	-
O^{IV}	4	-0.567	-	-	-
O^{IV}	4	-0.567	-	-	-
O^{IV}	4	-4.872	-	-	-
O^{IV}	4	-4.872	-	-	-
O^{III}	3	-1.363	-	-	-
O^{III}	3	-1.363	-	-	-
O^{III}	3	-1.363	-	-	-
O^{III}	3	-1.363	-	-	-
O^{III}	3	-4.086	-	-	-
O^{III}	3	-4.086	-	-	-
O^{III}	3	-4.086	-	-	-
O^{III}	3	-4.086	-	-	-
O^{III}	3	-1.363	-	-	-
O^{III}	3	-1.363	-	-	-
O^{III}	3	-1.363	-	-	-
O^{III}	3	-4.086	-	-	-
O^{III}	3	-4.086	-	-	-
O^{III}	3	-4.086	-	-	-
O^{III}	2	0	Si^{IV}-O^{III}	-1.669	
O^{III}	2	0	Si^{IV}-O^{III}	-1.669	
O^{III}	2	0	Si^{IV}-O^{III}	-1.669	
O^{III}	2	0	Si^{IV}-O^{III}	-1.669	
O^{III}	3	-5.448	-	-	-
O^{III}	3	-5.448	-	-	-

APPENDIX

(continued)

Sanidine (001)

O^{III}	3	-5.448	-	-	-
O^{III}	3	-5.448	-	-	-
Si^{IV}/Al^{IV}	3	-0.567	Si^{IV}-O^{III}	1.669	-
Si^{IV}/Al^{IV}	3	-0.567	Si^{IV}-O^{III}	1.669	-
Si^{IV}/Al^{IV}	3	-0.567	Si^{IV}-O^{III}	1.669	-
Si^{IV}/Al^{IV}	3	-0.567	Si^{IV}-O^{III}	1.669	-
Si^{IV}/Al^{IV}	4	-1.363	-	-	-
Si^{IV}/Al^{IV}	4	-1.363	-	-	-
Si^{IV}/Al^{IV}	4	-1.363	-	-	-
Si^{IV}/Al^{IV}	4	-1.363	-	-	-
Si^{IV}/Al^{IV}	4	-4.086			-
Si^{IV}/Al^{IV}	4	-4.086			-
Si^{IV}/Al^{IV}	4	-4.086			-
Si^{IV}/Al^{IV}	4	-4.872			-
Si^{IV}/Al^{IV}	4	-4.872			-
Si^{IV}/Al^{IV}	4	-4.872			-
Si^{IV}/Al^{IV}	4	-4.872	-	-	-
K^{X}	10	-3.613			
K^{X}	10	-3.613			
K^{X}	10	-1.836	-	-	
K^{X}	10	-1.836	-	-	
#broken bonds:	7.1/nm^2		APS	15.2/nm^2	
#unsaturated atoms:	7.1/nm^2		ABS		
#atoms within 1.4 Å depth:	19.6/nm^2		TBS	0/nm^2	
#O atoms within 1.4 Å depth:	12.5/nm^2		Area Unit Cell:	1.120 nm^2	
# sites from partial charges	7.1/nm^2				

Anorthite (010)

Site	Coordination	Depth (Å)	Broken Bond Type	Length Broken Bond	Brown Strength Broken Bonds
O^{III}	2	0	Al^{IV}-O^{III}	1.761	-0.744
Si^{IV}	3	1.215	Si^{IV}-O^{III}	1.634	0.973
O^{III}	2	1.130	Ca^{VI}-O^{III}	2.443	-0.277
Ca^{VI}	4	0.288	Ca^{VI}-O^{III}, Ca^{VI}-O^{III}	2.333, 2.443	0.372, 0.277
O^{III}	1	0.020	Si^{IV}-O^{III}, Ca^{VI}-O^{III}	1.634, 2.333	-0.973, -0.372
O^{III}	2	1.247	Ca^{VI}-O^{III}	2.389	-0.320
Al^{IV}	3	1.338	Al^{IV}-O^{III}	1.761	0.744
O^{IV}	3	1.482	Ca^{VI}-O^{IV}	2.607	-0.177

APPENDIX

(continued)

Anorthite (010)

Ca^{VI}	4	0.063	Ca^{VI}-O^{III}, Ca^{VI}-O^{IV}	2.389, 2.607	0.320, 0.177
Si^{IV}	4	1.391	-	-	-
Al^{IV}	4	1.532	-	-	-
O^{III}	3	1.505	-	-	-
O^{III}	3	1.194	-	-	-
O^{III}	3	1.501	-	-	-
O^{III}	3	1.203	-	-	-
O^{III}	3	2.183	-	-	-
O^{III}	3	1.790	-	-	-
Al^{IV}	4	1.954	-	-	-
O^{II}	2	1.744	-	-	-
O^{II}	2	1.731	-	-	-
O^{II}	2	2.407	-	-	-
Al^{IV}	4	2.260	-	-	-
O^{II}	2	2.500	-	-	-
Si^{IV}	4	1.931	-	-	-
O^{II}	2	2.751	-	-	-
Si^{IV}	4	2.257	-	-	-
O^{II}	2	3.621	-	-	-
O^{III}	3	3.868	-	-	-
O^{II}	2	3.476	-	-	-
Al^{IV}	3	4.177	-	-	-
O^{IV}	3	4.704	-	-	-
Si^{IV}	3	4.000	-	-	-
O^{II}	3	4.632	-	-	-
O^{II}	3	4.491	-	-	-
O^{II}	3	3.987	-	-	-
Al^{IV}	4	4.733	-	-	-
Al^{IV}	4	4.880	-	-	-
Al^{IV}	4	3.924	-	-	-
O^{III}	4	4.455	-	-	-
O^{II}	2	4.544	-	-	-
O^{III}	3	4.712	-	-	-
Si^{IV}	4	4.303	-	-	-
Si^{IV}	4	4.751	-	-	-
O^{III}	3	4.966	-	-	-
Ca^{VI}	6	5.844	-	-	-
O^{III}	3	4.920	-	-	-
O^{III}	3	5.077	-	-	-
O^{III}	3	6.392	-	-	-
O^{III}	3	6.144	-	-	-
O^{III}	3	6.465	-	-	-

APPENDIX

(continued)

Anorthite (010)

Ca^{VI}	6	6.765	-	-	-
O^{III}	3	6.217	-	-	-
Ca^{VI}	6	6.238	-	-	-
Ca^{VI}	6	6.371	-	-	-
O^{III}	3	4.978	-	-	-
Si^{IV}	4	4.935	-	-	-
O^{III}	3	7.632	-	-	-
O^{III}	3	7.643	-	-	-
Si^{IV}	4	7.674	-	-	-
Si^{IV}	4	7.859	-	-	-
O^{III}	3	7.689	-	-	-
O^{III}	3	7.533	-	-	-
Al^{IV}	4	7.729	-	-	-
Al^{IV}	4	7.877	-	-	-
Si^{IV}	4	8.610	-	-	-
O^{II}	2	8.118	-	-	-
O^{IV}	4	7.905	-	-	-
Al^{IV}	4	8.432	-	-	-
O^{III}	3	8.154	-	-	-
O^{II}	2	8.622	-	-	-
O^{II}	2	8.065	-	-	-
Al^{IV}	4	8.685	-	-	-
O^{III}	3	7.897	-	-	-
Si^{IV}	4	8.307	-	-	-
O^{III}	3	8.742	-	-	-
O^{II}	2	7.977	-	-	-
O^{II}	2	9.133	-	-	-
O^{II}	2	9.858	-	-	-
O^{II}	2	8.988	-	-	-
O^{II}	2	10.202	-	-	-
O^{II}	2	10.866	-	-	-
O^{II}	2	10.110	-	-	-
Al^{IV}	4	10.350	-	-	-
Si^{IV}	4	10.678	-	-	-
O^{III}	3	10.427	-	-	-
Al^{IV}	4	10.655	-	-	-
O^{III}	3	10.819	-	-	-
O^{II}	2	10.878	-	-	-
Si^{IV}	4	10.352	-	-	-
Al^{IV}	4	11.271	-	-	-
O^{III}	3	11.362	-	-	-
O^{III}	3	11.108	-	-	-
Al^{IV}	4	11.077	-	-	-

APPENDIX

(continued)

Anorthite (010)

O^{III}	3	11.479	-	-	-
Si^{IV}	4	11.394	-	-	-
O^{III}	3	11.104	-	-	-
O^{III}	3	11.406	-	-	-
O^{IV}	4	11.127	-	-	-
Si^{IV}	4	11.219	–	-	-
O^{III}	3	11.415	-	-	-
O^{III}	3	12.589	-	-	-
Ca^{VI}	6	12.321	-	-	-
Ca^{VI}	6	12.547	-	-	-
O^{III}	3	12.833	-	-	-
#broken bonds:	11.5/nm^2		APS	5.9/nm^2	
#unsaturated atoms:	8.6/nm^2		ABS	5.5/nm^2	
#atoms within 1.4 Å depth:	10.6/nm^2		TBS	0/nm^2	
#O atoms within 1.4 Å depth:	5.8/nm^2		Area Unit Cell:	1.041 nm^2	
# sites from partial charges	4.8/nm^2				

Anorthite (001)

Site	Coordination	Depth (Å)	Broken Bond Type	Length Broken Bond	Brown Strength Broken Bonds
Ca^{VI}	4	1.059	Ca^{VI}-O^{III}, Ca^{VI}-O^{IV}	2.3767, 2.607	0.330, 0.177
O^{III}	2	0.981	Ca^{VI} - O^{III}	2.377	-0.330
Si^{IV}	3	1.284	Si^{IV} - O^{IV}	1.644	0.947
O^{IV}	2	0	Al^{IV} - O^{IV}, Ca^{VI} - O^{IV}	1.772, 2.454	-0.722, -0.268
Ca^{VI}	3	0.906	Ca^{VI} - O^{III}, Ca^{VI} - O^{IV}	2.405, 2.454	0.306, 0.268
O^{III}	2	0.971	Ca^{VI} - O^{III}	2.405	-0.306
Al^{IV}	3	1.391	Al^{IV} - O^{IV}	1.772	0.722
O^{IV}	2	0.008	Si^{IV} - O^{IV}, Ca^{VI} - O^{IV}	1.644, 2.607	-0.947, -0.177
O^{III}	3	1.779	-	-	-
O^{II}	2	1.196	-	-	-
O^{II}	2	1.674	-	-	-
Si^{IV}	4	1.284	-	-	-
Al^{IV}	4	1.887	-	-	-
O^{II}	2	1.651	-	-	-
O^{II}	2	1.876	-	-	-

APPENDIX

(continued)

Anorthite (001)

O^{III}	3	1.718	-	-	-
O^{II}	2	1.284	-	-	-
Si^{IV}	4	1.857	-	-	-
O^{II}	2	1.791	-	-	-
Al^{IV}	4	1.452	-	-	-
Si^{IV}	4	2.341	-	-	-
O^{III}	3	2.635	-	-	-
O^{III}	3	2.523	-	-	-
O^{II}	2	2.461	-	-	-
Al^{IV}	4	2.265	-	-	-
O^{III}	3	2.393	-	-	-
O^{II}	2	3.519	-	-	-
O^{III}	3	3.964	-	-	-
O^{III}	3	4.912	-	-	-
O^{II}	2	4.438	-	-	-
O^{III}	3	4.591	-	-	-
O^{II}	2	3.348	-	-	-
O^{III}	3	4.894	-	-	-
Si^{IV}	4	4.219	-	-	-
Al^{IV}	4	4.898	-	-	-
Al^{IV}	3	4.968	-	-	-
Al^{IV}	4	4.108	-	-	-
Al^{IV}	4	4.184	-	-	-
O^{III}	3	4.981	-	-	-
O^{II}	6	5.788	-	-	-
O^{III}	4	4.869	-	-	-
Si^{IV}	4	4.119	-	-	-
Si^{IV}	3	4.997	-	-	-
O^{III}	6	5.758	-	-	-
Ca^{VI}	3	4.559	-	-	-
O^{III}	2	4.603	-	-	-
O^{III}	3	4.036	-	-	-
Al^{IV}	4	4.771	-	-	-
O^{III}	3	6.521	-	-	-
O^{III}	3	6.144	-	-	-
Ca^{VI}	6	6.835	-	-	-
Si^{IV}	4	4.987	-	-	-
O^{III}	3	6.479	-	-	-
O^{III}	3	5.024	-	-	-
Ca^{VI}	6	6.864	-	-	-
O^{III}	3	6.102	-	-	-
O^{III}	3	7.702	-	-	-
Al^{IV}	4	7.724	-	-	-

APPENDIX

(continued)

Anorthite (001)

O^{III}	3	7.728	-	-	-
O^{III}	3	7.642	-	-	-
Si^{IV}	4	7.726	-	-	-
Al^{IV}	4	7.852	-	-	-
O^{III}	3	8.659	-	-	-
O^{III}	3	8.064	-	-	-
O^{III}	3	7.655	-	-	-
O^{II}	2	8.185	-	-	-
Si^{IV}	4	8.515	-	-	-
Si^{IV}	4	8.403	-	-	-
O^{III}	3	8.032	-	-	-
Al^{IV}	4	8.439	-	-	-
O^{III}	3	8.586	-	-	-
O^{III}	3	7.599	-	-	-
O^{II}	2	8.019	-	-	-
O^{III}	3	7.625	-	-	-
Si^{IV}	4	7.754	-	-	-
Al^{IV}	4	8.504	-	-	-
O^{II}	2	9.103	-	-	-
O^{III}	3	10.229	-	-	-
O^{II}	2	10.949	-	-	-
Al^{IV}	4	10.735	-	-	-
O^{II}	2	9.275	-	-	-
O^{III}	3	10.904	-	-	-
Al^{IV}	4	10.358	-	-	-
Si^{IV}	4	10.766	-	-	-
O^{II}	2	10.162	-	-	-
O^{III}	3	10.843	-	-	-
O^{III}	3	9.988	-	-	-
Si^{IV}	4	10.281	-	-	-
O^{II}	2	10.832	-	-	-
O^{II}	2	11.339	-	-	-
Al^{IV}	4	11.171	-	-	-
O^{II}	2	10.747	-	-	-
O^{III}	3	11.651	-	-	-
Ca^{VI}	6	11.564	-	-	-
Al^{IV}	4	11.232	-	-	-
O^{III}	3	10.100	-	-	-
O^{II}	2	10.972	-	-	-
Si^{IV}	4	11.269	–	-	-
CaV	5	11.716	-	-	-
O^{II}	2	11.427	-	-	-
O^{III}	3	11.641	-	-	-

APPENDIX

(continued)

Anorthite (001)

Si^{IV}	4	11.339	-	-	-
O^{IV}	4	12.622	-	-	-
O^{IV}	4	12.615	-	-	-
#broken bonds:	11.4/nm^2		APS	5.8/nm^2	
#unsaturated atoms:	7.6/nm^2		ABS	5.2/nm^2	
#atoms within 1.4 Å depth:	10.5/nm^2		TBS	0/nm^2	
#O atoms within 1.4 Å depth:	5.7/nm^2		Area Unit Cell:	1.05 nm^2	
# sites from partial charges	5.7/nm^2				

Albite (010)

Site	Coordination	Depth (Å)	Broken Bond Type	Length Broken Bond	Brown Strength Broken Bonds
Na^{V}	3	0.113	Na^{V}-O^{III}, Na^{V}-O^{IV}	2.437, 2.586	0.1801, 0.1206
Na^{V}	5	6.200	-	-	-
Na^{V}	5	6.488	-	-	-
Na^{V}	5	12.575	-	-	-
Al^{IV}	4	2.119	-	-	-
Al^{IV}	4	4.194	-	-	-
Al^{IV}	4	8.494	-	-	-
Al^{IV}	4	10.570	-	-	-
Si^{IV}	4	2.256	-	-	-
Si^{IV}	4	4.057	-	-	-
Si^{IV}	4	8.632	-	-	-
Si^{IV}	4	10.432	-	-	-
Si^{IV}	3	1.377	Si^{IV}-O^{III}	1.632	0.9783
Si^{IV}	4	4.937	-	-	-
Si^{IV}	4	11.312	-	-	-
Si^{IV}	4	1.474	-	-	-
Si^{IV}	4	4.840	-	-	-
Si^{IV}	4	7.849	-	-	-
Si^{IV}	4	7.752	-	-	-
Si^{IV}	4	11.215	-	-	-
O^{IV}	3	1.514	Na^{V}-O^{IV}	2.586	-0.1206
O^{IV}	4	4.799	-	-	-
O^{IV}	4	7.890	-	-	-
O^{IV}	4	11.174	-	-	-
O^{III}	2	0	Si^{IV}-O^{III}	1.632	-0.9783
O^{III}	3	6.375	-	-	-
O^{III}	3	6.314	-	-	-

APPENDIX

(continued)

Albite (010)

O^{III}	3	12.689	-	-	-
O^{III}	3	1.373	-	-	-
O^{III}	3	7.748	-	-	-
O^{III}	3	11.316	-	-	-
O^{III}	3	4.940	-	-	-
O^{II}	2	1.868	-	-	-
O^{II}	2	4.446	-	-	-
O^{II}	2	8.243	-	-	-
O^{II}	2	10.821	-	-	-
O^{II}	2	2.487	-	-	-
O^{II}	2	3.826	-	-	-
O^{II}	2	8.862	-	-	-
O^{II}	2	10.201	-	-	-
O^{II}	2	2.441	-	-	-
O^{II}	2	3.872	-	-	-
O^{II}	2	8.816	-	-	-
O^{II}	2	10.247	-	-	-
O^{III}	2	1.359	Na^{V}-O^{III}	2.437	-0.1801
O^{III}	3	4.954	-	-	-
O^{III}	3	7.734	-	-	-
O^{III}	3	11.330	-	-	-
O^{II}	2	1.649	-	-	-
O^{II}	2	4.664	-	-	-
O^{II}	2	8.025	-	-	-
O^{II}	2	11.039	-	-	-
#broken bonds:	11.5/nm^2		APS	6.2/nm^2	
#unsaturated atoms:	9.6/nm^2		ABS	4.97/nm^2	
#atoms within 1.4 Å depth:	9.6/nm^2		TBS	0/nm^2	
#O atoms within 1.4 Å depth:	5.8/nm^2		Area Unit Cell:	0.5211 nm^2	
# sites from partial charges	3.8/nm^2				

Albite (001)

Site	Coordination	Depth (Å)	Broken Bond Type	Length Broken Bond	Brown Strength Broken Bonds
Na^{V}	3	0.722	Na^{V}-O^{IV}, Na^{V}-O^{IV}	2.461, 2.586	0.1688, 0.1206
Na^{V}	3	0.722	Na^{V}-O^{IV}, Na^{V}-O^{IV}	2.461, 2.586	0.1688, 0.1206
Na^{V}	5	5.236	-	-	-
Na^{V}	5	5.236	-	-	-

APPENDIX

(continued)

Albite (001)

Al^{IV}	3	1.114	Al^{IV}-O^{IV}	1.777	0.7106
Al^{IV}	3	1.114	Al^{IV}-O^{IV}	1.777	0.7106
Al^{IV}	4	4.844	-	-	-
Al^{IV}	4	4.844	-	-	-
Si^{IV}	4	1.301	-	-	-
Si^{IV}	4	1.301	-	-	-
Si^{IV}	4	4.658	-	-	-
Si^{IV}	4	4.658	-	-	-
Si^{IV}	4	1.798	-	-	-
Si^{IV}	4	1.798	-	-	-
Si^{IV}	4	4.160	-	-	-
Si^{IV}	4	4.160	-	-	-
Si^{IV}	4	2.090	-	-	-
Si^{IV}	4	2.090	-	-	-
Si^{IV}	4	3.869	-	-	-
Si^{IV}	4	3.869	-	-	-
O^{IV}	2	0	Na^{V}-O^{IV}, Na^{V}-O^{IV}	1.777, 2.586	-0.7106, -0.1206
O^{IV}	2	0	Na^{V}-O^{IV}, Na^{V}-O^{IV}	1.777, 2.586	-0.7106, -0.1206
O^{IV}	4	5.959	-	-	-
O^{IV}	4	5.959	-	-	-
O^{III}	2	1.003	Na^{V}-O^{III}	2.461	-0.1688
O^{III}	2	1.003	Na^{V}-O^{III}	2.461	-0.1688
O^{III}	3	1.577	-	-	-
O^{III}	3	1.577	-	-	-
O^{III}	3	4.382	-	-	-
O^{III}	3	4.382	-	-	-
O^{III}	3	4.956	-	-	-
O^{III}	2	4.956	-	-	-
O^{II}	2	4.520	-	-	-
O^{II}	2	4.520	-	-	-
O^{II}	2	1.438	-	-	-
O^{II}	2	1.438	-	-	-
O^{II}	2	4.447	-	-	-
O^{II}	2	4.447	-	-	-
O^{II}	2	1.512	-	-	-
O^{II}	2	1.512	-	-	-
O^{II}	2	4.705	-	-	-
O^{II}	2	4.705	-	-	-
O^{II}	2	1.254	-	-	-
O^{II}	2	1.254	-	-	-
O^{III}	3	2.271	-	-	-

APPENDIX

(continued)

Albite (001)

O^{III}	3	2.271	-	-	-
O^{III}	3	3.688	-	-	-
O^{III}	3	3.688	-	-	-
O^{II}	2	2.571	-	-	-
O^{II}	2	2.571	-	-	-
O^{II}	2	3.388	-	-	-
O^{II}	2	3.388	-	-	-
#broken bonds:	11.5/nm^2		APS	5.4/nm^2	
#unsaturated atoms:	7.7/nm^2		ABS	3.85/nm^2	
#atoms within 1.4 Å depth:	11.5/nm^2		TBS	0/nm^2	
#O atoms within 1.4 Å depth:	5.8/nm^2		Area Unit Cell:	1.04 nm^2	
# sites from partial charges	3.8/nm^2				

References

Aines, R. D., and Rossman, G. R., 1984, Water in minerals? A peak in the infrared: Journal of Geophysical Research, v. 89(B6), p. 4059–4071.

Altermatt, D., and Brown, I. D., 1985, Bond-valence parameters obtained from a systematic analysis of the inorganic crystal structure database: Acta Crystallographica, v. B41, p. 244–247.

Altmann, R. S., ms, 1985, Copper binding in heterogeneous, multicomponent aqueous systems: mathematical and experimental modeling: Ph.D. thesis, Stanford University.

Amrhein, C., and Suarez, D. L., 1988, The use of a surface complexation model to describe the kinetics of ligand-promoted dissolution of anorthite: Geochimica et Cosmochimica Acta, v. 52, p. 2785–2793.

Anderson, P. J., Horlock, R. F., and Oliver, J. F., 1965, Interaction of water with the magnesium oxide surface: Transactions of the Faraday Society, v. 61, p. 2754–2762.

Barron, V., and Torrent, J., 1996, Surface hydroxyl configuration of various crystal faces of hematite and goethite: Journal of Colloid and Interface Science, v. 177, p. 407–410.

Becker, U., Hochella, M. F., Jr., and Apra, E., 1996, The electronic structure of hematite {001} surfaces: applications to the interpretation of STM images and heterogeneous surface reactions: American Mineralogist, v. 81, p. 1301–1314.

Bergna, H. E., 1994, Colloid chemistry of silica: an overview, *in* Bergna, H. E., editor, The Colloid Chemistry of Silica: Washington, D.C., American Chemical Society, p. 1–47.

Berner, R. A., 1994, Chemical weathering and its effect on atmospheric CO_2 and climate, *in* White, A. F., and Brantley, S. L., editor, Chemical Weathering Rates of Silicate Minerals: Mineralogical Society of America, Reviews in Mineralogy, v. 31, p. 565–583.

Bloss, F. D., and Gibbs, G. V., 1963, Cleavage in quartz: American Mineralogist, v. 48, p. 821–838.

Blum, A. E., and Lasaga, A. C., 1991, The role of surface speciation in the dissolution of albite: Geochimica et Cosmochimica Acta, v. 55, p. 2193–2201.

Boehm, H. P., 1966, Chemical identification of surface groups: Advances in Catalysis, v. 12, p. 179–274.

Boehm, H. P., 1971, Acidic and basic properties of hydroxylated metal oxide surfaces: Discussions of the Faraday Society, v. 52, p. 264–275.

Boehm, H. P., and Knozinger, H., 1983, Nature and estimation of functional groups on solid surfaces, *in* Anderson, J. R., and Boudart, M., editors, Catalysis Science and Technology, v. 4: New York, Springer, p. 39–207.

Boily, J.-F., and Fein, J. B., 1996, Experimental study of cadmium-citrate co-adsorption onto α-Al_2O_3: Geochimica et Cosmochimica Acta, v. 60, p. 2929–2938.

Brady, P. V., and Walther, J. V., 1990, Kinetics of quartz dissolution at low temperatures: Chemical Geology, v. 82, p. 253–264.

Brown, I. D., and Shannon, R. D., 1973, Empirical bond-strength-bond-length curves for oxides: Acta Crystallographica, v. A29, p. 266–282.

Casey, W. H., Hochella, M. F., and Westrich, H. R., 1993, The surface chemistry of manganiferous silicate minerals as inferred from experiments on tephroite (Mn_2SiO_4): Geochimica et Cosmochimica Acta. v. 57, p. 785–793.

Davis, J. A., and Kent, D. B., 1990, Surface complexation modeling in aqueous geochemistry, *in* Hochella, M. F., Jr., and White, A. F., editors, Mineral-Water Interface Geochemistry: Mineralogical Society of America, Reviews in Mineralogy, v. 23, p. 177–260.

Davis, J. A., James, R. O., and Leckie, J. O., 1978, Surface ionization and complexation at the oxide/water interface. I. Computation of electrical double layer properties in simple electrolytes: Journal of Colloid and Interface Science, v. 63, p. 480–499.

Davis, J. A., and Kent, D. B., 1990, Surface complexation modeling in aqueous geochemistry, *in* Hochella, M. F., Jr., and White, A. F., editors, Mineral-Water Interface Geochemistry: Mineralogical Society of America Reviews in Mineralogy, v. 23, p. 177–307.

Deer, W. A., Howie, R. A., and Zussman, J., 1993, An Introduction to the Rock-Forming Minerals, 2nd edition: Essex, England, Longman Scientific and Technical, 696 p.

Derouane, E. G., Fraissard, J., Fripiat, J. J., and Stone, W. E. E., 1972, NMR studies in adsorption and heterogeneous catalysis: Catalysis Reviews, v. 7, p. 121–212.

Dove, P. M., 1994, Kinetic and thermodynamic controls on silica reactivity in weathering environments, in White, A. F. and Brantley, S. L., editors, Chemical Weathering Rates of Silicate Minerals: Mineralogical Society of America, Reviews in Mineralogy, v. 31 p. 235–290.

Dove, P. M., and Elston, S. F., 1992, Dissolution kinetics of quartz in sodium chloride solutions: analysis of existing data and a rate model for 25°C: Geochimica et Cosmochimica Acta, v. 56, p. 4147–4156.

Dzombak, D. A., and Morel, F. M. M., 1990, Surface Complexation Modeling: Hydrous Ferric Oxide: New York, John Wiley and Sons, Inc., 393 p.

Finger, L. W., and Hazen, R. M., 1978, Crystal structure and compression of ruby to 46 kbar: Journal of Applied Physics, v. 49, p. 5823–5826.

Furrer, G., and Stumm, W., 1986, The coordination chemistry of weathering: I. Dissolution kinetics of δ-Al_2O_3 and BeO: Geochimica et Cosmochimica Acta, v. 51, p. 1847–1860.

Gallei, E., and Parks, G. A., 1972, Evidence for surface hydroxyl groups in attenuated total reflectance spectra of crystalline quartz: Journal of Colloid and Interface Science, v. 38, p. 650–651.

Hair, M. L., 1967, Infrared Spectroscopy in Surface Chemistry: New York, Marcel Dekker, Inc., 315 p.

Harlow, G. E., and Brown, G. E., 1980, Low albite: an X-ray and neutron diffraction study: American Mineralogist, v. 65, p. 986–995.

Hayes, K. F., Redden, G., Ela, W., and Leckie, J. O., 1991, Surface complexation models: an evaluation of model parameter estimation using FITEQL and oxide mineral titration data: Journal of Colloid and Interface Science, v. 142, p. 448–469.

Heinrich, V. E., 1983, The nature of transition-metal-oxide surfaces: Progress in Surface Science, v. 14, p. 175–200.

Hiemstra, T., Riemsdijk, W. H. V., and Bolt, G. H., 1989, Multisite proton adsorption modeling at the solid/solution interface of (hydr)oxides: A new approach I. Model description and evaluation of reaction constants: Journal of Colloid and Interface Science, v. 133, p. 91–104.

Hiemstra, T., Wit, J. C. M. D., and Riemsdijk, W. H. V., 1989, Multisite proton adsorption modeling at the solid/solution interface of (hydr)oxides: A new approach II. Applications to various important (hydr)oxides: Journal of Colloid and Interface Science, v. 133, p. 105–117.

Hochella, M. F., Jr., 1990, Atomic structure, microtopography, composition, and reactivity of mineral surfaces, *in* Hochella, M. F., Jr., and White, A., editors, Mineral-Water Interface Geochemistry: Mineralogical Society of America, Reviews in Mineralogy, v. 23, p. 87–132.

Hochella, M. F., Jr., 1995, Mineral surfaces: their characterization and their chemical, physical and reactive nature, *in* Vaughan, D. J., and Pattrick, R. A. D., editors, Mineral Surfaces Mineralogical Society Series, v. 5: New York, Chapman and Hall, p. 17–60.

Hohl, H., and Stumm, W., 1976, Interaction of Pb^{2+} with hydrous α-Al_2O_3. Journal of Colloid and Interface Science, v. 55, p. 281–288.

Hollabaugh, C. M., and Chessick, J. J., 1961, Adsorption of water and polar paraffinic compounds onto rutile: Journal of Physical Chemistry, v. 65, p. 109–114.

Hsi, C.-K. D., and Langmuir, D., 1985, Adsorption of uranyl onto ferric oxyhydroxides: Application of the surface complexation site-binding model: Geochimica et Cosmochimica Acta, v. 49, p. 1931–1941.

Huang, C. P., ms, 1971, Ph.D. thesis, Harvard University, Cambridge, Massachusetts.

Huang, C. P., and Stumm, W., 1973, Specific adsorption of cations on hydrous α-Al_2O_3: Journal of Colloid and Interface Science, v. 22, p. 231–259.

Iler, R., 1979, The Chemistry of Silica: New York, John Wiley and Sons.

James, R. O., and Parks, G. A., 1982, Characterization of aqueous colloids by their electrical double-layer and intrinsic surface chemical properties, *in* Matijevic, E., editor, Surface and Colloid Science, v. 12: New York, Plenum Press, p. 119–216.

Jones, P., and Hockey, J. A., 1971a, Infra-red Studies of Rutile Surfaces: Part 1. Transactions of the Faraday Society, v. 67, p. 2669–2678.

—— 1971b, Infra-red Studies of Rutile Surfaces. Part 2.–Hydroxylation, hydration and structure of rutile surfaces: Transactions of the Faraday Society, v. 67, p. 2679–2685.

Jones, P., and Hockey, J. A., 1972, Infra-red studies of rutile surfaces. Part 3. Adsorption of water and dehydroxylation of rutile: Journal of the Chemical Society, Faraday Transactions I, v. 68, p. 907–913.

Kihara, K., 1990, An X-ray study of the temperature dependence of the quartz structure. European Journal of Mineralogy, v. 2, p. 63–77.

Klein, C., and Hurlbut, C. S., Jr., 1993, Manual of Mineralogy, 21st edition.: New York, John Wiley and Sons, 681 p.

Koretsky, C. M., Sverjensky, D. A., Salisbury, J. W., and D'Aria, D. M., 1997, Detection of surface hydroxyl species on quartz and feldspars using reflectance infrared spectroscopy: Geochimica et Cosmochimica Acta, v. 61, p. 2193–2210.

Kubicki, J. D., Blake, G. A., and Apitz, S. E., 1996, Ab initio calculations on aluminosilicate Q3 species: implications for atomic structures of mineral surfaces and dissolution mechanisms of feldspars: American Mineralogist, v. 81, p. 789–799.
Little, L. H., 1966, Infrared spectra of adsorbed species: London, Academic Press., 428 p.
Lövgren, L., Sjöberg, S., and Schindler, P. W., 1990, Acid/base reactions and Al(III) complexation at the surface of goethite: Geochimica et Cosmochimica Acta, v. 54, p. 1301–1306.
McCafferty, E., and Zettlemoyer, A. C., 1971, Adsorption of water vapour on α-Fe_2O_3: Discussions of the Faraday Society, v. 52, p. 239–263.
Morterra, C., Ghiotti, G., Garrone, E., and Boccuzzi, F., 1976, Infrared spectroscopic characterization of the α-alumina surface: Journal of the Chemical Society, Faraday Transactions I, v. 72, p. 2722–2734.
Morterra, C., Magnacca, G., and Del Favero, N., 1993, IR study of CO adsorption at ~77K on α-Al_2O_3: Langmuir, v. 9, p. 642–645.
Morimoto, T., Nagao, M., and Tokuda, F., 1969, The relation between the amounts of chemisorbed and physisorbed water on metal oxides: Journal of Physical Chemistry, v. 73, p. 243–248.
Palmer, D., 1996, CrystalMaker©: Cambridge, United Kingdom, Cambridge University Technical Services Ltd.
Parfitt, R. L., Russell, J. D., and Farmer, V. C., 1976, Confirmation of the surface structures of goethite (α-FeOOH) and phosphated goethite by infrared spectroscopy. Journal of the Chemical Society, Faraday I, v. 72, p. 1082–1087.
Peri, J. B., 1965, A model for the surface of γ-alumina: Journal of Physical Chemistry, v. 69, p. 220–230.
Rochester, C. H., and Topham, S. A., 1979, Infrared study of surface hydroxyl groups on hematite. Journal of the Chemical Society, Faraday Transactions, v. 75, p. 1073–1088.
Russell, J. D., Parfitt, R. L., Fraser, A. R., and Farmer, V. C., 1974, Surface structures of gibbsite, goethite and phosphated goethite: Nature, v. 248, p. 220–221.
Rustad, J. R., Felmy, A. R., and Hay, B. P., 1996a, Molecular statics calculations for iron oxide and oxyhydroxide minerals: toward a flexible model of the reaction mineral-water interface: Geochimica et Cosmochimica Acta, v. 60(9), p. 1553–1562.
——— 1996b. Molecular statics calculations of proton binding to goethite surfaces: a new approach to estimation of stability constants for multisite surface complexation models: Geochimica et Cosmochimica Acta, v. 60(9), p. 1563–1576.
Sahai, N., and Svjerjensky, D. A., 1997, Evaluation of internally consistent parameters for the triple-layer model by the systematic analysis of oxide surface titration data: Geochimica et Cosmochimica Acta, v. 61, p. 2801–2826.
Schindler, P. W., and Kamber, H. R., 1968, Die aciditat von silanolgruppen: Helvetica Chimica Acta, v. 51, p. 1781–1786.
Schindler, P. W., and Stumm, W., 1987, The surface chemistry of oxides, hydroxides and oxide minerals, *in* Stumm, W., editors, Aquatic Surface Chemistry: New York, John Wiley, p. 83–110.
Schneider, M., ms, 1962: Ph.D. thesis, University of Heidelberg, Germany.
Sposito, G., 1984, The Surface Chemistry of Soils: New York, Oxford University Press., 234 p.
Stillings, L. L., Brantley, S. L., and Machesky, M. L., 1995, Proton adsorption at an adularia feldspar surface: Geochimica et Cosmochimica Acta, v. 59, p. 1473–1482.
Stumm, W., Huang, C. P., and Jenkins, S. R., 1970, Specific chemical interactions affecting the stability of dispersed systems: Croatica Chemica Acta, v. 42, p. 223–244.
Sverjensky, D. A., 1993, Physical surface-complexation models for sorption at the mineral-water interface: Nature, v. 364, p. 776–780.
Sverjensky, D. A., Criscenti, L. J., Koretsky, C. M., and Sahai, N., 1995, A constant capacitance model for dissolution rates for oxides and silicates at 25°C and 1 bar: EOS, American Geophysical Union Spring Meeting, S101.
Sverjensky, D. A., and Sahai, N., 1996, Theoretical prediction of single-site surface-protonation equilibrium constants for oxides and silicates in water: Geochimica et Cosmochimica Acta, v. 60(20), p. 3773–3797.
Szytula, A., Burewicz, A., Dimitrijevic, Z., Krasnicki, S., Rzany, H., Todorovic, J., Warvic, A., and Wolski, W., 1968, Neutron diffreaction studies of a-FeOOH: Physica Status Solidi, v. 26, p. 429–434.
Tsukada, M., Adachi, H., and Satoko, C., 1983, Theory of electronic structure of oxide surfaces: Progress in Surface Science, v. 14, p. 113–174.
Tsyganenko, A. A., and Filimonov, V. N., 1973, Infrared spectra of surface hydroxyl groups and crystalline structure of oxides: Journal of Molecular Structure, v. 19, p. 579–589.
Wainwright, J. E., and Starkey, J., 1971, A refinement of the structure of anorthite: Zeitschrift fur Kristallographie, v. 133, p. 75–84.
Wieland, E., and Stumm, W., 1992, Dissolution kinetics of kaolinite in acidic aqueous solutions at 25°C: Geochimica et Cosmochimica Acta, v. 56, p. 3339–3355.
Wyckoff, R. W. G., 1960, Crystal Structures, v. III: New York, Interscience Publishers, Inc.
Yates, D. E., ms, 1975, The structure of the oxide/aqueous electrolyte interface: Ph.D. thesis, University of Melbourne.
Yates, D. E., Grieser, F., Cooper, R., and Healy, T. W., 1977, Tritium exchange studies on metal oxide colloidal dispersions: Australian Journal of Chemistry, v. 30, p. 1655–1660.
Yates, D. J. C., 1961, Infrared studies of the surface hydroxyl groups on titanium dioxide, and of the chemisorption of carbon monoxide and carbon dioxide: Journal of Physical Chemistry, v. 65, p. 746–753.
Zoltai, T., and Stout, J. H., 1984, Mineralogy: Concepts and Principles: Minneapolis, Minnesota, Burgess Publishing Co, 505 p.